TEMPERATURE AND SCALING STUDIES FROM PROJECTILE

FRAGMENTATION OF ^{86,78}KR+^{64,58}NI AT 35 MEV/A

A Dissertation

by

SARA KATHERINE WUENSCHEL

Submitted to the Office of Graduate Studies of
Texas A&M University
in partial fulfillment of the requirements for the degree of

DOCTOR OF PHILOSOPHY

August 2009

Major Subject: Chemistry

TEMPERATURE AND SCALING STUDIES FROM PROJECTILE

FRAGMENTATION OF ^{86,78}KR+^{64,58}NI AT 35 MEV/A

A Dissertation

by

SARA KATHERINE WUENSCHEL

Submitted to the Office of Graduate Studies of
Texas A&M University
in partial fulfillment of the requirements for the degree of

DOCTOR OF PHILOSOPHY

Approved by:

Chair of Committee,	Sherry J. Yennello
Committee Members,	Che-Ming Ko
	Rand L. Watson
	Joseph B. Natowitz
Head of Department,	David H. Russell

August 2009

Major Subject: Chemistry

ABSTRACT

Temperature and Scaling Studies from Projectile Fragmentation of ^{86,78}Kr+^{64,58}Ni

at 35 MeV/A. (August 2009)

Sara Katherine Wuenschel, B.S., LeTourneau University

Chair of Advisory Committee: Dr. Sherry J. Yennello

Many observables have been developed to study the effects of the two component nature of nuclei. This dissertation has experimentally probed caloric curves as well as scaling observables for their dependence on the asymmetric portion of the nuclear equation of state. Projectile fragmentation sources were identified from the reactions of ^{86,78}Kr+^{64,58}Ni at 35 MeV/A taken on the NIMROD-ISiS array. The angular coverage, excellent isotopic resolution, and Neutron Ball allow for quasi-complete event reconstruction in both charge and mass.

A new thermometer for nuclear fragmentation studies has been derived and is presented here. In this thermometer, the temperature is obtained from fluctuations of the transverse momentum. The proton transverse momentum fluctuations are used in this thesis to study the N/Z dependence of the nuclear caloric curve. The caloric curve constructed from proton momentum fluctuations does not show a significant dependence on the source N/Z ratio. Two other thermometers have also been studied in this thesis: the double isotope ratio, and moving source slope thermometers. These thermometers show no statistically significant dependence on the source N/Z.

The source density has been derived from the evolution of fragment Coulomb barriers with increasing E*/A. This density showed no source N/Z dependence. However, a strong evolution in source density over the E*/A=1.5–7.5 MeV region was observed.

Fragment scaling was investigated through isoscaling and power law scaling. The

power law scaling showed a strong dependence on the source N/Z. This source N/Z dependence was further investigated through isoscaling. The fragment yields of this data have been shown to exhibit consistent isoscaling for Z=1–17. In addition, isoscaling was observed in data cut on the E^*/A of the source yielding decreasing slopes (α) as a function of E^*/A. This decrease, normalized to the asymmetries of the sources (α/Δ), has been linked to a decrease in the asymmetry coefficient C_{sym}.

This dissertation has shown that the experimentally observed decrease in C_{sym} with E^*/A is well correlated to the temperature and density changes experimentally observed in this data.

To my husband Josiah

ACKNOWLEDGMENTS

It has been a privilege to conduct my graduate studies at the Texas A&M University Cyclotron Institute. I would like to thank the staff of the Institute first for their great help during the upgrade of NIMROD to NIMROD-ISiS as well as for their support during this dissertation experiment. Thanks are also due Kris Hagel and Roy Wada for their extensive help and input through out the experimental upgrade, experiment, and data analysis. I would next like to thank my committee Drs. Che-Ming Ko, Joseph Natowitz, and Rand Watson. I would like to thank Aldo Bonasera for his never ceasing stream of ideas and many useful and enlightening conversations. Thanks are also due to my family and particularly to my husband for their support, love, and encouragement. Finally, and perhaps most importantly, are the thanks due to my advisor Sherry Yennello. Words do not seem enough to properly thank her for her guidance, support, and general awesomeness. I entered graduate school looking for an advisor and I have found not only that, but also a friend.

TABLE OF CONTENTS

LIST OF TABLES

LIST OF FIGURES

FIGURE   Page

FIGURE   Page

FIGURE   Page

CHAPTER I

INTRODUCTION

For many years, the onset of multi-fragmentation in excited nuclei has been associated with a liquid-to-gas type phase transition [1, 2]. Phase transition studies have been conducted using yields from discrete telescopes [1, 3, 4] and quasi-complete event detectors [5, 6, 7, 8, 9]. These efforts have yielded general information about nuclear phase transitions [10, 11, 12, 13]. However, significant questions about the effect of the two-component nature of the nucleus on experimental observables remain [9, 14, 15, 16, 17].

A.   Equation of State

Nuclear binding energy as a function of pressure, temperature, composition, etc. may be described by means of an equation of state (EOS). These EOS's vary from the schematic phenomenological models [18, 19] to very complex quantum descriptions [20, 21]. The nuclear binding energy is well understood for ground state nuclei with T=0, ρ/ρ_0=1. In the ground state, the nuclear binding energy of a finite nucleus can be described through a liquid drop model. The basis of nuclear phase transition studies can be easily understood in the framework of this simple model.

The Weisacker model is based on a liquid drop description of the nucleus [22, 23]. The energy holding a liquid-like drop together is referred to as the binding energy (BE). The leading terms of this formalism describe the volume (a_vA) and surface ($a_s A^{2/3}$) effects. The Weisaker model (Eq. 1.1) incorporates additional terms to accommodate the charged, two-component, and structured nature of nuclei. In

---

The journal model is Physical Review C.

this model, the nuclear binding energy is parameterized as

$$BE = a_v A - a_s A^{2/3} - a_c Z(Z-1)A^{-1/3} - a_{sym}(A-2Z)^2 A^{-1} + \delta \qquad (1.1)$$

where Z is the proton number, A is the mass number, and coefficients of each term (a_v, a_s, a_c, and a_{sym}) have been obtained from fitting to known nuclear binding energies obtained from experimentally measured nuclear masses [22, 23]. Because the nucleon-nucleon interaction is short range, only the nearest neighbor nucleons contribute to the volume term. This interaction is proportional to A, the total number of neutrons (N) and protons (Z). The decrease in binding energy due to the surface must be considered to accurately describe a finite liquid drop. This decrease in total binding energy is the result of the surface nucleons (neutrons or protons) having fewer neighboring nucleons to interact with. From geometry, the decrease in binding energy due to the surface is proportional to $A^{2/3}$.

In nuclei, we must differentiate between the number of neutrons and the number of protons. The Coulomb repulsion between the protons in the nucleus decreases the total binding energy. The Coulomb force is a relatively long range force, thus the repulsion between the protons must be taken as Z(Z-1). Assuming a spherical nucleus, the Coulomb term of the nuclear binding energy becomes $Z(Z-1)A^{-1/3}$.

The symmetry term reflects the loss in the binding energy from an inequality in the total number of neutrons and protons. The loss of binding energy arises from the interaction potential difference between like and unlike nucleons [24]. In small nuclei with low Coulomb repulsion, there is a strong tendency for the number of neutrons and protons to be equal. As the size of the nucleus increases, an increasing number of neutrons are required to moderate the drop in binding energy due to increased Coulomb repulsion. Thus, for larger Z nuclei there are more N$\neq$Z isotopes energetically available. The generally accepted form of this term is $(A-2Z)^2/A$. The

final term (δ) is the pairing factor accounting for the odd-even structure in nuclei.

The coefficients used in this binding energy parameterization have been well established for ground state nuclei. It should be noted, however, that the symmetry energy coefficient is not constant in the nuclear equation of state. Rather, it is a function of the temperature and density of the nuclear material. The density and temperature dependence of this symmetry coefficient, which is often referred to in the literature as C_{sym}, is of particular interest to current nuclear physics research.

As a nucleus is heated, the largest effects result from the energy cost of increasing the nuclear surface through deformation or fragmentation. These effects have long been studied through Fisher's droplet model [1, 25, 26] by means of power law scaling. In the Fisher Droplet Model (FDM), the probability of a fragment being produced can be written as

$$Yield \propto l^{-\tau} exp \left[- \left(f_l - \mu l \right) \beta \right] \tag{1.2}$$

where l is the fragment size, f_l is the fragment free energy, μ is the chemical potential per particle, and β is $1/T$ [27]. The term incorporating τ results mathematically from accounting for variations in the fragment surface geometry. In the phase transition region the free energy and chemical potential terms cancel and the nucleus breaks up as a result of the Coulomb potential [27]. The formula then becomes

$$Yield \propto l^{-\tau} \tag{1.3}$$

where the probability of a particle of size l being produced has a negative power law behavior. Experimentally, l is defined as the A or Z of the fragment and τ is a fitting parameter describing the slope of a charge or mass distribution.

The schematic drawings in the left panels of Fig. 1 depict a nucleus at three possible stages of heating: evaporation (top), multi-fragmentation (middle), and va-

porization(bottom). At low energy, (top, left panel of Fig. 1) the excited nuclear system disposes of excess energy by evaporating one or more small particles thereby creating more surface. The corresponding charge distribution is shown in the right panel with peaks corresponding to the small evaporated fragments and the residue. In this low energy regime, the evaporation of light particles produces a very steep slope in the charge (or mass) distribution if the residue is excluded.

At higher energies, the nucleus will break into several similarly sized fragments as is shown in the middle, left panel of Fig. 1. This phenomena is referred to as multi-fragmentation and is the result of more decay channels becoming energetically accessible. The slope of the charge (or mass) distribution is much more shallow in this energy regime as depicted in the middle, right panel of Fig. 1.

At relatively high energy, the system undergoes quasi-complete vaporization into light charged particles and free neutrons (Fig. 1 bottom, left panel). This again creates a very steep particle distribution. Though the system shown in the bottom, right panel is clearly not vaporized, the increase in slope of the distribution can be seen between the middle and bottom panels of this figure.

Theoretically and experimentally, the minimum in the slope parameter (τ) should correspond to multi-fragmentation behavior in nuclei. Theory also dictates that the value of τ should be between 2 and 3 in the phase transition region [25].

Smaller effects, resulting from the Coulomb and symmetry contributions to nuclear binding energy, can be seen in phase transition observables. These effects have been investigated through caloric curve studies. The caloric curve represents the relationship between temperature and excitation energy. Thermodynamically, the temperature should pass through a plateau or singularity as the result of a phase transition. In nuclei this temperature is referred to as the limiting temperature which is the maximum temperature a finite nucleus can obtain. This is related to, though
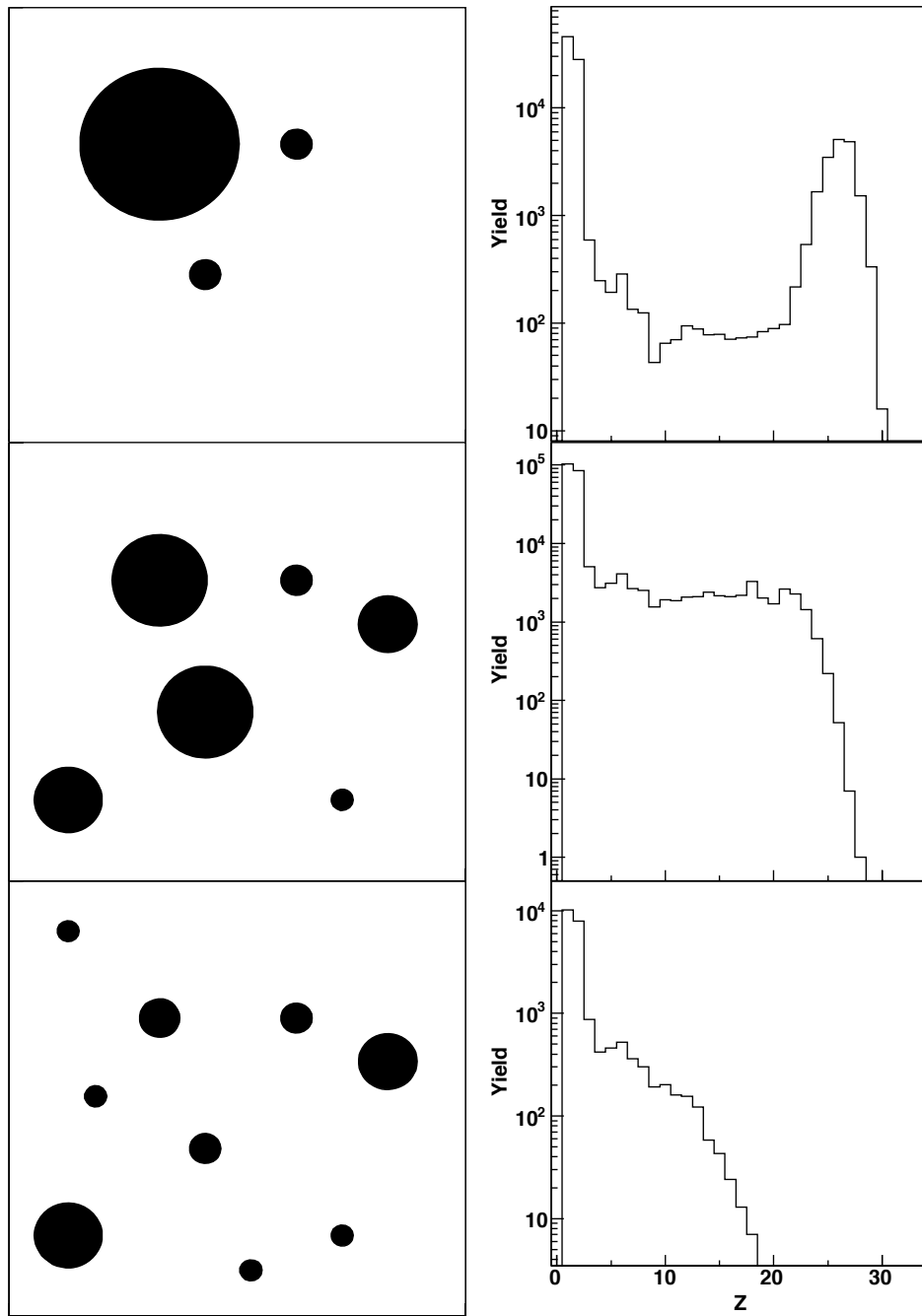
FIG. 1. Left: The figure depicts evaporation (top), multi-fragmentation (middle), va-
porization (bottom) for a large nucleus. The radius corresponds to the size of
the nuclear fragment produced. Right: This figure presents the corresponding
fragment charge distributions for a nucleus at low (top), medium (middle),
and high (bottom) excitation energies.

not the same as, the critical temperature that is achievable only in theory and infinite nuclear matter [14, 28, 29]. Limiting temperatures have been experimentally measured to be ∼6–9 MeV while the critical temperature is calculated to be ∼14–16 MeV [28]. Through comparison of caloric curves constructed from a wide range of system sizes, the decrease in binding energy due to Coulomb repulsion has been shown to lower the limiting temperature with increasing system size [28].

The effect of the two-component nature of nuclei on phase change behavior has yet to be experimentally determined. A key challenge in these studies is to accurately determine the neutron-to-proton ratio of the fragmenting source [30]. Traditionally, the source composition has been most often derived from the reacting system [13, 17]. This assumption neglects the neutron and proton exchange occurring during the interaction between projectile and target nuclei. Recently, quasi-projectile reconstruction studies have sought to improve the knowledge of the neutron and proton composition of the source [30, 31].

B.   Experimental Signatures of Phase Transitions in Nuclei

Studies of phase transition signatures can be categorized in two broad groups: discrete telescopes and 4π experiments. The discrete telescopes have generally contributed isotopically resolved particle yields with little global event characterization. On the opposite end of the spectrum, the 4π experiments have provided global event characterization with limited isotopic information. These experiments have yielded productive phase transition research in which many signatures of a nuclear phase transition have been proposed and tested [32]. Here we will focus on the power law scaling and caloric curve observables.

The first experimental study to show signatures consistent with a nuclear liquid-

gas phase transition was conducted using discrete telescope fragment yields from the reaction of 80-350 GeV Protons on Xe and Kr [1]. The isobaric fragment yield distribution exhibited power law scaling as predicted by Fisher [25]. This study also yielded a value of τ ($\sim$ 2.6) consistent with the theoretically predicted range of 2–3. After further analysis of this data set [26, 27], the authors expanded the one-component Fisher scaling formalism to account for the two component nature of nuclei in the chemical potential term.

Scaling studies have also been conducted on source-selected data taken on multi-detector arrays. It was shown by Mastinu *et al.* [6] that multiple regions of the nuclear phase diagram could be investigated in a single reaction at a single beam energy by selecting on impact parameter observables or event excitation energy. Subsequently, source selected nuclear systems have been studied extensively by the ISiS, INDRA, MINIBALL, CHIMERA, NIMROD, etc. [5, 6, 7, 8, 33] collaborations.

Through comparing the large body of nuclear scaling data some consensus has been achieved [10, 11, 12]. The slope parameter, τ, clearly changes with E*/A and a minimum should be achieved in the multi-fragmentation region [6, 8, 27]. Additionally, while some experimental and theoretical works question the implication of criticality from Fisher scaling, scaling studies retain theoretical impact through correlation with other observables more directly indicative of phase change such as caloric curves [7, 34, 35].

Throughout the literature, caloric curves are most often constructed using one of three methods for calculating nuclear temperature: Maxwellian fits to kinetic energy distributions, excited state populations, and yield ratios of isotopes [36, 37, 38].

The first thermometer follows from the Maxwell-Boltzmann relation

$$Yield \propto \exp^{-E/kT} \tag{1.4}$$

between energy state occupation probability and system temperature. The temperature is obtained experimentally by fitting the particle kinetic energy distribution where the slope of the distribution is related to the temperature of the system.

In a notable study by Wada *et al.* [39], the slope thermometer was implemented to construct one of the first nuclear caloric curves. This data exhibited a plateau for excitation energies above 3 MeV/A. The slope thermometer has since been used in a wide variety of experiments [27, 39, 40, 41]. However, as reaction mechanisms become increasingly violent the values obtained with this thermometer become higher relative to other thermometers. Additionally, the values obtained are significantly larger than the ~5–8 MeV commonly used in statistical multifragmentation models to reproduce fragment yields [42]. Theoretical analysis with the single particle model has explained the measured temperature as 50% thermal with the remainder resulting from particle Fermi momenta [27, 40, 42] and/or collective radial flow resulting from compression during projectile-target interaction [43, 44].

The second thermometer examines the relative probability of two excited states being produced in a system. The probabilities are linked to temperature through

$$\frac{P_1}{P_2} = \frac{2s_1 + 1}{2s_2 + 1} exp\left[\frac{-(E_1 - E_2)}{T}\right] \tag{1.5}$$

where $P_{1,2}$ are the probabilities of state 1 and 2, $s_{1,2}$ is the spin of state 1 and 2, and $E_{1,2}$ is the excitation energy of the states 1 and 2. When using particle unbound states to observe high temperatures, this thermometer has an advantage over other thermometers due to the relatively weak influence of secondary decays [13]. However, this thermometer has been shown to saturate in sources with E^*/A above the excitation energy of the excited states being studied [10, 13].

Excited state temperatures were directly compared to double isotope temperatures by Imme *et al.* [45]. This study showed a strong saturation at high reaction

energy in the excited state temperature while the double isotope temperatures continued to rise.

The double isotope ratio thermometer was proposed by Albergo [36] and has been widely used for 4π type experiments [5, 8, 46]. This thermometer operates on the assumption that the source is thermally and chemically equilibrated. A temperature is then obtained via the relation

$$T_{app} \quad = \quad B/ln(aR_{app}) \tag{1.6}$$

$$where$$

$$B \quad = \quad BE(A_i, Z_i) - BE(A_i + 1, Z_i) + BE(A_j, Z_j) - BE(A_j + 1, Z_j),$$

$$a \quad = \quad \frac{[2S(A_j, Z_j) + 1] / [2S(A_j + \Delta A_j, Z_j + \Delta Z_j) + 1]}{[2S(A_i, Z_i) + 1] / [2S(A_i + \Delta A_i, Z_i + \Delta Z_i) + 1]} \left[\frac{A_j/(A_j + \Delta A_j)}{A_i/(A_i + \Delta A_i)} \right]^{\eta},$$

$$R_{app} \quad = \quad Y(A_i, Z_i)/Y(A_i + 1, Z_i) \; / \; Y(A_j, Z_j)/Y(A_j + 1, Z_j).$$

B is a function of the ground state binding energies, R_{app} is the observed apparent yield ratio, and a is a function of the ground state particle spins of the chosen isotopes. The factor η in a varies depending on whether volume or surface emission is assumed. For $\Delta A=1$, $\eta \sim 1$ in either case [37]. The elements chosen for R_{app} generally differ by only one proton, and the isotopes of each element by only one neutron. The binding energy term is required to be large relative to the temperatures derived [36]. For this reason, double isotope thermometers generally incorporate the ^{3,4}He, ^{11,12}C, or ^{15,16}O isotopes.

Using the isotopic ratios obtained via peripheral heavy-ion reactions, a landmark study by Pochadzilla *et al.* [46] produced a caloric curve spanning a wide range of excitation energies. This data showed a rise in the region of surface evaporation, a strong plateau through multifragmentation, and at high excitation energy exhibited another rise that was interpreted as vaporization of the system. Subsequent studies
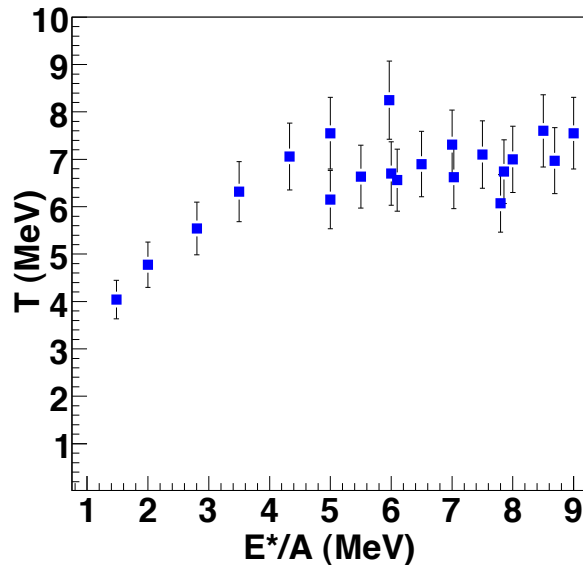
FIG. 2. Compilation of experimental caloric curves from sources with A=60–100 [28].

have investigated a wide range of reaction mechanisms and isotope ratios [5, 37, 41, 44, 47].

In response to caloric curve studies, an important question arose as to whether the strong plateau seen in caloric curves obtained from heavy ion reactions is truly a signature of a nuclear phase transition or rather the result of collective radial flow. This concern is particularly important for very central heavy ion reactions. However, a benchmark for nearly pure thermal expansion was provided by the ISiS light–ion induced reactions [5, 41]. This reaction mechanism has been shown to produce very little collective radial expansion when compared to theoretical multifragmentation codes [48]. In addition, the data from these studies exhibit a plateau similar to those observed in heavy ion reactions.

Temperatures derived using the double isotope method must be corrected for secondary decay effects on the observed isotopic fragment yields. Various models have

been used to estimate the magnitude of this correction [37, 47]. T_{app} is generally some-what lower than the model corrected value. The magnitude of this correction varies with the isotopes chosen for the thermometer. It has been proposed by Trautman *et al.* that the inconsistency between double isotope ratio pairs may indicate a disconnection between chemical and thermal equilibrium in the fragmenting source [47].

Published experimental caloric curves have been compiled by Natowitz *et al.* [28]. The various experimental caloric curves were found to agree within errors of each other when compiled by the size of the fragmenting source nucleus. A representative curve from this compilation is plotted in Fig. 2. This figure corresponds to systems in the A=60-100 region and exhibits a limiting temperature of approximately 7 MeV.

C.   This Dissertation

The effect of the ratio of neutrons-to-protons (N/Z) is a challenging experimental problem remaining for nuclear phase transition studies. To investigate this effect, 35 MeV/A ^{86,78}Kr + ^{64,58}Ni reaction systems were studied with the 4π NIMROD-ISiS detector. The projectiles, targets, and detection system were selected to provide projectile fragmentation sources with a wide range of N/Z [30]. The intermediate system size was chosen to minimize both the Coulomb instability present in large nuclear systems and the structure effects present in small nuclei [28]. Projectile fragmentation sources are believed to have only small collective radial flow [43] and thus provide minimal collective radial contamination to the thermal expansion. In addition, this size of system should be optimal for observing a change in limiting temperature with respect to N/Z [14].

CHAPTER II

EXPERIMENTAL

Quasi-projectiles were identified from the projectile fragmentation reactions of ^{86,78}Kr + ^{64,58}Ni (Table I) at 35 MeV/nucleon. The reactions were conducted at the Texas A&M University Cyclotron Institute and the results collected using the NIMROD-ISiS 4π array [49]. The detector thresholds, inverse kinematics reaction mechanism, and electronic triggers were chosen to maximize the desired projectile fragmentation events. The fragment particle identification method was chosen to retain the highest quality of elemental and isotopic fragment designation for the events.

The experimental reactions are summarized in Table I. Each beam was accelerated to 35 MeV/nucleon and impinged upon a self supporting Ni target. The charge state of each beam as well as the target thicknesses are provided in Table I. In addition, the beam intensity is provided in electrical units of pA or nA. The two key systems are the most neutron-rich ^{86}Kr+^{64}Ni and least neutron-rich ^{78}Kr+^{58}Ni as is reflected in the number of hours of data acquired for each beam–target combination.

A. Detector Configuration

The NIMROD-ISiS detector array is a 4π charged particle array within a neutron calorimeter. The 14 concentric rings of the charged particle array cover the lab angles between 3.6 and 167 degrees. Table II shows the angular range of each ring and the $\Delta\phi'$s associated with them. Each ring is composed of 12, 18, or 24 detector modules generally referred to as telescopes. The telescopes are composed of one or two thin energy loss detectors and a final thick stopping detector. The comparison of energy loss and remaining energy capitalizes on the charge and mass dependence of fragment energy loss in matter [22]. In NIMROD-ISiS the energy loss detectors are

TABLE I. Beams and target reaction systems taken for this thesis.

Beam	^{86}Kr	^{86}Kr	^{78}Kr	^{78}Kr
Target	^{64}Ni	^{58}Ni	^{58}Ni	^{64}Ni
Target Thickness	1.05mg/cm^2	1.7mg/cm^2	1.7mg/cm^2	1.05mg/cm^2
Target Purity	97.9%	99%	99%	97.9%
Beam Charge State	27+	27+	25+	25+
Avg. Beam Intensity	300pA	300pA	10nA	10nA
Hours	82.96	40.31	52.95	32.83

150, 300, or 500μm Si wafers. The stopping detectors are either 500μm Si wafers or CsI crystals.

NIMROD-ISiS is the result of combining the NIMROD (Neutron Ion Multidetector for Reaction Oriented Dynamics) and the ISiS (Indiana Silicon Sphere) [50] arrays. The forward most eight rings of the array are based on the design for the INDRA [51] 4π array. The intermediate rings (10-11) provide detection in the 45-90 degree region and were designed based on the ISiS geometry. These two rings also serve to mate the forward rings with the rear hemisphere that is composed of one half of the original ISiS array.

As shown in Fig. 3, the charged particle array is housed inside the TAMU Neutron Ball [49, 52]. The Neutron Ball provides signal and background neutron multiplicities for each event. The neutrons are detected using a scintillator made of $\sim$0.3 wt% Gd doped pseudocumene. Each segment of the Neutron Ball is read out with either 3 or 4 (quadrant and hemisphere respectively) photomultiplier tubes mounted on viewing ports equipped with fish eye lenses to maximize the detection efficiency. The upper and side quadrants of the neutron ball are radially displaced outward,

TABLE II. Angular layout of the NIMROD-ISiS array. The telescope and super telescope Si configurations at each angle are given with the CsI crystal lengths.

Ring	Θ Range degrees	ϕ Range degrees	Telescopes Silicon number (thickness)	Super Telescopes	CsI Length cm
2	3.6-5.0	30	10 (300μm)	2	10.0
3	5.0-7.6	30	10 (300μm)	2	10.0
4	8.0-10.8	30	10 (300μm)	2	10.0
5	10.8-14.7	30	10 (300μm)	2	10.0
6	15.3-20.9	30	5 (300μm) 5 (150μm)	2	6.5
7	20.9-27.6	15	5 (300μm) 5 (150μm)	2	6.5
8	28.6-35.8	30	6 (300μm) 4 (150μm)	2	6.0
9	35.8-45.0	15	6 (300μm) 4 (150μm)	2	6.0
10	52.7-69.2	-	-	140+100μm	4.0
11	70.1-86.3	20	1 (300μm) 1(500μm)	-	3.0
12	93.5-110.8	20	18 (500μm)	-	2.8
13	110.8-128.4	20	18 (500μm)	-	2.8
14	128.4-147.4	20	18 (500μm)	-	2.8
15	147.4-167.0	20	18 (500μm)	-	2.8
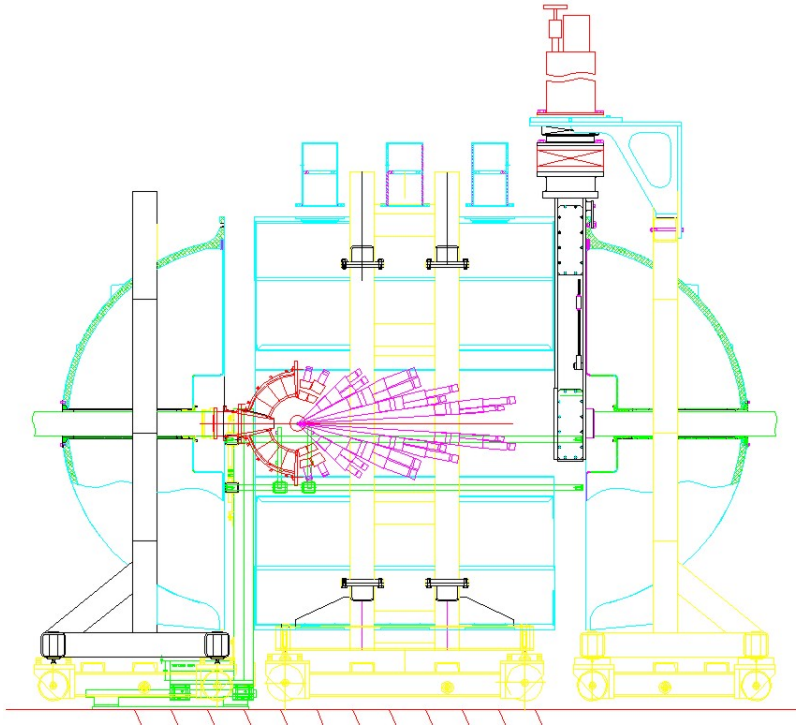
FIG. 3. Charged particle array inside Neutron Ball. Beam enters from the left of this figure. (color online)

providing 4 in and 2 in gaps respectively. The upper opening provides a clearer path for neutron time of flight measurements in experiments using supplementary discrete neutron detectors. However, there is no change in the charged particle array detector configuration or the chamber thickness in these regions. Each of the three major portions of the Neutron Ball is mounted on a track. This allows them to be moved independently and provides access to the inner charged particle detector chamber. The beam enters the array from the left in Fig. 3.

The GEANT-3 [54] simulation code was used in conjunction with the GCALOR [55] package to evaluate the Neutron Ball efficiency [49, 53]. Fig. 4 shows the calculated results for the Neutron Ball efficiencies. DENIS code [56] predictions are depicted
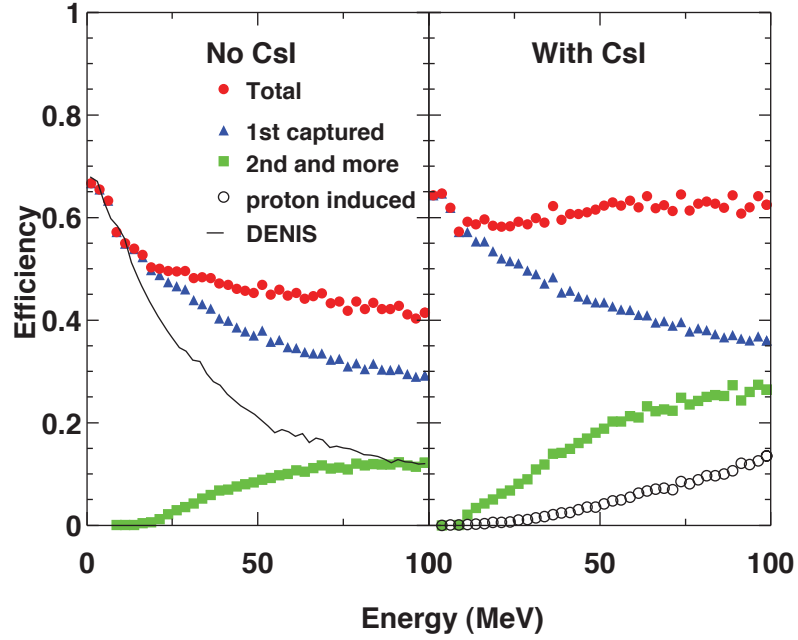
FIG. 4. Calculated neutron ball efficiency without the charged particle array (a) and with the charged particle array (b). Intrinsic neutron efficiency at a given energy is shown by dots. The contribution of the first detected neutrons is shown by triangles and that of the second and higher order detected neutrons is shown by squares. The solid line in the left figure shows results from the DENIS code. The open circles in the right figure display the detection efficiency of generated neutrons when a proton of an initial energy, given on x-axis, is emitted at the target [49, 53]. (color online)

by a solid line for the case without the charged particle array [52]. Below 10 MeV both calculations agree reasonably well. However, for the higher energy neutrons, the efficiency calculated by DENIS is lower than the results for the first detected neutrons in the GEANT-3 simulation (triangles). This results from the lack of neutron generation in DENIS and indicates that a significant number of secondary neutrons are generated by high energy neutrons.

A large number of energetic electrons are produced during the interaction phase of a nuclear reaction. These electrons can interact with the detectors creating background. The target ladder of NIMROD-ISiS is designed to hold up to 40 kV for suppression of these electrons. The voltage was set to 25 kV for this experiment.

Angular coverage, detection thresholds, and granularity are important when selecting or configuring a detector for an experiment. This experiment was carried out with inverse kinematics (heavy projectile on lighter target) and focused on projectile-like events. Thus the forward most angles are the most important for particle detection and the particles of interest are carrying some remnant of the beam momentum. The addition of beam momentum to the event break-up energy effectively lowers the center of mass energy required for particles to overcome detector thresholds. The detection thresholds important for this configuration of NIMROD-ISiS are shown in Table III.

Table II lists the number of telescopes and super telescopes for each ring as the detector was configured for this experiment. Each of the rings 2–9 contained two super telescopes. The super telescopes consist of a 150 and 500 μm Si and a CsI crystal and were placed at the 1 and 2 o'clock positions as viewed from the target. The remainder of these rings were composed of regular telescopes with a 150 or 300 μm Si and a CsI crystal. At these angles the Si detectors (3.6–45 degrees) are segmented on the p+ side (front) and have a single n+ backplane. Rings 10 and 11 did not include Si

TABLE III. Detector energy thresholds relevant to the configuration of NIMROD-ISiS for this thesis. Thresholds were calculated using the energy loss code SRIM [57].

Si Thickness	α Threshold	^{12}C Threshold
140μm	15MeV	85MeV
150μm	16MeV	89MeV
300μm	24MeV	134MeV
500μm	32MeV	182MeV
650μm	38MeV	212MeV
1000μm	49MeV	274MeV

detectors during this experiment. The remaining angles (rings 12–15) are composed of 500μm Si and CsI. For these Si the backplane is n+. A graphical layout of each ring, with detector numbers, can be see in Appendix A. This appendix also provides details about non-functioning detectors.

Raw experimental spectra are shown in Fig. 5 for the three possible sources of particle identification in the telescopes and super telescopes. Pulse shape discrimination based on the fast and slow components of the CsI light output can provide isotopic identification of Z=1,2 particles. This is shown in the top panel of the figure. Energy loss versus remaining energy, such as Si-CsI (middle panel) and Si-Si (bottom panel), provide charge and mass identification for heavier particles.

The experimental data was taken with downscaled minimum bias, high multiplicity, and pulser triggers. The minimum bias triggered on any event, regardless of the number of particles detected, and was downscaled by a factor of 10. The high multiplicity trigger was set with a threshold of 3–5 CsI detectors providing signals. The
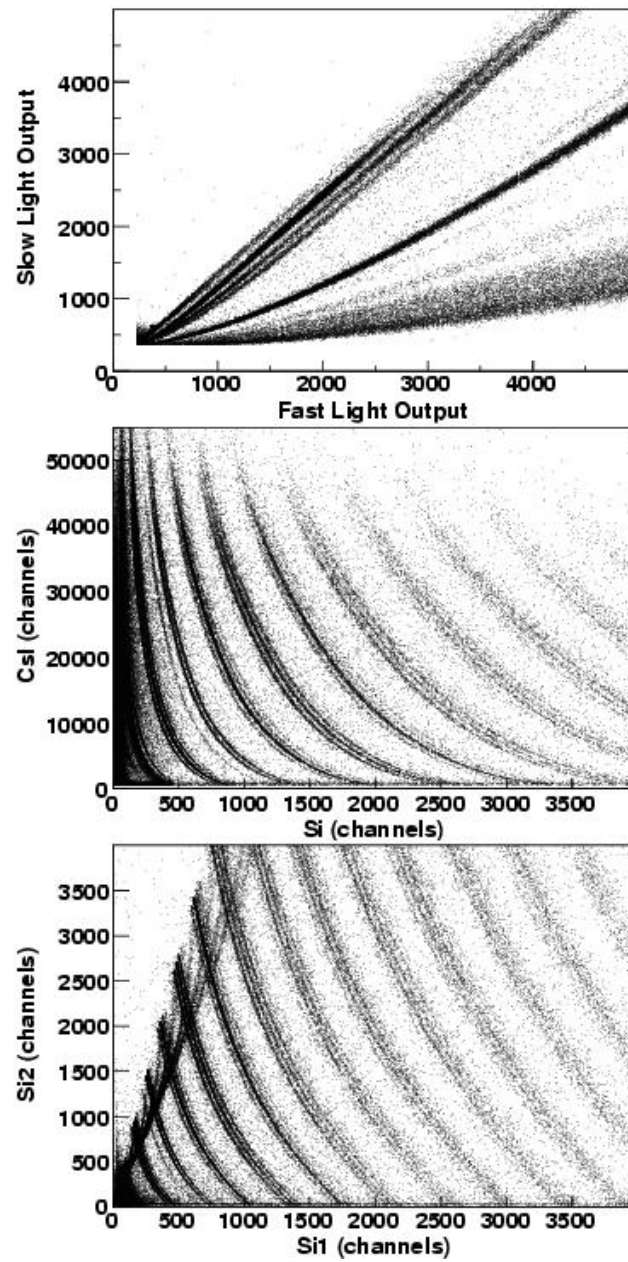
FIG. 5. Sources of particle identification in a detector module. Top) CsI pulse shape discrimination of the light output of the CsI crystal. Middle) Energy deposited in Si vs the energy deposited in the CsI. Bottom) Energy deposited in the 150μm Si vs 500μm Si. (color online)

pulser trigger provided background events for the Neutron Ball. During the experiment, data was acquired with proprietary software based on the ROOT [58] package and was written to disk in packets that were then converted to event-by-event files. The acquisition software also provided real time monitoring of the detectors.

B. Electronic Set Up

A significant effort was made during set up, to modularize the detector outputs for signal correlation. Motherboards house preamplifiers [59] on the outside surface of the vacuum chamber and collect the telescope signals to be passed modularly to the electronics. Two designs of motherboards are used. The first eight rings employ custom boards. However, the ISiS region functions with boards supplied by Zepto Systems [59]. The modular signals are passed through coaxial ribbon cables to a splitting panel where the signals are then sent to the next stage of electronics.

The electronic signal analysis will be addressed in six logical segments: the forward angle (3.6–45 degrees) Si, the ISiS (90–167 degrees) Si, the forward angle (3.6–90 degrees) CsI, the ISiS (90–167 degrees) CsI, the Neutron Ball, and the triggering logic. The Si signals are divided based on the detector design, and the CsI are divided based on the light read out mechanism. A schematic representation of the electronic and triggering logic can be found in Figs. 6-9 and a description of the modules used is given in Table IV.

In rings 2-9, the energy deposited in the Si is read from both the front and back of the detector. Signals taken from the front quadrants are amplified by CAMAC Pico System [60] shaping amplifiers. Signals from the back plane are processed by CAMAC Pico System Shaper Discriminators that provide both amplified and trigger logic timing outputs. The amplified signals from both the front and back of the detectors

Si signals
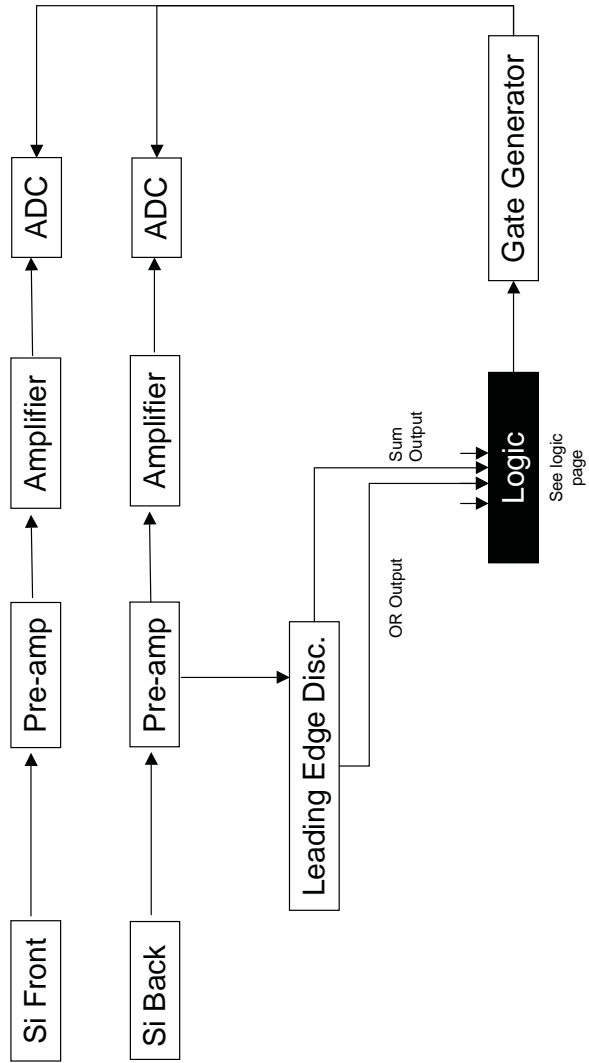
FIG. 6. Si electronics diagram
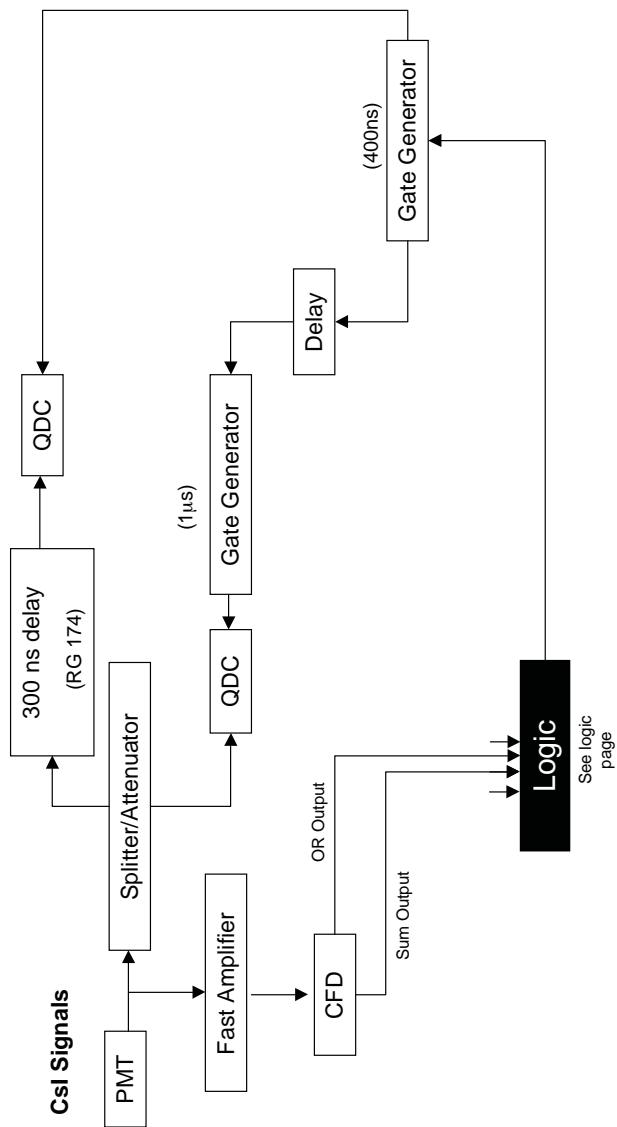
FIG. 7. CsI electronics diagram
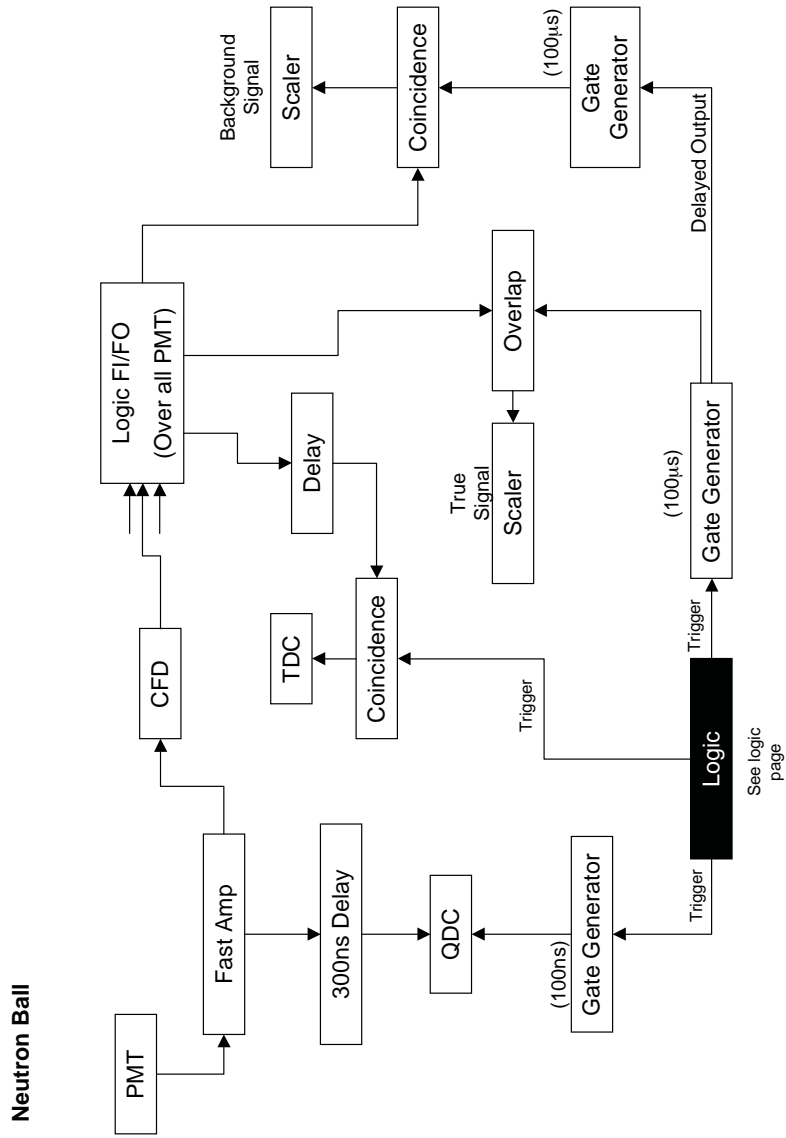
FIG. 8. Neutron Ball electronics diagram
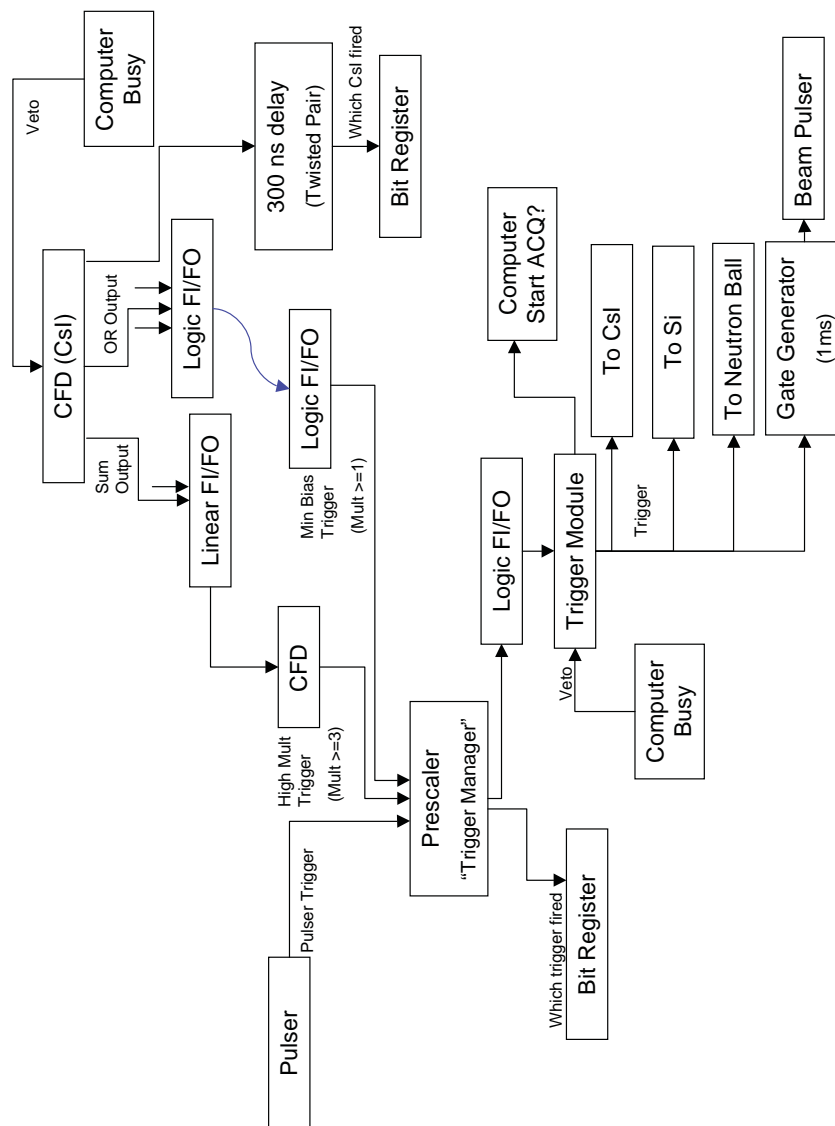
FIG. 9. Trigger logic electronics diagram

TABLE IV. Electronic modules used in the analysis of raw signals and triggering logic for this thesis.

Module Name	Abv.	Function	Modules Used
Constant Fraction Discriminator	CFD	Determines if the signal is above threshold with minimal walk in the timing signal produced	LeCroy 3420, Tennelec 454
Leading Edge Discriminator	LED	Determines if a signal is above a threshold	LeCroy 623B, Pico Sys. Shaper Disc.
Peak Sensing Analog to Digital Converter	ADC	Converts analog peak height to digital signal	Phillips 7164
Peak Integrating Analog to Digital Converter	QDC	Converts peak integral to digital signal	LeCroy 1885F, Phillips 7166
Fast Amplifier	FA	Amplifies the signal without changing its shape	LeCroy 612A
Shaping Amplifier	-	Amplifies, integrates, and differentiates the signal producing a uni- or bipolar signal	Pico Sys. Shaper,Pico Sys. Shaper Disc., Orange Quad

TABLE IV, Continued

Module Name	Abv.	Function	Modules Used
Linear Fan in Fan out	AND	Creates a linear sum of the input signals, multiple copies of this signal are available	LeCroy 428F
Logic Fan in Fan out	FI/FO, OR	Creates a single logic signal if any input fired, multiple copies of this signal are available	LeCroy 429A, PS 757,756
Coincidence	-	Produces a logic signal when the selected coincidence level is achieved among the inputs	LeCroy 356AL
Time to Digital Converter	TDC	Digitizes the time difference between two input signals	LeCroy 1875A
Bit Register	-	Marks a bit assigned to each fired input when triggered by the DAQ	LeCroy 4448, 2341A
Gate Generator	-	Creates an adjustable width logic signal when triggered	LeCroy 222, PS 794, GG 8000,8010
Scaler	-	Counts signals received in coincidence with a gate	LeCroy 4434

are then digitized by CAMAC Phillips peak sensing ADCs. The ISiS Si signals are amplified by shaping amplifiers inherited from the original ISiS electronics [50] and use VME peak sensing ADCs. The silicon signals were not used in the triggering logic for this experiment.

In the forward hemisphere (3.6–90 degrees), the CsI are read by photomultiplier tubes (PMT). These signals are passed through a proprietary splitter-attenuator and three copies of the signal sent out. One copy is attenuated and passed through 300 ns of delay cables before entering a charge to digital converter (QDC). Another copy is attenuated and sent directly to a QDC to digitize the slow portion of the light. A third copy of the signal is passed to a fast amplifier. The amplified signal enters a constant fraction discriminator (CFD) that provides a logic output for the triggering system. During a good event, the logic returns a gate for the QDCs. This gate is 400 ns long and slightly delayed for the fast signal. The delay time was chosen such that the gate opened at the peak of the PMT signal. The gate for the slow signal is delayed to open 1 μs after the PMT signal began and is 1 μs long. These gates are not traditional in their placement on the signal. However, these delay settings were experimentally determined to provide the best isotopic resolution in these detectors.

The photomultiplier signals from the Neutron Ball are passed to fast amplifiers and the amplified outputs are split. One copy is sent through 300 ns of delay to a QDC. A copy of the DAQ trigger generates a 100 μs gate that joins the data at the QDC. The second copy of the amplified signal is passed to a CFD and from there to a logic fan-in-fan-out (FI/FO) that performs a logical OR over all of the PMT signals. The CFD thresholds are set to reproduce the modeled efficiency of the Neutron Ball for ^{252}Cf neutrons. The trigger also passes to a coincidence module where it is overlapped with the logical OR of the PMTs. The overlap is output to a TDC. A third copy of the DAQ trigger generates a 100 μs gate that is passed

through a coincidence overlap with the logic OR of the PMTs. The signals collected within this gate are counted as the true event signals. The delayed output logic signal from this gate is sent to a second gate generator to create a second 100 μs gate for background counting.

The triggering logic was based entirely off of the CsI signals for this experiment. Three logical triggers were constructed: minimum bias, high multiplicity, and pulser. A minimum of one PMT was required for the minimum bias trigger. The high multiplicity trigger required 3 or more PMTs to have signals. A beam pulser deflected the beam for 1 ms while an event was collected. This minimized the probability of two events being counted as one. It was also intended to minimize background in the Neutron Ball signal gate. The pulser trigger was included to provide a more accurate Neutron Ball background accounting for the time before the beam pulser activates. The triggers were run simultaneously and scaled using a prescaler (trigger module).

The minimum bias trigger is constructed from the CsI PMT CFD logic OR signals. This OR output is present if any PMT in the CFD produced a signal. The OR CsI CFD signal is passed to a logic FI/FO over all CsI PMTs to create a combined OR. This combined OR signal provides the minimum bias event trigger to the prescaler. The high multiplicity trigger is constructed from the CsI PMT CFD SUM logic signals. The SUM signal indicates the number of PMTs in the CFD that produced a signal. This SUM from each CFD is passed through a decoupler to ensure that the baseline is zero before being passed to a FI/FO over all of the PMT CFDs to create a combined SUM. A threshold is set on the combined SUM signal to provide a high multiplicity trigger. The pulser trigger for Neutron Ball background is also passed to the prescaler.

A divide factor is placed on each trigger in the prescaler to adjust the relative acquisition rates. A signal related to which trigger fired is output by the prescaler to

a bit register. This signal also passes to a coincidence module that provides a logical OR over the triggers. The OR signal passes to the trigger module (logic FI/FO) where it joins with the computer busy veto. If the computer is not busy, this final trigger is fanned out to provide a start for the computer DAQ and gate generators for the CsI, Si, Neutron Ball, and beam pulser.

C. Particle Identification

Particle identification can be done on either calibrated or uncalibrated data. If calibrated spectra are used, changes to the calibrations necessitate alterations in the particle identification. In light of this, uncalibrated spectra were used for particle identification in this data set. The particle identification was carried out using a linearization method.

The data plots provide separation between the elements and in most cases the isotopes, however these bands have a curvature that follows a complex function. The goal of linearization is to straighten these lines and then project the straightened lines onto an axis resulting in a plot such as Fig. 10. The top, left panel is Z=1,2 isotopic yield distributions obtained from pulse shape discrimination of CsI light output. The top, right (Z=3-6) and bottom, left (Z=7-10) panels are from energy lost in Si versus the remaining energy collected in the CsI. The final panel (bottom, right) shows isotopic resolution for Z=11-14 from energy lost in the 150 μm si versus the remaining energy collected in the 500 μm Si.

To linearize the data, lines were first chosen to follow along each elemental band. Fig. 11 shows these lines overlaid on raw data from a Si-CsI telescope. The lines were chosen to follow either the most prominent isotope or the left-most strong isotope. Two lines were generally chosen for Z=1 to optimize the isotopic resolution of this
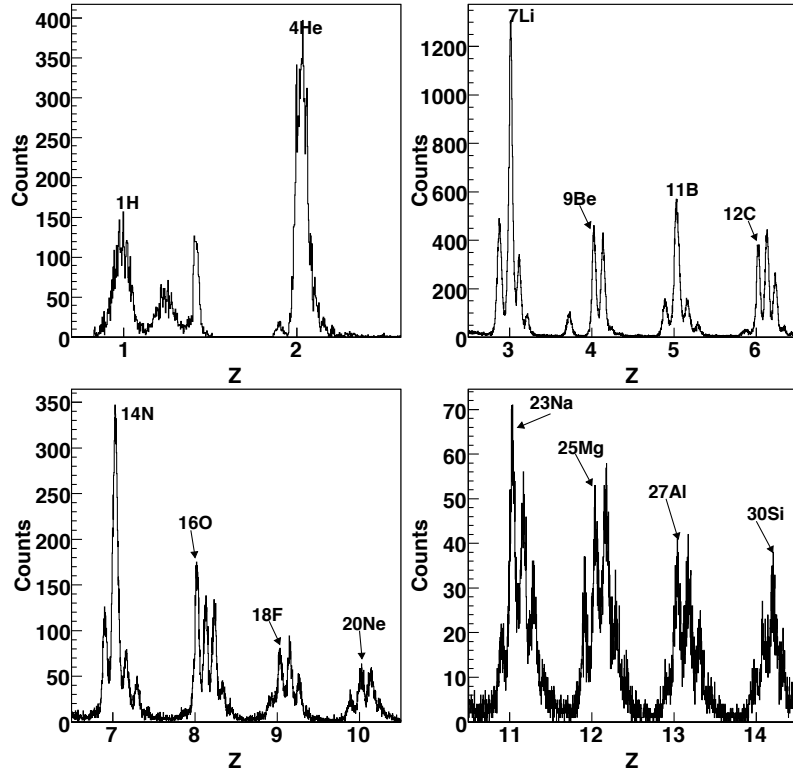
FIG. 10. Projected results of the linearization procedure. Z=1,2 are identified in the CsI fast-slow, Z=3-10 are representative of Si-CsI data, and Z= 11-14 were derived from a Si-Si data plot. [49]

element. For each data point, the distance to the two closest lines was calculated. The shorter distance was then normalized by the Z assigned to the two lines as well as the distance between the lines.

$$L_X = \frac{dist_1}{|dist_1 - dist_2|} Z_2 - \frac{dist_2}{|dist_1 - dist_2|} Z_1 \qquad (2.1)$$

$$L_X = \frac{dist_1}{|dist_1 + dist_2|} Z_2 + \frac{dist_2}{|dist_1 + dist_2|} Z_1 \qquad (2.2)$$

$$L_X = \frac{dist_2}{|dist_2 - dist_1|} Z_1 - \frac{dist_1}{|dist_2 - dist_1|} Z_2 \qquad (2.3)$$

Eqs. 2.1-2.3 define the normalization where L_X is the linearized X-axis value, $dist_{1,2}$
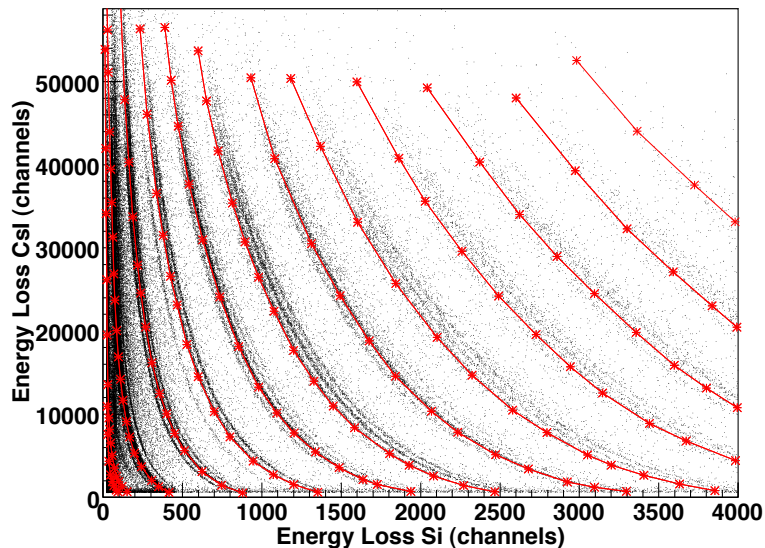
FIG. 11. Si-CsI raw data plot with overlayed user picked lines. (color online)

are the distances to the two closes lines, and $Z_{1,2}$ are elemental designations of these closest lines. The first normalization function (Eq. 2.1) is implemented for any point to the right of the right-most user chosen line. The second equation (Eq. 2.2) is used for any point that is between two lines. The final function (Eq. 2.3) is used for any point to the left of the left-most line. If the process performed well, a straight-line plot such as Fig. 12 was constructed. This plot shows linearized Z=3-7 fragments from a Si-CsI telescope.

The distance calculation method has an effect on the quality of the lineariza-tion [61]. A new distance calculation method was developed by May *et al.* [62] to mathematically determine the shortest distance (L_X) between a point and a polyno-mial curve. This function was implemented with excellent results.

After linearization, data was then projected onto an axis producing quasi-Gaussian peaks. The isotopic peaks in the projected distributions were fitted with Gaussian
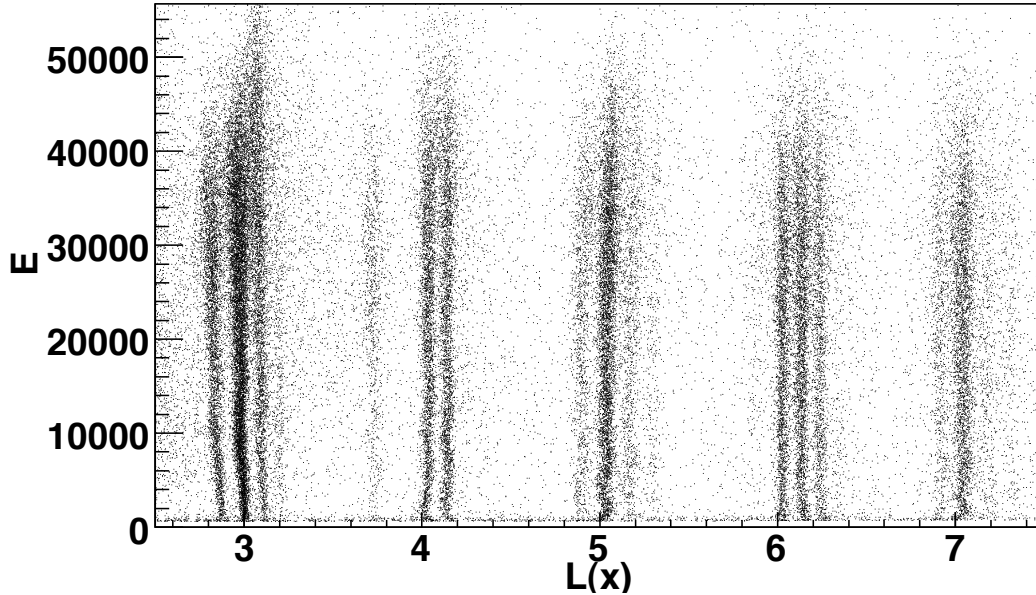
FIG. 12. Linearized Si-CsI plot. The X-axis (L_X) is normalized to Z and the Y-axis is related to energy in the CsI.

functions. The mass of each particle was assigned by determining the probability of the particle belonging to a given isotope. This probability (P_A) was calculated by comparing the value of the the isotopic Gaussian functions at the L_X value of the particle

$$P_A = \frac{G_A(L_X)}{\sum_i G_i(L_X)} \tag{2.4}$$

where G_A is the fit to the selected isotope which is compared to the summation over all Gaussians (G_i) of the element. For this thesis, a non-zero mass was defined only if the P_A was ≥ 0.75. This method of fitting the linearized data with Gaussians provided the ability to estimate the average contamination between neighboring isotopes. The contamination in the yield of a given isotope as defined here was calculated to be $\leq 5\%$ across all reaction systems and all detectors.

TABLE V. Calibration beams and targets.

Beam	H_2	H_2	^{4}He	^{2}0Ne	HD	HD
Target	Th (nat)	^{28}Si	Th (nat)	Th (nat)	Th (nat)	^{28}Si
Energy (Mev/u)	55	55	25	25	30	30

In this particle identification method the user defines the mass designation of each peak. Mass designations may be checked against published distributions such as those of Mocko or Souliotis [63, 64]. The Gaussian peak shape assumption is also important to note. The Gaussian shape assumption works very well for Si-CsI or Si-Si linearization. The shapes, however, can deviate somewhat for the pulse shape discrimination plots.

D. Calibration

After the particles were identified, the detectors were calibrated. External calibrations were provided by a ^{228}Th α source and calibration beams. The ^{228}Th calibration was taken immediately after the thesis data was acquired. However, the calibration beam data was acquired the following year. The list of calibration beams, targets, and energies are given in Table V and the table of elastic scattering energy versus ring for each beam is given in Appendix B. Only elastic scattering points were used for calibration.

The Si detectors were calibrated assuming a linear function. The calibration points were obtained from three sources: ^{228}Th αs, punch-in points, and punch-through points. In rings 2-7, the Si amplification was too low to take advantage of ^{228}Th calibration. However, the Si in rings 8-9 were calibrated using these α energies. The super telescope Si-Si were calibrated using punch-through points. These punch-

through points result from particles passing through both detectors and have well known energies. The telescope Si detectors were calibrated using punch-in points. Punch-in points correspond to the minimum energy required for a particle to pass through the Si and provide a signal in the CsI. The quality of the punch-in calibration depends on the software thresholds of the detector. Low detector thresholds provide the best values for this calibration. The punch-in and punch-through methods of calibration are compared in Fig. 13. These channel-energy calibration points are from a 500 μm super telescope Si detector. The calibration points obtained from each of these two methods were fit with linear functions which can be seen in the figure. The functions obtained are in good agreement with each other.

For Z>3, the total energy of the particle was derived from the energy lost in the silicon detector via an energy loss code. The extrapolation performs well for these fragments because a large fraction of the total energy is lost in the Si detector. The resulting total energy spectra were compared to those from a similar reaction [53] as well as the super telescopes at the same angle. Low Si electronic gains and high particle energy in ring 2 made deriving the total Z=3 energy from the Si problematic. For this reason, the ring 2, Z=3 total energy was derived from the CsI energy calculation. In all other rings, the Z=3 energy was derived from the Si energy loss.

The CsI calibration was based on the slow portion of the light output. The slow component was used because it is less likely than the fast component to saturate. The Tassan-Got [65] formula worked well for this data with a single set of parameters
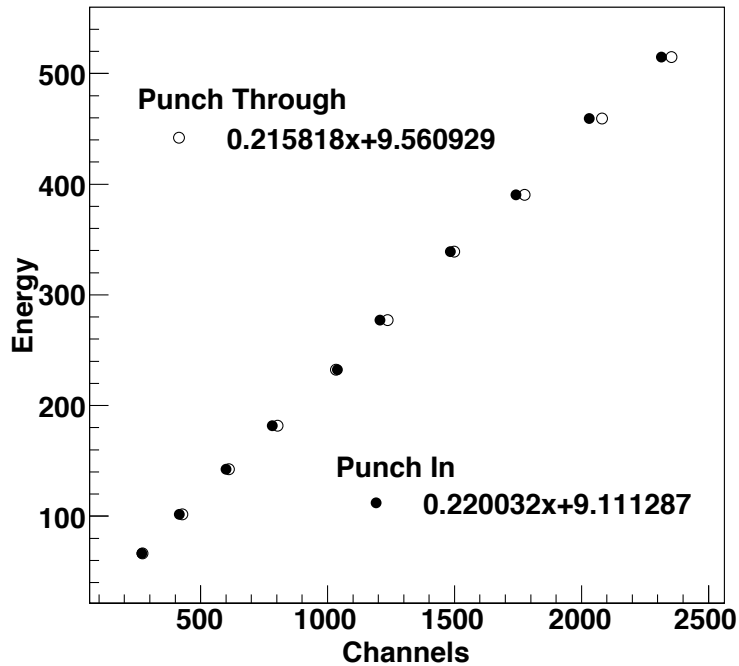
FIG. 13. Si calibration functions as for the punch in and punch through methods for a 500μm super telescope Si. Open symbols are punch in points and closed symbols are punch through points. The relevant calibration formulae are also shown.

for a small range of elements. The formula relates channel number to energy as:

$$E \quad = \quad \sqrt{h^2 + 2\rho h \left[1 + ln\left(1 + \frac{h}{\rho}\right)\right]}$$

where

$$h \quad = \quad (\text{ CsI light output - pedestal }) / \text{ scaling parameter} \qquad (2.5)$$

and

$$\rho \quad = \quad \eta Z^2 A.$$

The scaling parameter and η are both fitting parameters. In this data, Eq. 2.5 was fit to relate the channel-energy relationship for Z=1,2 simultaneously. The fitting

parameters were obtained using the calibration beam data points and spectra from a similar system [53] as references. Z=1,2 energy were obtained from the CsI calibration. In ring 2, the Z=3 energy was also derived from the CsI calibration though it was not included in the parameter fitting. Based on the CsI energy obtained from the calibration, the energy lost in the ΔE Si was derived from a code and added to the CsI energy to create a total energy for the fragment.

Example total energy spectra are shown in Fig. 14 for protons from ring 2 ($\sim$4 degrees in lab). The variation in spectrum starting energy on the left is the result of individual detector thresholds for proton detection and identification. The position of the spectrum peak along the X-axis is the result of a combination of the beam velocity, internal source temperature, and Coulomb acceleration of the protons. Above this peak, the spectrum falls off exponentially. Extended energy distributions are compiled in Appendix C.

E.   Physics Tapes

The particle identification logic flow chart is given in Fig. 15. Event by event, a buffer was filled with the data from all detectors that fired. The buffer was processed by looping over the CsI detectors. If a signal was found in the CsI, linearization was attempted. If the particle was successfully identified in the CsI linearization, it was then tested for energy thresholds. The lower threshold in the CsI was used to define the value at which the isotopic identification became useful. This is important because the lowest energy (least resolved) signals in the CsI are generally the best resolved signals in the Si-CsI. A particle within the lower and upper thresholds was then assigned a charge and mass using the Gaussian probability function (Eq. 2.4). In the CsI, ^{8}He particles fall in the same band as the double alpha particles. However, in
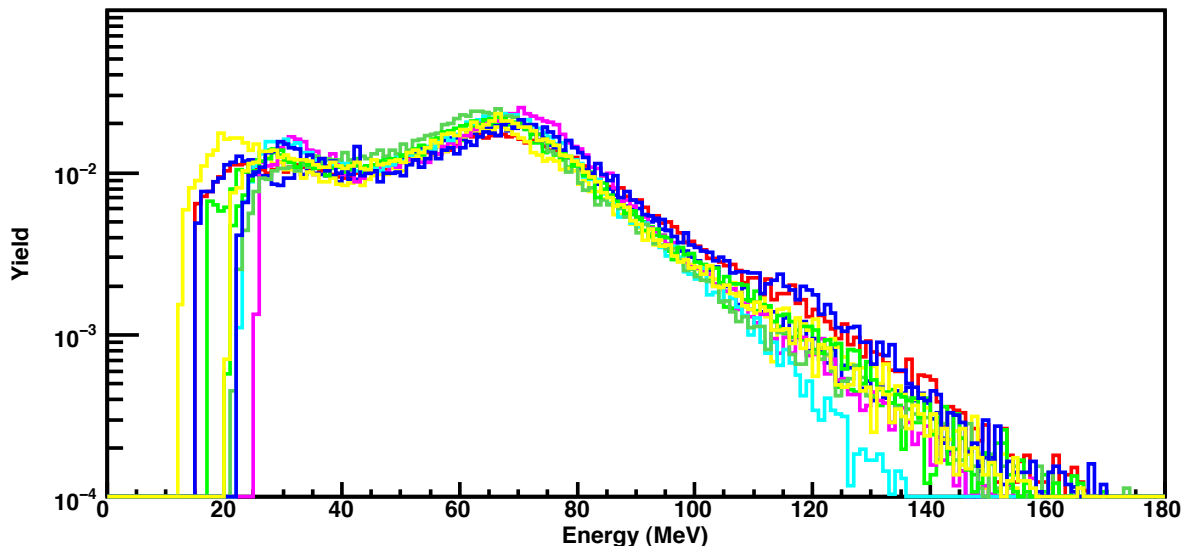
FIG. 14. Energy spectra for protons in ring 2. (color online)

the Si-CsI the particles identify as Z=2 for ^{8}He and Z=3 for the double alpha. Thus, particles that tested as ^{8}He in the CsI were also tested for Z=2 identification in the Si-CsI before being accepted. The CsI linearization was the primary identification source for Z=1,2 in all detectors. It was also the primary identification source for Z=3 in ring 2.

If identification was not assigned in the CsI, linearization was attempted on the Si-CsI. If the Si-CsI linearization was successful, the signal was tested with the upper and lower thresholds. Particles within the thresholds were assigned a charge and mass from the Gaussian probability function and retained in the event. In the Si-CsI, the threshold was placed directly below the lowest energy signals that could be clearly identified as above background. If the particle was Z<3, the charge identified in the Si-CsI was compared to that of the CsI. If the charges were equal, the particle was mass identified and retained. This cut was useful for eliminating high energy background
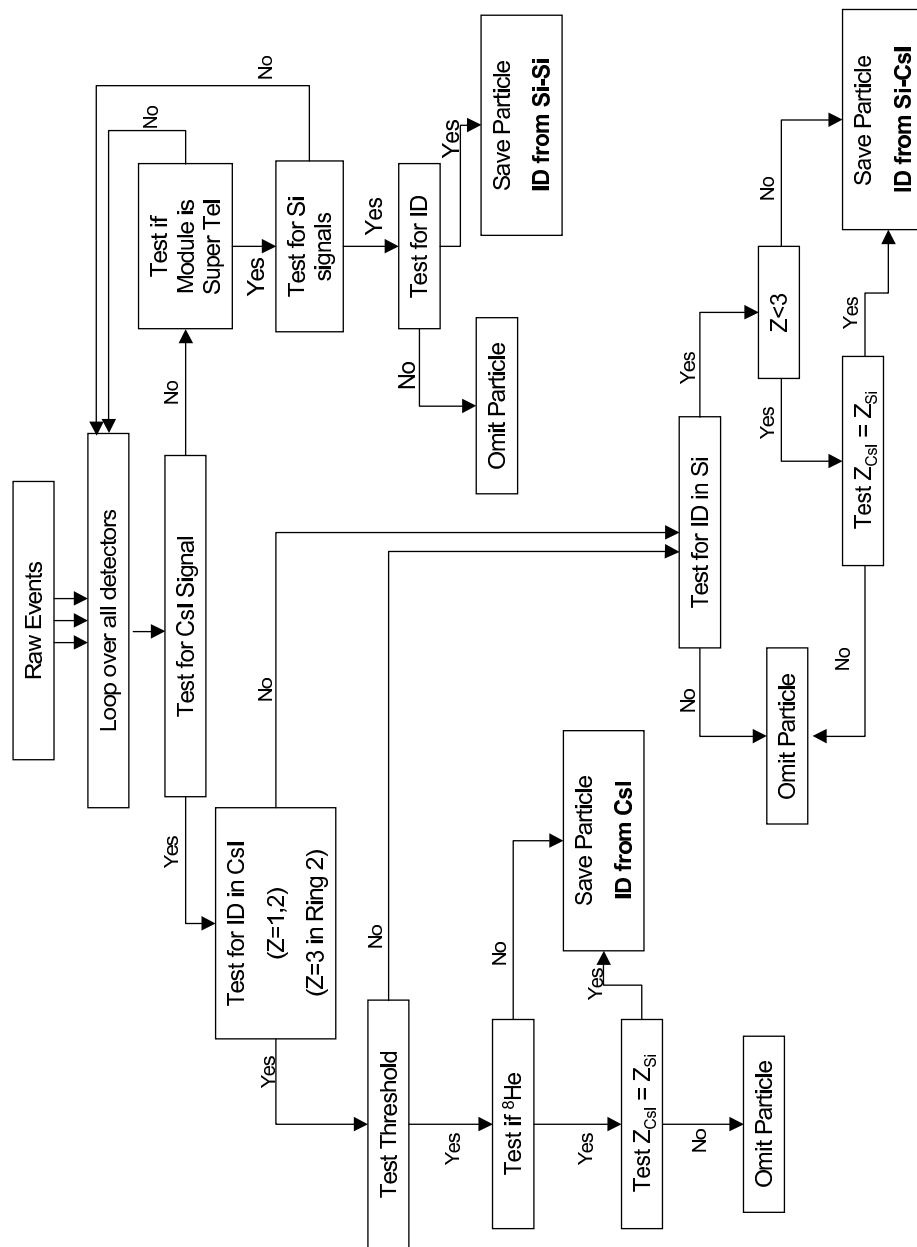
FIG. 15. Logical flow for particle identification designation.

in the low Z region of the Si-CsI plots. If the linearization was unsuccessful for the Si-CsI, the particle was omitted.

If the loop over detectors during an event did not find a signal in the CsI and the module was a super telescope, the Si detectors were checked for signals. If signals were present, then linearization was attempted. Successful linearization led to particle identification and retention in the output file. The mass was obtained from the most probable isotope identified from the Gaussian probability function (Eq. 2.4).

Two points should be highlighted about the physics tape logic. First, the thresholds for Si-CsI and CsI were important for maximizing isotopic resolution. The lowest energy signals in the CsI were the least resolved isotopically. Conversely, the lowest energy signals in the Si-CsI were the best isotopically resolved. Carefully placing the threshold on these two modes of particle identification maximized the isotopic resolution for Z=1,2 particles. The other issue of note is the removal of low level noise in the Si. If a particle identified as Z=1,2 in the Si-CsI, the Z was compared to the Z obtained in the CsI. If these did not agree, the particle was omitted. This cut was found to be effective in reducing low energy background in the Si-CsI detectors.

CHAPTER III

EVENT SELECTION

A well-defined source that covers a wide range of excitation energies should be used when studying phase transitions. Projectile fragmentation was chosen for this thesis because of its range of excitation energies with low effective energy thresholds for detecting particles of interest. The low effective energy threshold is the result of residual beam momentum and remains low for even relatively massive particles.

A projectile-like source should retain a velocity along the beam axis (V_z) similar to that of the projectile, have a sumZ (Eq. 3.1) of fragments similar to the Z of the projectile, and exclude mid-velocity, target-like, and pre-equilibrium particles. This chapter will step through the quasi-projectile (QP) source definition cuts and show the effect of the cuts on experimental and theoretical data. The HIPSE-SIMON [19] event generator provided quantitative information on the quality of the source definition.

$$sumZ = \sum_{i}^{fragments} Z_i \qquad (3.1)$$

The HIPSE-SIMON event generator has been shown to accurately simulate the energy and particle distributions in similar reactions measured by the INDRA detector [19]. Due to its similarity to the INDRA array, the code was used to understand the effect of software source cuts on the NIMROD-ISiS array. The theoretical data from HIPSE was de-excited by SIMON and passed through a software filter. This filter replicated the geometry, energy thresholds, and particle identification characteristics of the NIMROD-ISiS detector for the corresponding experimental data sets. The filter also addressed free neutron detection probabilities in the Neutron Ball.

A center of mass was constructed from the fragments detected in an event. The Z-axis velocity of this event center of mass is plotted in Fig. 16. There are no source cuts
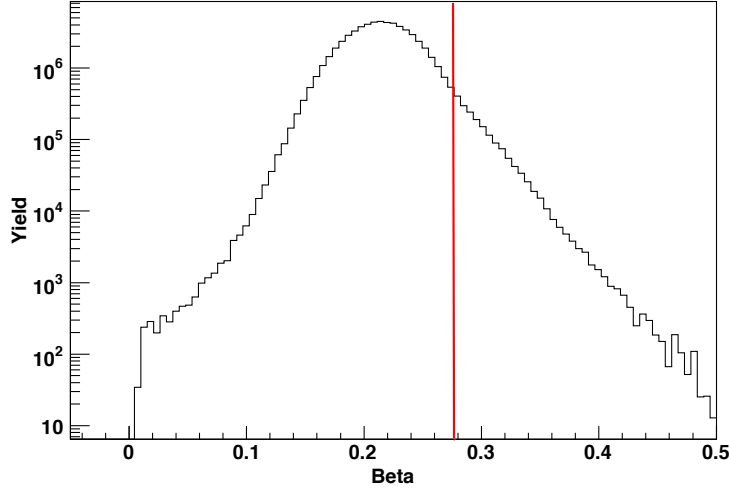
FIG. 16. Event center of mass velocity along the beam axis in units of c. V_{beam} is shown by the red line at 0.274c. Raw Data. (color online)

implemented on this data. The velocity of the beam (0.274c) along this axis is also shown. The data is clearly peaked slightly below the beam velocity and thus contains an enhanced concentration of projectile-like events. The breadth of this distribution likely results from a combination of detector geometry, threshold characteristics, and projectile-target dissipation effects during the interaction [66]. Dynamically emitted fragments result in the high energy tail seen on the right. The low energy tail is likely the result of very damped collisions between the target and projectile. The peak, slightly below the projectile velocity, is the projectile fragmentation peak.

The HIPSE-SIMON code provides fragments tagged with the relative quasi-projectile, quasi-target, or quasi-fusion sources. Fig. 17 is the distribution of fragment sources for filtered theoretical events without additional cuts. The sources are listed in Table VI with 0: quasi-fusion, 1: quasi-projectile, and 2: quasi-target. The dominance of the quasi-projectile source in Fig. 17 implies that a high fraction of particles
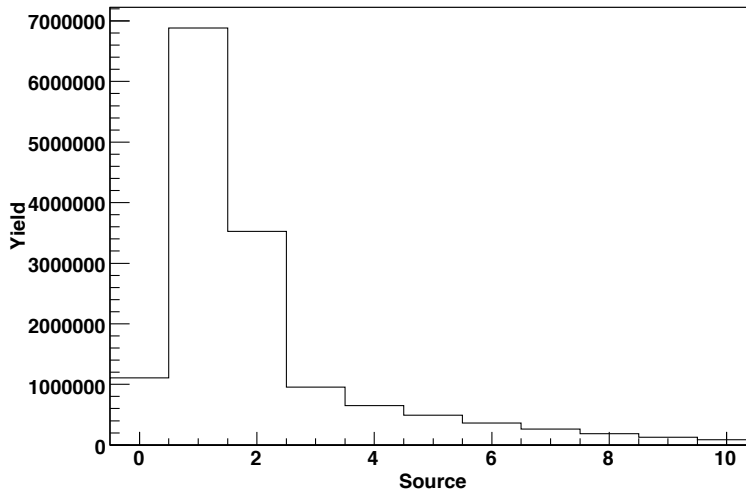
FIG. 17. Relative yield of fragments from quasi-projectile, quasi-target, and quasi-fusion sources in filtered theoretical data with no additional cuts. See Table VI for description of sources.

resulted from this source in the raw data. Figs. 16 and 17 show that the experimental configuration was successful in optimizing the fraction of particles from the quasi-projectile source.

The first software cut implemented was the sumZ$\geq$30 (Eq. 3.1) placed on raw events. Comparing Fig. 18 to Fig. 17 shows that the ratio of fragment sources does not change appreciably as a result of this cut. It is apparent that the primary result of this cut was to eliminate incompletely detected events and events not belonging to the projectile fragmentation mechanism. The effect of this cut on the experimental event velocity spectrum is shown in Fig. 19. The velocity of the center of mass of the detected particles is now approximately Gaussian in shape and positioned slightly below the velocity in the Z-axis (V_z) of the beam. Collectively, the remaining events are now beginning to look like the result of projectile fragmentation.

TABLE VI. Numerical particle source list as generated by HIPSE-SIMON and the corresponding particle source description.

Value	Source
0	Quasi-fusion
1	Quasi-projectile
2	Quasi-target
≥ 3	Other
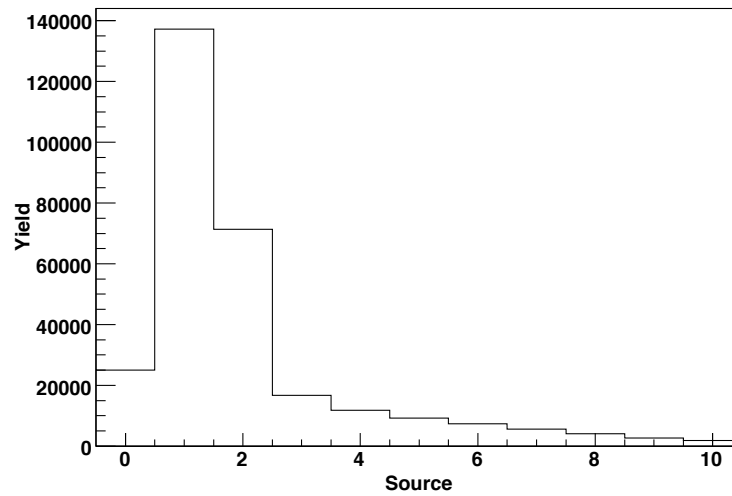
FIG. 18. Distribution of fragment sources present in filtered theoretical data with sumZ$\geq$30. See Table VI for description of sources.
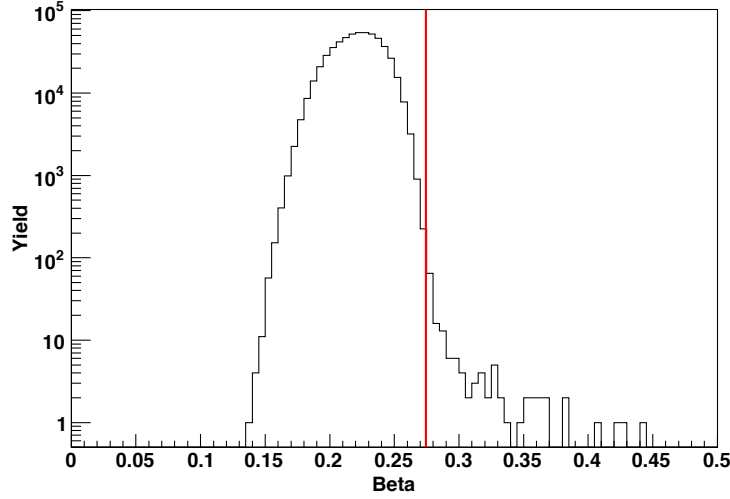
FIG. 19. Event center of mass velocity along the beam axis in units of c for reconstructed quasi-projecteiles with sumZ$\geq$30. V$_{beam}$ is shown by the red line at 0.274c. (color online)

Within an event, the fragments were analyzed individually to assess the likelihood of their belonging to a QP source. Particle sources can be visually identified in a plot of the fragment parallel versus perpendicular velocity (V$\parallel$V$\perp$). Fig. 20 is the Z=1,2 V$\parallel$V$\perp$ of experimental data after the sumZ$\geq$30 cut was applied. The velocity of the beam is shown at 0.274c. The data shows a concentration of fragments in this velocity region. However, the presence of particles at very high and low velocities indicates that the sumZ$\geq$30 cut was not sufficient to satisfactorily remove target-like and mid-velocity source fragments from the data.

A parallel velocity (V$_z$) cut was implemented to remove individual fragments that can not be reasonably associated with a QP source [67]. Within an event, the velocity in the beam direction of each particle was compared to the V$_z$ of the largest fragment. Fragments with relatively low or relatively high V$_z$ were associated with non-QP
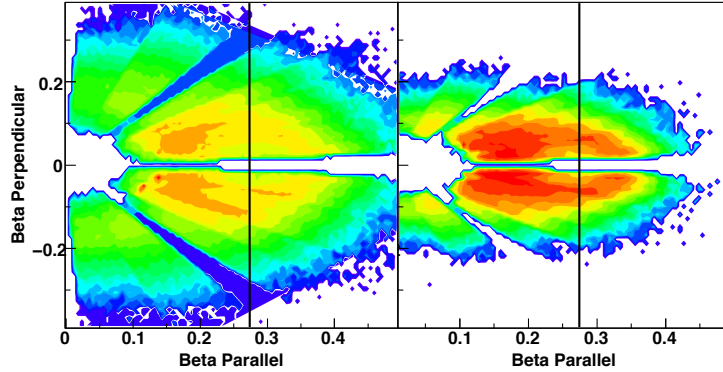
FIG. 20. Velocity in the beam axis versus velocity out of the beam axis in units of 1/c. Events have a sumZ≥30. The vertical black line is at the beam velocity. Left) Z=1 Right) Z=2 (color online)

sources. Velocity windows of ± 65%, 60%, and 45% (Z=1, Z=2, Z≥3 respectively) of V_z (largest fragment) were imposed on all particles in the experimental and theoretical data. Fig. 21 shows the effect of this cut on the Z=1,2 V‖V⊥ of experimental data. The velocity of the beam is shown and a strong concentration of fragments exist in this velocity region. The data no longer includes the most forward and backward velocities seen in Fig. 20. The improvement in the fraction of particles belonging to the QP source is shown in Fig. 22 where the relative fraction of quasi-projectile source particles was improved by approximately a factor of two over that of the quasi-target source particle yield. Narrower windows of velocity provided negligible improvement in the ratio of QP source in the theoretical data.

At this point it is reasonable to associate the selected events with an isolated quasi-projectile source. The event was transformed into the center of mass (COM) of the accepted fragments to determine the velocity and excitation energy (Eq. 3.2) of the fragmenting source. The momentum in the X, Y, and Z directions were summed across an event to determine the COM. The event COM velocity in each axis was
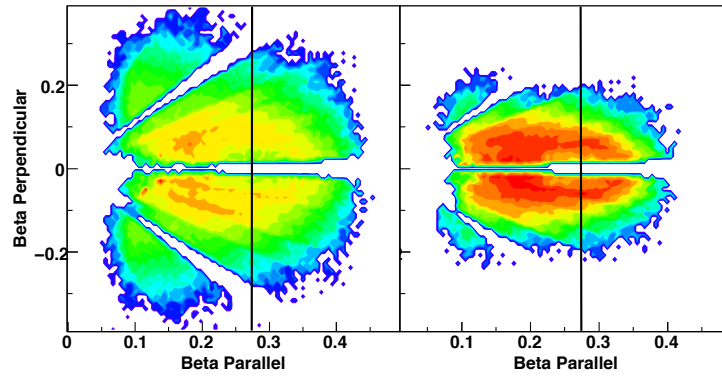
FIG. 21. Velocity in the beam axis versus velocity out of the beam axis in units of
1/c. Events have sumZ=30-34 and V_z cuts. The vertical black line is at the
beam velocity. Left) Z=1 Right) Z=2 (color online)
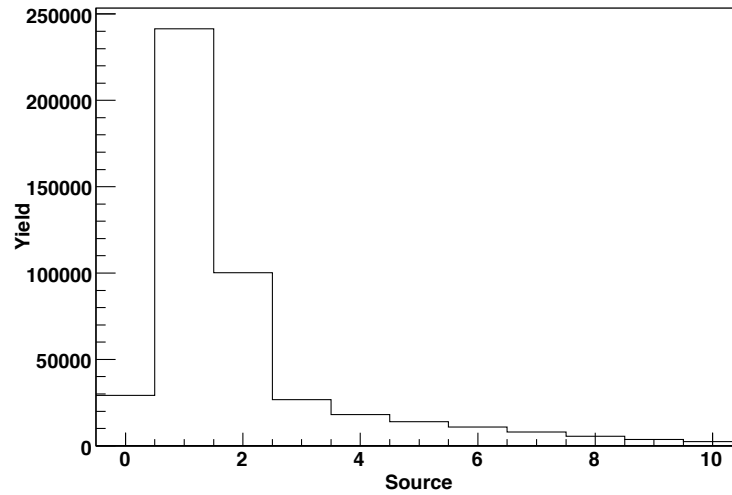
FIG. 22. Distribution of fragment sources present in filtered theoretical data with
sumZ=30-34 and V_z cuts. See Table VI for description of sources.

subtracted from each fragment's lab velocity. The kinetic energy of each fragment was then calculated from the velocity in the COM.

Reconstruction of the quasi-projectile allows us to calculate the excitation energy through calorimetry:

$$E^*_{source} = \sum_i^{M_{cp}} K_{cp}(i) + M_n \langle K_n \rangle - Q. \tag{3.2}$$

The excitation energy (E^*_{source}) was defined as the sum over the accepted particles' center of mass kinetic energy (K_{cp} and K_n) minus the reaction Q-value. The average kinetic energy of the neutrons was calculated as the proton average kinetic energy with a correction for the Coulomb barrier energy [68].

Proper calculation of the excitation energy should include the neutron and gamma energy corrections. The Neutron Ball provides an experimental neutron multiplicity per event that must be corrected for background, neutron source, and efficiency. The background provided by the pulser trigger is not correlated to any event. It, however, does provide a detector environment identical to that of a true event for background calculation. An additional background is collected with each event immediately after signal collection. The event background and pulser trigger backgrounds are plotted in Fig. 23. There is a strong similarity between these two distributions in peak position and overall shape. Thus the background correction was taken as the raw counts in the background gate corresponding to the event. The multiplicity of free neutrons was extracted from the experimental data using:

$$Mult_{QP} = \frac{Mult_{exp} - Mult_{bkg}}{(Eff_{QP} + \frac{N_T}{N_P} Eff_{QT})(.7/.6)}. \tag{3.3}$$

The multiplicity of neutrons assigned to the projectile source ($Mult_{QP}$) was calculated from the background ($Mult_{bkg}$) corrected experimental neutron multiplicity ($Mult_{exp}$). This multiplicity was then corrected using the relative efficiency of the Neutron Ball
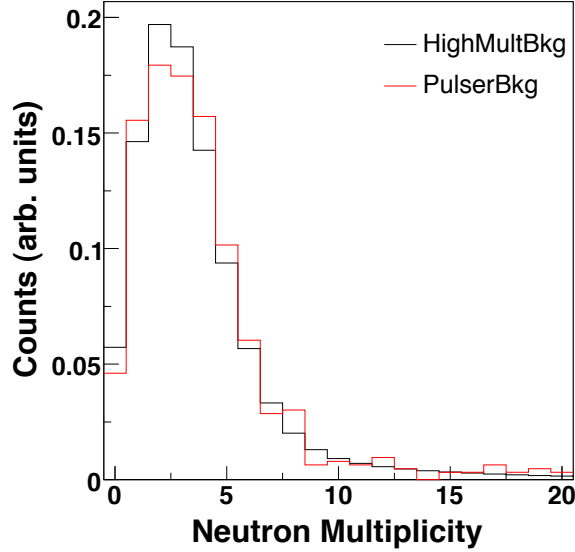
FIG. 23. Neutron background distributions. Pulser trigger background distribution (red) obtained from the first Neutron Ball signal gate for events triggered by the electronic pulser signal. High multiplicity trigger background (black) obtained event by event from the second Neutron Ball signal gate. (color online)

for detecting free neutrons emitted from a quasi-projectile (Eff_{QP}) and quasi-target (Eff_{QT}) for this reaction. The free neutron correction also accounted for the respective total neutron contributions from both the target (N_T) and projectile (N_P) nuclei. The efficiencies were extracted from tagged neutrons generated by the HIPSE-SIMON code and the GEANT3 simulation of the detector [30]. Simulation and filtering provided Eff_{QP}=0.65 and Eff_{QT}=0.40. The Neutron Ball was calibrated with a ^{252}Cf source to 70% efficiency for this experiment. The correction factor in the denominator accounts for the experimental calibration of the Neutron Ball to 70% efficiency rather than the 60% efficiency obtained from the GEANT3 simulation of the detector. Event by event, the Mult_{QP} provided an estimate of the free neutrons emitted from the quasi-projectile.

The energy carried away by gammas is generally considered to be small [11, 69]. In an effort to account for gamma energy, the ISiS collaboration calculated $E_\gamma = 1 MeV(Mult_{Z\geq3})$ [69]. However, this energy has not been constrained experimentally [70]. Using this formula the gamma energy is $\leq 1\%$ of the total excitation energy of the event. The gamma energy correction is not included in calorimetry for this thesis as it is small compared to that of the neutron and event energies and is poorly constrained.

A further cut was made on the data to improve its applicability to phase transition studies. Phase transition behavior is sensitive to the size of the studied system [28]. For this reason, the accepted events were required to have 30$\leq$sumZ$\leq$34 after the V_z cut.

To focus on events for which collective motion along the beam axis is minimized, the final cut constrained the shape of the event. The shape of each event was tested with the quantity

$$R = 2P_z^2/P_t^2 \tag{3.4}$$

where P_z is the momentum in Z-axis and P_t is the transverse momentum. On average, for a group of events, this quantity should equal one if the class of events is spherical. Limits were placed on the values of this ratio such that the mean for each excitation energy bin equaled 1$\pm$.05. This ratio was the final cut placed on the events. The resulting sphericity of the defined source can be seen in Fig. 24. The Y-axis corresponds to the momentum in the Z direction, the negative X-axis is momentum in the Y direction, and the positive X-axis is momentum in the X direction. The strong concentration of points around (0,0) indicates that the source is nearly symmetric in all directions. The strong sphericity of the source is consistent with a well-defined source without visible collective behavior along any axis.
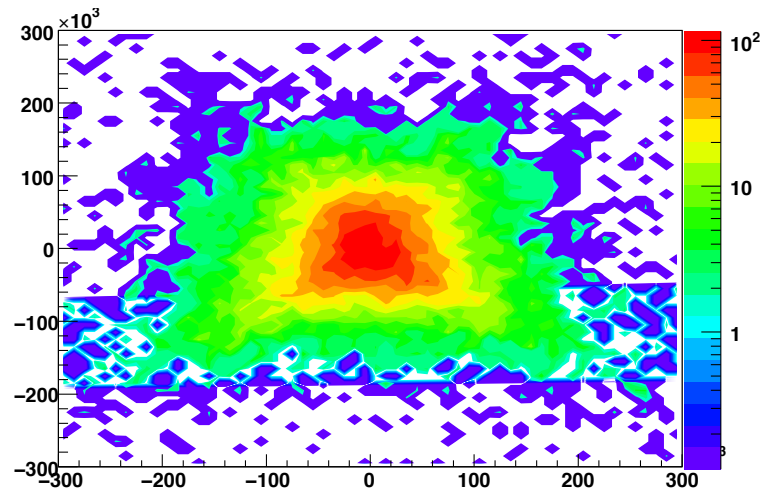
FIG. 24. Dalitz plot after all source cuts. The Y-axis corresponds to the momentum in the Z direction, the negative X-axis is momentum in the Y direction, and the positive X-axis is momentum in the X direction. (color online)

CHAPTER IV

TEMPERATURE FROM MOMENTUM FLUCTUATIONS

A new method of calculating the system temperature can be derived from the momentum fluctuations of particles in the center of mass frame of the fragmenting source. In this case, the frame is that of the reconstructed quasi-projectile. The momentum is constructed for each particle in the projectile frame center of mass for each axis. The momenta are then compared using Eq. 4.1

$$Q = 2P_z^2 - P_t^2 \tag{4.1}$$

where P_z^2 is the momentum in the Z-axis and P_t^2 is the transverse momentum. In an ideal, spherical, fragmenting source the sum of Q for all fragments in the event in the center of mass of that event should be a δ function at zero. However, in a real system fluctuations occur within a class of events. These fluctuations convert the momentum δ function into a distribution that can be characterized by a mean and width. In an equilibrated system, the mean should still equal zero.

The variance (σ^2) may be obtained from the distribution through

$$\sigma^2 = \left\langle Q^2 \right\rangle - \left\langle Q \right\rangle^2 \tag{4.2}$$

where Q is the quadrupole moment (Eq. 4.1). For a mean equal to zero, the second term cancels. Taking the first term as

$$\left\langle Q^2 \right\rangle = \int d^3p \left(2P_Z^2 - P_X^2 - P_Y^2 \right)^2 f(p) = \int d^3p \left(2P_Z^2 - P_T^2 \right)^2 f(p) \tag{4.3}$$

and assuming a Maxwellian distribution of the particles yields

$$\left\langle Q^2 \right\rangle = \frac{1}{(2\pi mT)^{3/2}} \int d^3p \left(4P_Z^4 - 4P_Z^2 P_T^2 + P_T^4 \right) e^{-\frac{P_Z^2 + P_X^2 + P_Y^2}{2mT}}. \tag{4.4}$$

A Gaussian integral is used

$$I_n(a) = \int_0^\infty x^n e^{-ax^2} dx \tag{4.5}$$

and the results that are of interest to this derivation are:

$$I_0(a) = \frac{1}{2}\sqrt{\frac{\pi}{a}} \tag{4.6}$$

$$I_2(a) = \frac{1}{4a}\sqrt{\frac{\pi}{a}} \tag{4.7}$$

$$I_4(a) = \frac{3}{8a^2}\sqrt{\frac{\pi}{a}}. \tag{4.8}$$

It is important to note that these integrals are only for 0 to ∞ and therefore should be doubled for $-\infty$ to ∞.

If we break Q^2 into three parts:

$$Part1 = \left(\frac{\pi}{a}\right)^{-3/2} \int dP_X e^{-aP_X^2} \int dP_Y e^{-aP_Y^2} \int dP_Z P_Z^2 e^{-aP_Z^2} \tag{4.9}$$

where

$$a = \frac{1}{2mT} \tag{4.10}$$

The first two terms, after being integrated from $-\infty$ to ∞ both equal

$$\sqrt{\frac{\pi}{a}} \tag{4.11}$$

The third term becomes:

$$\left(\frac{3}{4a^2}\right)\sqrt{\frac{\pi}{a}} \tag{4.12}$$

The product of these three terms yields:

$$Part1 = \frac{3}{4a^2}. \tag{4.13}$$

$$Part2 = \left(\frac{\pi}{a}\right)^{-3/2} \int d^3P P_Z^2 \left(P_X^2 + P_Y^2\right) e^{a\left(P_Z^2 + P_X^2 + P_Y^2\right)} \tag{4.14}$$

This yields:

$$\sqrt{\frac{\pi}{a}} \left(\frac{1}{2a}\sqrt{\frac{\pi}{a}}\right)^2 \tag{4.15}$$

$$Part2 = \frac{1}{2a^2} \tag{4.16}$$

$$Part3 = \left(\frac{\pi}{a}\right)^{-3/2} \int d^3P \left(P_X^2 + P_Y^2\right)^2 e^{a\left(P_Z^2 + P_X^2 + P_Y^2\right)} \tag{4.17}$$

$$Part3 = \left(\frac{\pi}{a}\right)^{-3/2} \int d^3P \left(P_X^4 + P_Y^4 + 2P_Y^2 P_X^2\right) e^{a\left(P_Z^2 + P_X^2 + P_Y^2\right)} \tag{4.18}$$

This yields:

$$2\left(\frac{3}{4a^2}\sqrt{\frac{\pi}{a}}\sqrt{\frac{\pi}{a}}\sqrt{\frac{\pi}{a}}\right) + 2\left(\left(\frac{1}{2a^2}\sqrt{\frac{\pi}{a}}\right)^2\sqrt{\frac{\pi}{a}}\right) \tag{4.19}$$

$$Part3 = \frac{2}{a^2} \tag{4.20}$$

Summing these three parts yields:

$$\sigma^2 = 4\left(\frac{3}{4a^2}\right) - 4\left(\frac{1}{2a^2}\right) + \frac{2}{a^2} = 12m^2T^2. \tag{4.21}$$

For a single fragment type from a nuclear multi-fragmentation:

$$\sigma^2 = 12A^2 m_0^2 T^2 \tag{4.22}$$

where m_0 is the mass of a nucleon and A is the mass number of the fragment. For multiple particle types, the formula becomes:

$$\sigma^2 = 12m_0^2 T^2 \sum_i (\zeta_i A_i)^2 \tag{4.23}$$
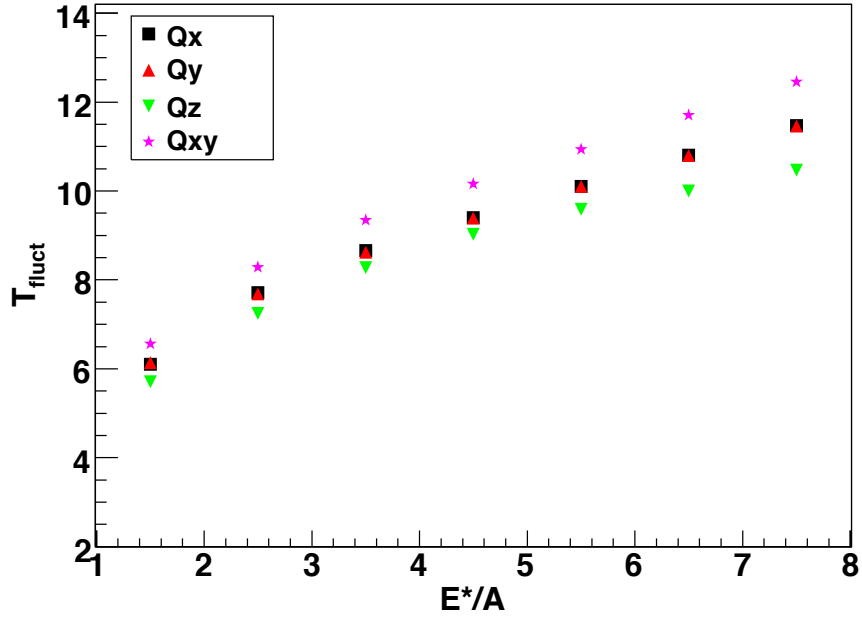
FIG. 25. Q_x, Q_y, Q_z and Q_{xy} (Eqs. 4.24 and 4.35) temperatures (Eqs. 4.23 and 4.36) as a function of E^*/A of the source event. (color online)

where ζ is the concentration of the particle in question.

The temperature evaluated from all fragments assigned to the quasi-projectile fragmentation event via Eq. 4.23 is shown in Fig. 25. Here the Q (Eq. 4.1) are defined as

$$
\begin{aligned}
Q_x &= 2P_x^2 - P_y^2 - P_z^2 \\
Q_y &= 2P_y^2 - P_x^2 - P_z^2 \\
Q_z &= 2P_z^2 - P_y^2 - P_x^2.
\end{aligned}
\qquad (4.24)
$$

The statistical error bars are smaller than the size of the points in Fig. 25. The Q_x, Q_y thermometers are identical within errors and the Q_z thermometer is slightly lower. In spite of the velocity and shape source cuts, the Z-axis does not exhibit the

same momentum distributions as are seen in the X,Y-axes. This behavior is likely the result of residual collective motion along the beam axis. Thus, when this axis is used to calculate Q_x, Q_y, or Q_z the distributions are contaminated by the remaining collective behavior.

To remove the collective behavior present in the Z-axis from the temperature calculation, the temperature was re-derived using only the X and Y-axes and employing the same Maxwellian distribution and Gaussian integral assumptions. Here Q^2 is defined as

$$Q^2 = \int d^2p \left(P_X^4 - 2P_X^2 P_Y^2 + P_Y^4 \right) f(p) \tag{4.25}$$

and after the Maxwellian distribution assumption becomes

$$Q^2 = \frac{1}{(2\pi mT)} \int d^2p \left(P_X^4 - 2P_X^2 P_Y^2 + P_Y^4 \right) e^{-\frac{P_X^2 + P_Y^2}{2mT}}. \tag{4.26}$$

If we break Q^2 into three parts and implement Gaussian integrals (Eq. 4.5):

$$Part1 = \left(\frac{\pi}{a} \right)^{-1} \int dP_X P_X^4 e^{-aP_X^2} \int dP_Y e^{-aP_Y^2} \tag{4.27}$$

where

$$a = \frac{1}{2mT} \tag{4.28}$$

$$Part3 = \left(\frac{\pi}{a} \right)^{-1} \int dP_Y P_Y^4 e^{-aP_Y^2} \int dP_X e^{-aP_X^2} \tag{4.29}$$

where

$$a = \frac{1}{2mT} \tag{4.30}$$

Part1 equals Part 3 and the sum of them becomes

$$\frac{3}{2a^2}. \tag{4.31}$$

$$Part2 = 2\left(\frac{\pi}{a}\right)^{-1} \int dP_X P_X^2 e^{-a\left(P_X^2\right)} \int dP_Y P_Y^2 e^{-a\left(P_Y^2\right)}. \tag{4.32}$$

This yields:

$$-\frac{1}{2a^2}. \tag{4.33}$$

Summing these three parts yields:

$$\sigma^2 = \frac{1}{a^2} = 4m^2T^2. \tag{4.34}$$

For a single fragment type from a nuclear multi-fragmentation:

$$\sigma^2 = 4A^2 m_0^2 T^2 \tag{4.35}$$

where m_0 is the mass of a nucleon and A is the mass number of the fragment. For multiple fragment types,

$$\sigma^2 = 4m_0^2 T^2 \sum_i \left(\zeta_i A_i\right)^2 \tag{4.36}$$

where ζ is again the concentration of a given particle type. The temperature is now linked to the variance through Eq. 4.36 and the caloric curve obtained using the Q_{xy} fluctuations is plotted in Fig. 25. This thermometer provides a higher source temperature across all excitation energies than was obtained using the Q_x, Q_y, or Q_z thermometers. This difference in temperature is the result of removing the remaining collective behavior along the Z-axis.

Combining all of the fragments together to create a Q distribution depends on the assumption that all of the fragments, regardless of mass or charge, have the same distribution width. This implies a simultaneous, statistical emission of fragments. The temperatures obtained from the Q_{xy} distributions for selected particle types are plotted as a function of excitation energy in the top panel of Fig. 26. Though the temperature increases with excitation energy regardless of particle type, there is a

significant spread in measured temperature across the fragment types.

Three Li isotopes have been plotted in the middle panel of Fig. 26 to provide a mass comparison at constant Z. These Li isotopes agree well across most excitation energies and show only a small mass dependence. A more significant mass dependence at constant Z may be seen in the ^{3,4}He isotopes plotted in the bottom panel of Fig. 26. The ^{3}He yields a $\sim$35% higher temperature than the ^{4}He across all E*/A. The ^{4}He apparent temperatures show a $\sim$15% increase across E*/A= 1.5–7.5. The ^{3}He temperatures, on the other hand, increase by $\sim$50% across the same E*/A region.

To observe the change in measured temperature at constant mass and differing charge, the apparent temperatures of ^{3}He and ^{3}H are plotted in the bottom panel of Fig. 26. The ^{3}He observed temperatures are $\sim$35% higher than those of the ^{3}H across all E*/A. However, the rate of increase is $\sim$50% for both of these isotopes across E*/A= 1.5–7.5.

It is possible that some of the mass dependence of the apparent temperature is the result of differential fragment emission time. This is particularly likely for the difference seen in the He isotopes. It is known that ^{3}He is emitted early in the fragmentation process. Conversely, ^{4}He is emitted throughout the de-excitation cascade [71].

The difference in measured temperature seen in the A=3 isotopes may indicate a Coulomb contribution to the momentum distributions widths. A Coulomb contribution to the fragment widths should increase with fragment Z. However, the ^{10}B and ^{12}C exhibit higher variances and temperatures than ^{16}O. This indicates that Coulomb repulsion cannot be the entire explanation to the momentum distribution width dependence on fragment type.

The momentum distributions may also be widened by recoil during the source break up. The recoil effect on the momentum Q distributions has been parameterized
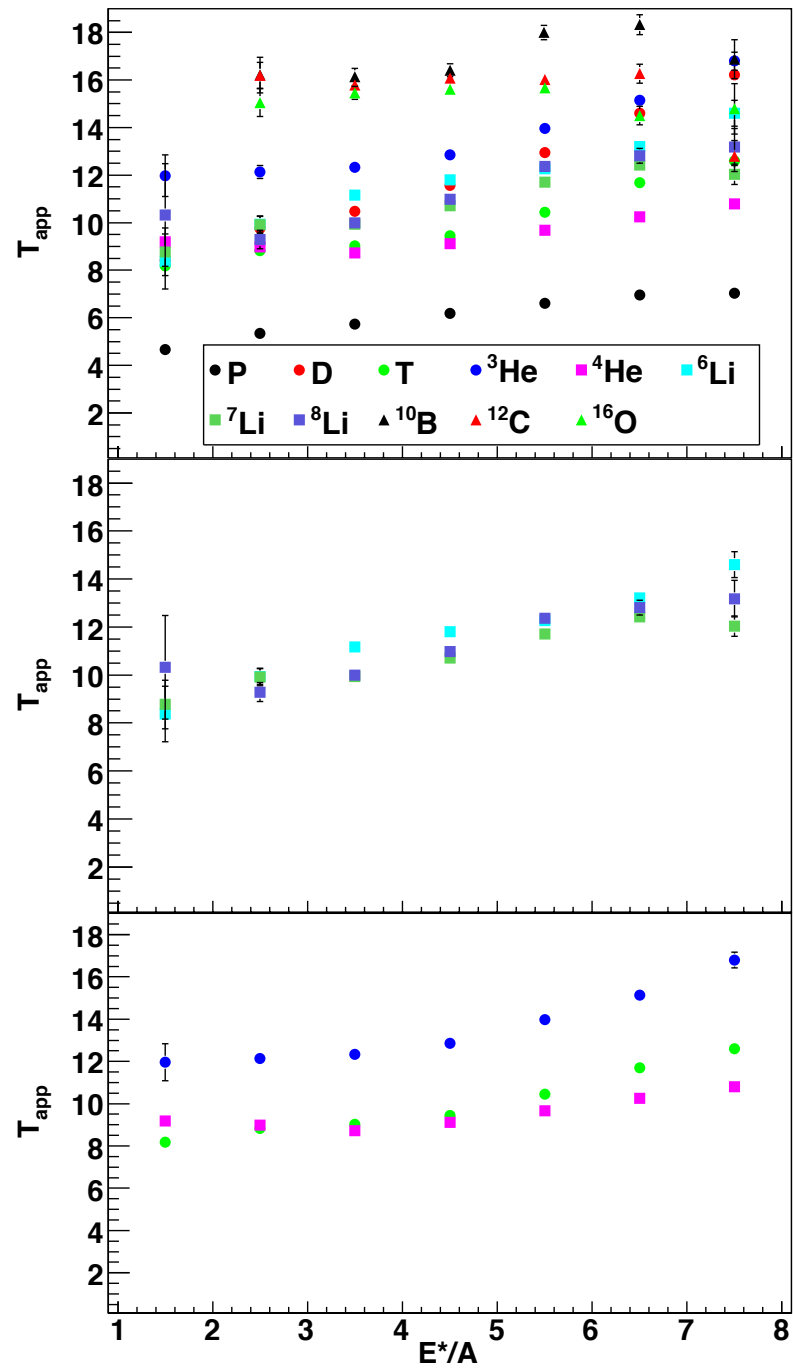
FIG. 26. Apparent temperatures extracted from the Q_{xy} distributions as a function of particle type. (color online)
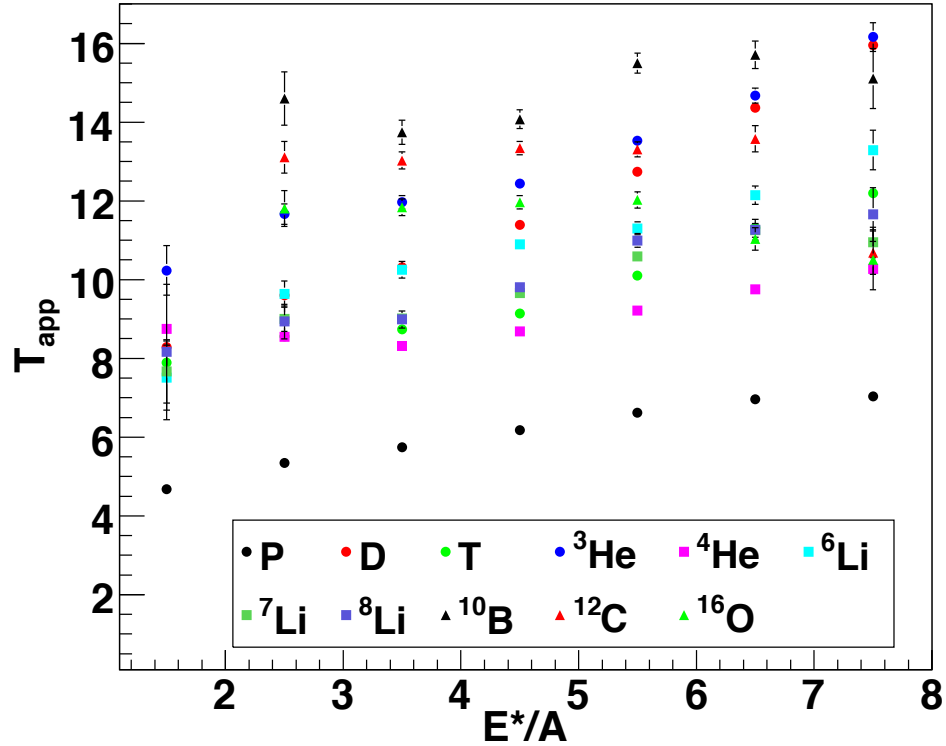
FIG. 27. Apparent temperatures extracted from the recoil corrected Q_{xy} distributions as a function of particle type. (color online)

as

$$Q_{xy(0)} = Q_{xy(app)}\left(\frac{A - A_f}{A - 1}\right) \tag{4.37}$$

where $Q_{xy(0)}$ is the recoil corrected value, $Q_{xy(app)}$ is the experimental value (Eq. 4.36), A is the mass of the source, and A_f is the mass of the fragment being considered [42]. The apparent temperatures obtained from the recoil corrected Q_{xy} distributions as a function of particle type and source excitation energy are plotted in Fig. 27. This figure shows that the recoil correction decreased the variation in the momentum distribution widths slightly as a function of particle type. Even after recoil correction, the Coulomb repulsion still cannot explain the mass dependence of this thermometer as the ^{10}B and ^{12}C still exhibit higher temperatures than ^{16}O does.

In addition to the above mentioned factors, the temperature obtained with this thermometer could be a combination of thermal energy and Fermi momentum in the detected fragments [42]. Following the paper of Bauer, the measured fragments exhibit a momentum distribution resulting not only from thermal sources but also the Fermi momentum of the component nucleons. This effect increases as a function of fragment size until a limiting value is observed. This correction is only meaningful for fragments with A$\geq$2. Thus, the momentum distributions of protons are free of this complication.

The caloric curve derived from the proton momentum fluctuation widths of the ^{86}Kr+^{64}Ni system is plotted in Fig. 28. The fluctuations for this thermometer were measured along the X,Y-axes. For reference, the compilation of Natowitz et $al.$ [28] and two Fermi Gas curves (T $= \sqrt{aE^*/A}$ with a = 8, 13) are plotted. As shown in this figure, the protons produce temperatures similar to what is obtained from a Fermi Gas at low E*/A indicating that this thermometer does indeed yield reasonable temperature values. The errors plotted in Fig. 28 for the Y-axis are estimated systematic errors of 0.5 MeV.

Four momentum thermometers have been defined in this chapter (Eqs. 4.24, 4.36). The first three (Q_x, Q_y, and Q_z) should theoretically be degenerate. However, the Z-axis was found to contain residual collective behavior. This contaminated all three of these thermometers. To remove the collective behavior along the Z-axis, the temperature was then derived using only the X and Y-axes. This thermometer provides a slightly higher temperature reflecting the removal of the Z-axis with its incorrect width. The high value of T obtained from this thermometer may be a result of Fermi momentum in the fragments. This effect is zero for protons. The proton caloric curve is shown in Fig. 28. This proton based Q_{xy} thermometer, in conjunction with the slope (Eq. 1.4) and double isotope (Eq. 1.6) thermometers, will be used in the next
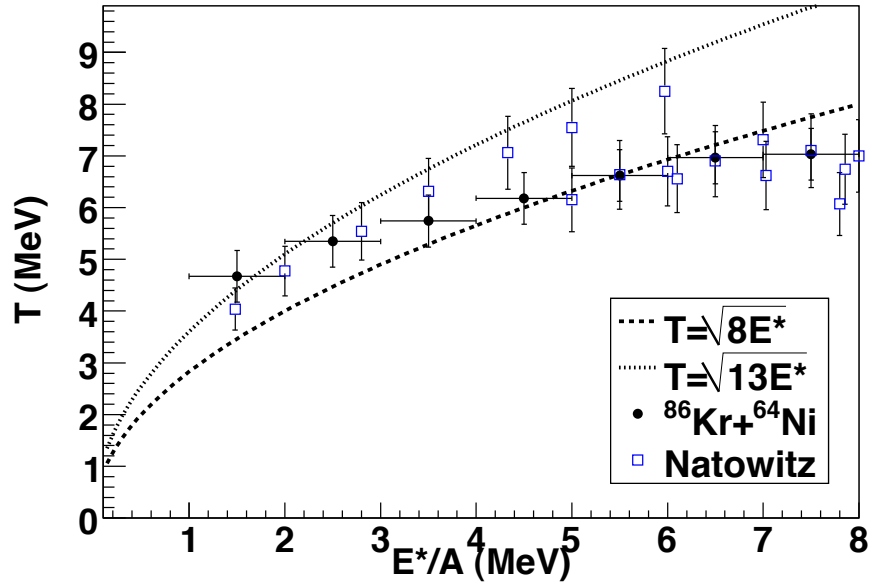
FIG. 28. Q_{xy} (Eq. 4.35) temperatures derived from proton momentum fluctuations as a function of E^*/A of the source event. For reference the caloric curve for A=60-100 from the Natowitz compilation [28] as well as two Fermi Gas (T $= \sqrt{aE^*/A}$ with a = 8, 13) curves are plotted. (color online)

chapter to investigate the N/Z dependence of the nuclear caloric curve.

CHAPTER V

CALORIC CURVES

A major challenge for experimentally investigating the asymmetry term of the nuclear equation of state is to accurately determine the neutron-to-proton ratio (N/Z) of the fragmenting source. By combining the excellent isotopic resolution in the NIMROD-ISiS array and experimental free neutron multiplicities obtained from the Neutron Ball a quasi-projectile can be reconstructed in both charge and mass. In this chapter we will investigate the effect of the experimentally determined source N/Z on the caloric curve.

Often, in studies requiring knowledge of the source N/Z, this quantity has been estimated via a theoretical code or assumed to be equal to the N/Z of the composite system or the projectile [13]. However, several years ago, a significant effort was made by Rowland et $al.$ [31], to reconstruct the charged particles resulting from a quasi-projectile break-up of A=20 systems. The source N/Z was calculated from the summation of the neutrons and protons bound in the detected charged particles:

$$\frac{N}{Z}_{bound} = \frac{\sum_i^{M_{cp}} N_i}{\sum_i^{M_{cp}} Z_i}. \tag{5.1}$$

The reconstructed quasi-projectile N/Z$_{bound}$ from the reactions of ^{86}Kr+^{64}Ni and ^{78}Kr+^{58}Ni are shown in Fig. 29. The N/Z of ^{86}Kr is 1.38 and the N/Z of ^{78}Kr is 1.16. The centroid of the reconstructed quasi-projectile N/Z$_{bound}$ distributions show a shift away from the N/Z of the projectile towards the valley of stability. The N/Z$_{bound}$ distribution widths are the result of neutron and proton exchange during the projectile-target interaction. The widths and means have been estimated by fitting with a Gaussian function. The ^{86}Kr+^{64}Ni mean is 1.07 with a σ of 8.0e-2. The ^{78}Kr+^{58}Ni mean is 0.99 with a σ of 7.6e-2. The width of the N/Z$_{bound}$ distributions

FIG. 29. N/Z$_{bound}$ distribution for the most neutron rich and most neutron poor reacting systems. Triangles are ^{86}Kr+^{64}Ni and squares are ^{78}Kr+^{58}Ni. Five bins were placed on the N/Z$_{bound}$: 0.9–0.96 (bin 1), 1.0–1.06 (bin 2),1.1–1.16 (bin 3), 1.2–1.26 (bin 4), and 1.3–1.36 (bin 5). (color online)

are large, particularly as compared to the difference between the average N/Z$_{bound}$ of the two reaction systems. Five bins in N/Z$_{bound}$ were placed on these distributions regardless of the reacting system: N/Z$_{bound}$ = 0.9–0.96 (bin 1), 1.0–1.06 (bin 2),1.1–1.16 (bin 3), 1.2–1.26 (bin 4), and 1.3–1.36 (bin 5). These bins provide a more precise source N/Z than the beam-target combinations for comparing observables.

The isoscaling [30] observable in Fig. 30 shows the effect of improving the precision of the source N/Z definition. In heavy-ion collisions, fragment yield ratios R$_{21}$(N,Z), obtained from two reactions, have been shown to exhibit an exponential dependence on the neutron (N) and proton (Z) numbers of the fragments. This scaling was derived assuming a statistical fragment production mechanism where two

reactions are occurring at the same temperature and differ only in their isospin asymmetry [72, 73, 74]. The ratios are defined as

$$R_{21}(N, Z) = Y_2(N, Z)/Y_1(N, Z) = Cexp(N\alpha + Z\beta) \qquad (5.2)$$

where α and β are the fitting parameters and C is an overall normalization constant. Traditionally, reaction 2 corresponds to the more neutron-rich source and reaction 1 to the less neutron-rich source. This scaling behavior is called isotopic scaling or isoscaling [73], and has been observed in a variety of reactions [72, 75, 76, 77].

The top panel of Fig. 30 is isoscaling with reconstructed quasi-projectiles from ^{86}Kr+^{64}Ni as the neutron-rich and ^{78}Kr+^{58}Ni as the neutron-poor sources (system-to-system). The fragment yield ratios for each element are plotted with a different symbol and the fit of Eq. 5.2 to the yield ratios of each element are depicted by the solid lines. An overall value of α=0.245 and β=-0.266 were obtained by globally fitting across all isotopes and elements. While some scaling behavior is present, the isoscaling is not of exceptional quality.

The middle panel of this same figure shows the quality of isoscaling observed using well defined and separated bins of quasi-projectile N/Z$_{bound}$. The data from each beam/target combination was cut using reconstructed quasi-projectile N/Z$_{bound}$ bins of 1.0 - 1.06 (bin 2) and 1.2 - 1.26 (bin 4) to construct the neutron-poor and neutron-rich sources of Eq. 5.2. Similar isoscaling behavior was observed from each beam-target combination; thus, the reaction systems were added together to increase statistics. The ratio of the isotopic yields from the combined systems for Z=1-17 as a function of neutron number is shown in the middle panel of Fig. 30 using N/Z$_{bound}$ bin 2 and bin 4. As in the system-to-system isoscaling, the lines are the result of individually fitting each element with Eq. 5.2. The global fit isoscaling parameter α for this plot is 0.912 and the β parameter is -1.089. The range in N/Z$_{bound}$ in bins
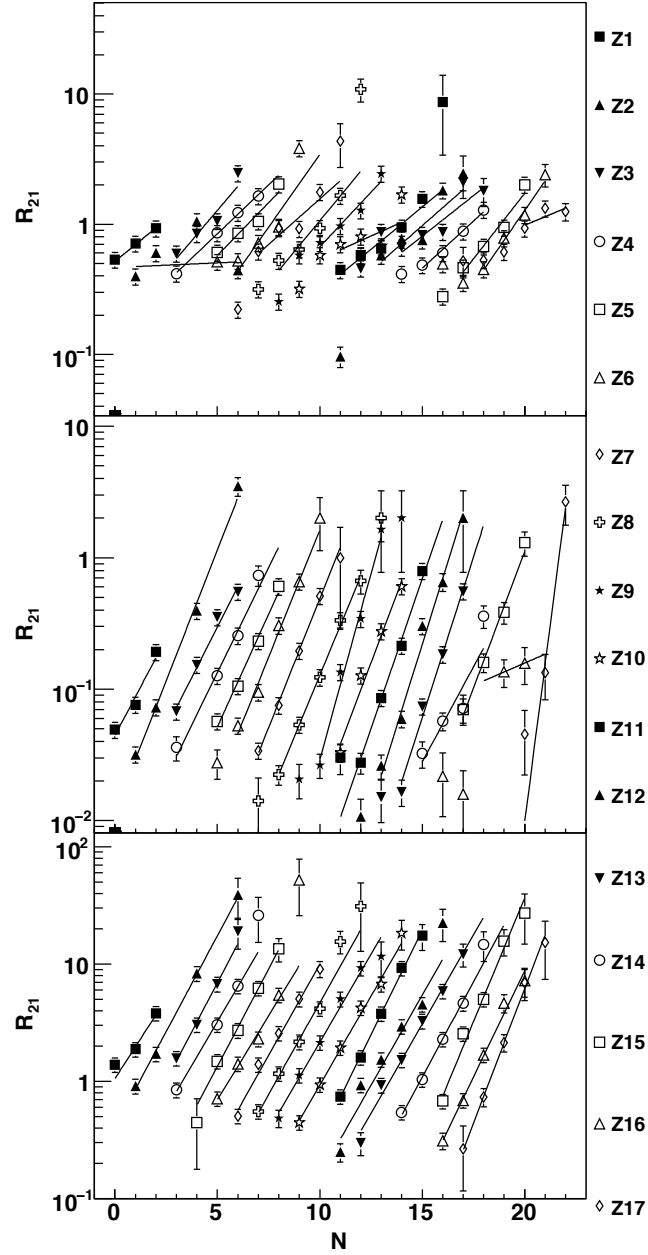
FIG. 30. Global Ratios no E∗ cuts. Top: System to system isoscaling ^{86}Kr+^{64}Ni, ^{78}Kr+^{58}Ni. Middle: Isoscaling using neutron-rich and neutron-poor bins on the reconstructed, N/Z$_{bound}$ of the quasi-projectiles from all four reaction systems (^{86,78}Kr+^{64,58}Ni). Bottom: isoscaling using bins of 1.0 - 1.06 (bin 2) and 1.2 - 1.26 (bin 4) on the reconstructed, N/Z$_{meas}$ of the quasi-projectiles from all four reaction systems (^{86,78}Kr+^{64,58}Ni). (see text)

2 and 4 is ~25% of the difference between the means of these two bins. The clear improvement in the isoscaling between the top and middle panels demonstrates the importance of precisely defining the N/Z of the source.

To access the nuclear symmetry energy from isoscaling, free neutrons emitted by the source must be accounted for. Attempts have been made to account for the undetected neutrons by using a source N/Z derived from the reacting systems [75] or from theoretically corrected N/Z_{bound} [78]. The current data, however, includes experimentally detected neutrons from the Neutron Ball [49] thereby allowing an experimentally based determination of the source N/Z:

$$\frac{N}{Z}_{meas} = \frac{\sum_i^{M_{cp}} N_i + M_n}{\sum_i^{M_{cp}} Z_i}. \tag{5.3}$$

The multiplicity of free neutrons (M_n)was extracted from the experimental data using Eq. 3.3.

The N/Z_{meas} of the reconstructed quasi-projectiles from the ^{86}Kr+^{64}Ni and ^{78}Kr+^{58}Ni reaction systems are plotted in Fig. 31. The widths and means have again been esti-mated by fitting with a Gaussian function. The mean of the ^{86}Kr+^{64}Ni distribution is 1.26 with a σ of 9.3e-2, and the mean of the ^{78}Kr+^{58}Ni is 1.12 with a σ of 8.6e-2. The difference between the means of the ^{86}Kr+^{64}Ni and ^{78}Kr+^{58}Ni N/Z_{meas} distributions is larger than was observed for the N/Z_{bound} distributions of these two systems.

The effect of free neutron correction is shown by placing bins of N/Z_{meas} equal to 1.0 - 1.06 (bin2) and 1.2 - 1.26 (bin4) on the reconstructed quasi-projectiles. The resulting isoscaling is shown as the bottom panel of Fig. 30. The consistency and linearity of the elemental lines are notable, especially in light of the wide range in asymmetry of isotopes shown for each element. Each element has been fitted indi-vidually with Eq. 5.2. A global fit across isotopes and elements to obtain α and β produced 0.733 and -0.841 respectively.
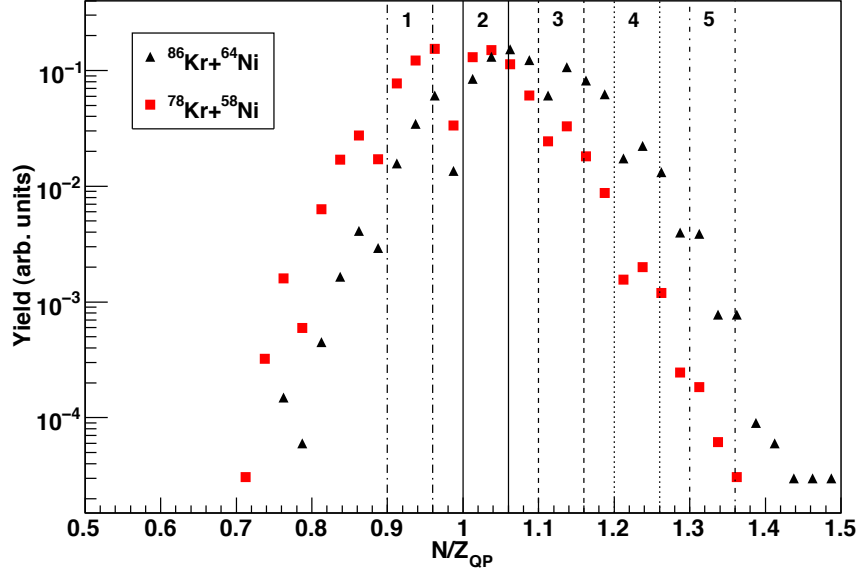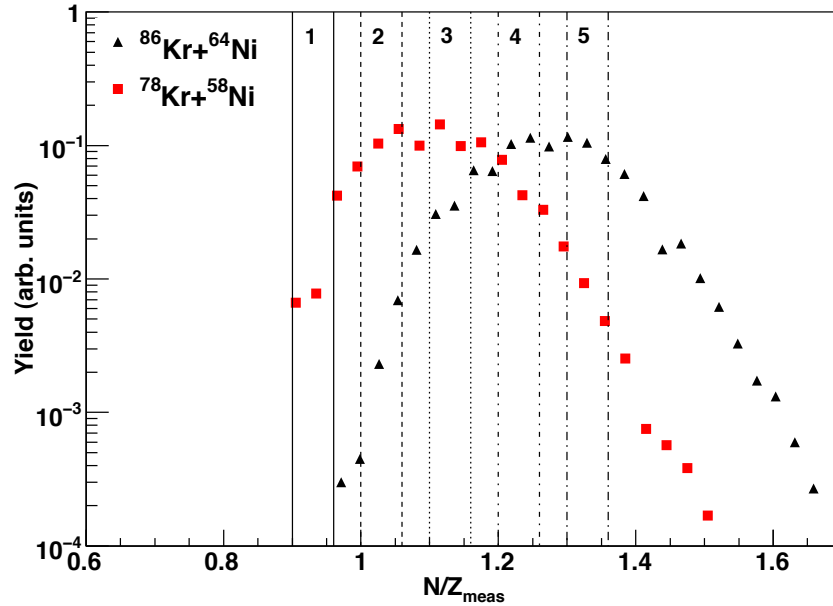
FIG. 31. N/Z_{meas} distribution for the most neutron rich and most neutron poor react-
ing systems. Triangles are ^{86}Kr+^{64}Ni and squares are ^{78}Kr+^{58}Ni. Six bins
were placed on the N/Z_{QP}: 0.9–0.96 (bin 1), 1.0–1.06 (bin 2),1.1–1.16 (bin
3), 1.2–1.26 (bin 4), 1.3–1.36 (bin 5), and 1.4–1.46 (bin 6). (color online)

The isoscaling has shown that observables are dependent on the N/Z_{meas}. This
dependence carries over to reaction system dependence to the extent that the sys-
tems populate different ranges in N/Z_{meas}. As above, the four reaction systems are
combined to provide maximum statistics. The N/Z_{meas} distribution of the combined
systems is shown in Fig. 32. Six bins were placed on this distribution regardless of
the reacting system: N/Z_{meas} = 0.9–0.96 (bin 1), 1.0–1.06 (bin 2),1.1–1.16 (bin 3),
1.2–1.26 (bin 4), 1.3–1.36 (bin 5), and 1.4–1.46 (bin 6).

Three thermometers were investigated to study the source N/Z dependence of
the nuclear caloric curve: the double isotope method, the slope method, and the
momentum fluctuations method. The double isotope temperature is obtained via the
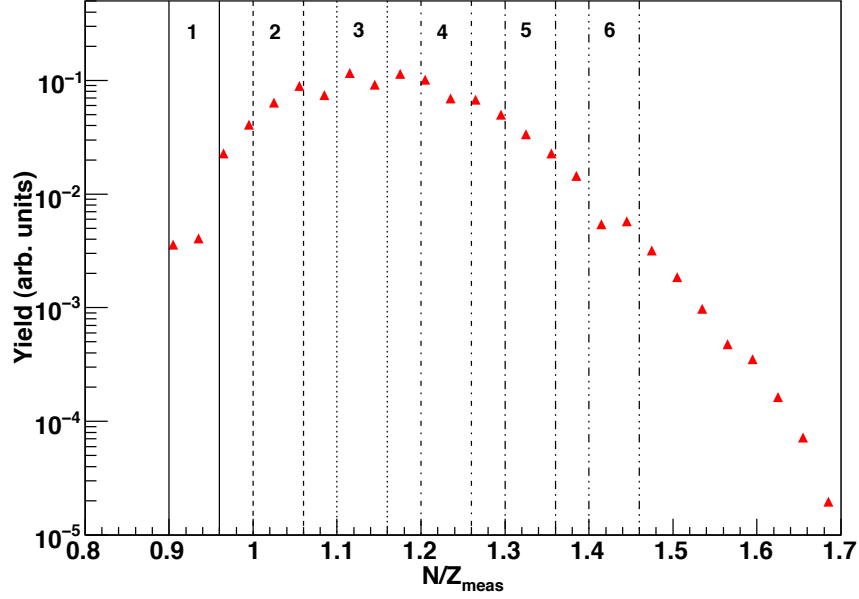
FIG. 32. N/Z_{meas} distribution of the combined reaction systems. Six bins were placed on the N/Z_{QP}: 0.9–0.96 (bin 1), 1.0–1.06 (bin 2),1.1–1.16 (bin 3), 1.2–1.26 (bin 4), 1.3–1.36 (bin 5), and 1.4–1.46 (bin 6). (color online)

relation

$$T_{app} = B/ln(aR_{app}) \tag{5.4}$$

where B is a function of the ground state binding energies, R_{app} is the observed apparent yield ratio, and a is a function of the ground state particle spins of the chosen isotopes. These terms are further explained in Eq. 1.6 though it is important to remember that the binding energy term should be large compared to the source temperature. This thermometer employs the relative production of four isotopes produced in the system [36]. The T_{HeLi} thermometer is shown in Fig. 33 for the ^{86}Kr+^{64}Ni system. This thermometer employs the yield ratios of ^{3,4}He and ^{6,7}Li.

Overlaid with the experimental data in the top panel of Fig. 33 are data from
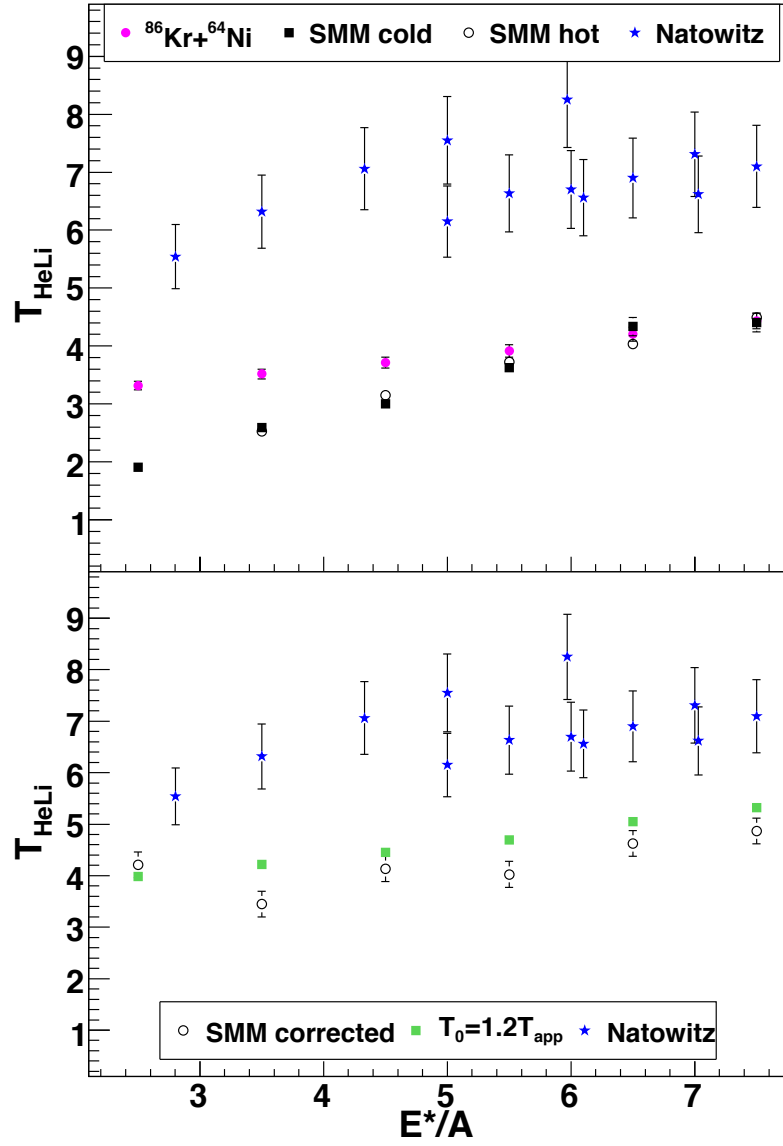
FIG. 33. Top: Temperatures derived from the double isotope ratio method for the ^{86}Kr+^{64}Ni system using $^{3}He/^{4}$He / $^{6}Li/^{7}$Li (closed circles). Temperatures compiled by Natowitz *et al.* [28] from similarly sized systems are also shown (stars). SMM hot and cold temperatures are overlaid (closed squares and open circles respectively). Bottom: Experimental data corrected for secondary decay with SMM (open circles) and with a 20 percent factor (squares). Natowitz compilation is also plotted for reference (stars). (color online)

the published compilation of Natowitz *et al.* [28] for sources with A=60-100. The caloric curve obtained from this data is clearly not in agreement with the compilation caloric curve. In a study by Wada *et al.* [3], a discrepancy similar to what is seen here between the data and other published works was attributed to secondary decay effects on the yield ratios. The DIT-SMM [79, 80] simulation codes were run to estimate the secondary decay effects on the experimentally derived temperature.

The Deep Inelastic Transfer (DIT) model was used to prepare excited quasi-projectiles from peripheral to mid-peripheral nuclear interactions. The statistical multifragmentation model (SMM) [80] was used to decay the excited projectiles from DIT. This model assumes a statistical break up at ρ/ρ_0=1/3 or 1/6. However in the most recent version, it accounts for the whole range of break up mechanisms from fission to vaporization. SMM provides access to the fragments produced in the initial break-up partition as well as the final, cold fragments. Thus, secondary decay effects may be studied by comparing the fragment production from the hot, initial partition to the production in the final, cold products.

The T_{HeLi} was obtained from both the hot and cold fragments obtained from the DIT-SMM simulation of the ^{86}Kr+^{64}Ni system with a freeze out density of ρ/ρ_0=1/6. The DIT-SMM simulated hot and cold caloric curves are plotted with the experimental and Natowitz curves in the top panel of Fig. 33. DIT-SMM does not show any difference between the caloric curve obtained from the ^{86}Kr+^{64}Ni and the ^{78}Kr+^{58}Ni systems for either the hot or the cold fragments. Hence, the difference between the hot and cold caloric curves for the ^{78}Kr+^{58}Ni system was used to estimate the secondary decay correction for the experimental data. The SMM corrected caloric curve as well as a T_0=1.2T_{app} [47] corrected curve are plotted with the Natowitz compilation in the bottom panel of Fig. 33. These secondary decay corrections do not overlay the experimental T_{HeLi} obtained in this data with the published caloric curves of similar

nuclei.

A similar result was found in the work of Wada *et al* [3]. In that work, fragment isotopic temperatures from neither the simultaneous nor sequential decay codes were able to reproduce the input model temperatures. The authors concluded that the mechanism of intermediate mass fragment production is not adequately understood. Thus, the interpretation of this thermometer is not straightforward.

For this data, the correction factors provided by SMM do not change with reacting system and thus only affect the absolute magnitude of the temperature obtained. Accordingly, the experimental data, uncorrected for secondary decay, will be used to study the caloric curve dependence on the N/Z of the fragmenting source. Plotted in Fig. 34 are T_{HeLi} caloric curves constructed from N/Z_{meas} bins 2–5. Comparing across N/Z_{meas} bins, this thermometer does not exhibit a statistically significant change with source N/Z. From Fig. 34, it appears that the data cut in this way does not have the statistics to investigate the N/Z dependence of this observable. To increase statistics, the complete isotopic reconstruction constraint was removed and the most neutron-rich and most neutron-poor reaction systems compared.

The ^{86}Kr+^{64}Ni and ^{78}Kr+^{58}Ni system caloric curves obtained using T_{HeLi} are plotted in Fig. 35. At some excitation energies, it appears that a statistically significant difference may be occuring between the two systems. The thermometer shows a higher temperature for the less neutron-rich source. This trend with source N/Z is opposite to what has been theoretically predicted [14, 15]. To test if this dependence on N/Z is an artifact of the isotopes chosen for the thermometer, other isotope ratios were investigated.

There are many combinations of isotopes that have been and can be used for double isotope thermometers. In general, the binding energy term of the ratios must be large in comparison to the temperature to be studied [47]. The effect of the iso-
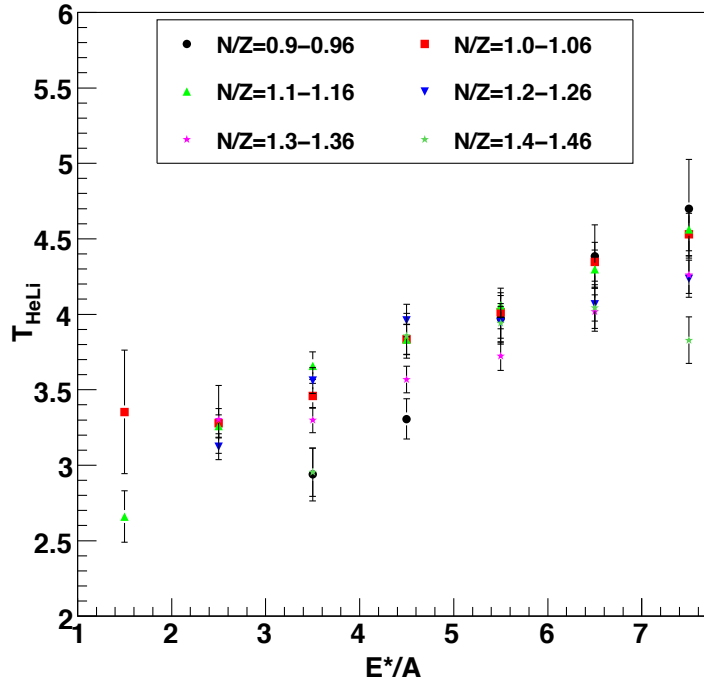
FIG. 34. T_{HeLi} temperatures obtained from source N/Z_{meas} bins. (color online)

topes chosen for the thermometer was investigated by employing a range of isotopic thermometers (see Eqs. 5.5). The caloric curves for each of these four thermometers are plotted in Fig. 36 for the ^{86}Kr+^{64}Ni and ^{78}Kr+^{58}Ni systems. The top two panels employ Z=1–3 fragments. These two thermometers provide a higher temperature for the less-neutron rich system. An opposite trend with N/Z is seen in the bottom two thermometers. These thermometers employ isotopes of Li and C and indicate a higher temperature for the more neutron-rich system. Additionally, the Li-C thermometer predicts a larger difference in temperature with respect to source N/Z than is predicted by the C-C thermometer. From this figure, it can be seen that the magnitude as well as the sign of the difference between the two systems is dependent on the
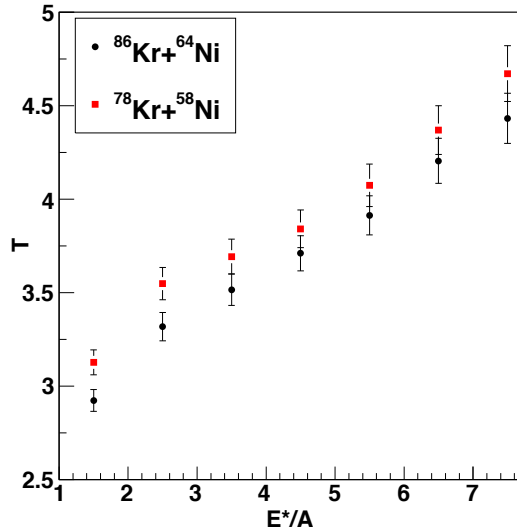
FIG. 35. T_{HeLi} temperatures measured between the most neutron-rich and most neutron-poor reaction systems (^{86}Kr+^{64}Ni and ^{78}Kr+^{58}Ni). (color online)

isotopes chosen for the thermometer.

$$
\begin{aligned}
\mathrm{T}_{HeLi} &= 13.3/\ln\left(2.2\left(Y_{6Li}/Y_{7Li}\right)/\left(Y_{3He}/Y_{4He}\right)\right) \\
\mathrm{T}_{HeDT} &= 14.3/\ln\left(1.6\left(Y_{2H}/Y_{3H}\right)/\left(Y_{3He}/Y_{4He}\right)\right) \\
\mathrm{T}_{LiC} &= 11.5/\ln\left(5.9\left(Y_{6Li}/Y_{7Li}\right)/\left(Y_{11C}/Y_{12C}\right)\right) \\
\mathrm{T}_{CC} &= 13.8/\ln\left(7.9\left(Y_{12C}/Y_{13C}\right)/\left(Y_{11C}/Y_{12C}\right)\right)
\end{aligned}
\tag{5.5}
$$

The N<Z isotopes have been shown [71] to be more dependent than the N≥Z isotopes on the N/Z of the source. However, these N<Z isotopes are necessary to obtain binding energy terms large relative to the system temperature. The caloric curves from Fig. 36 are re-plotted in Fig. 37 as a function of the source N/Z. This figure indicates that the less neutron rich ^{78}Kr+^{58}Ni system yields consistent tem-
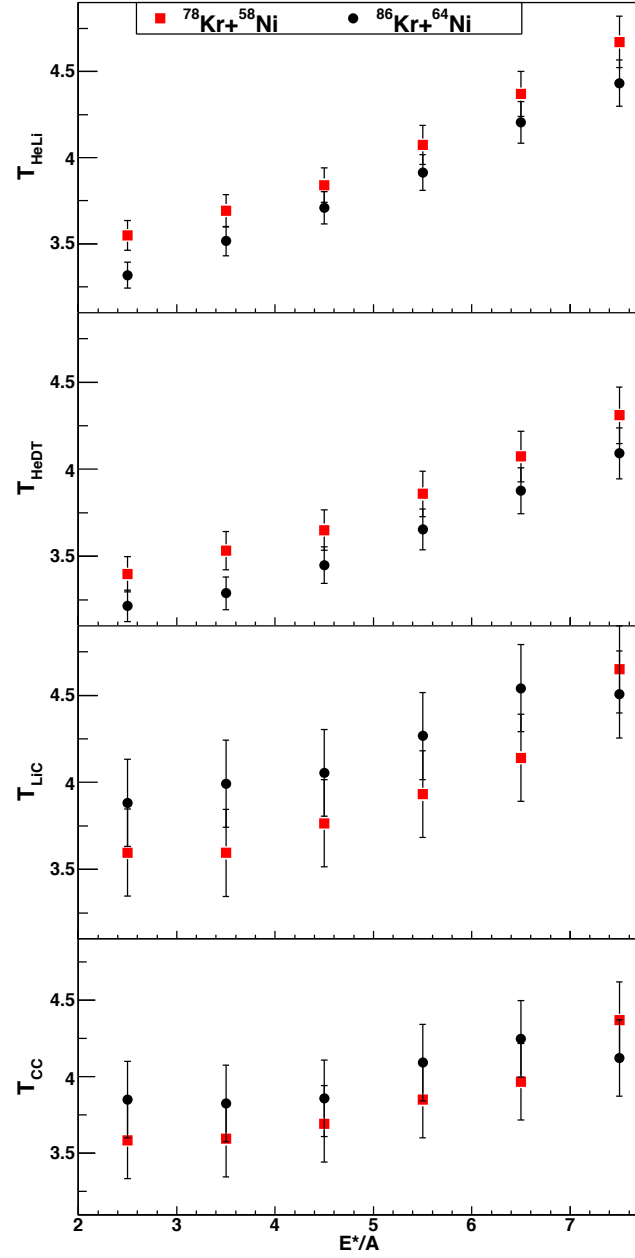
FIG. 36. T_{HeLi}, T_{HeDT}, T_{LiC}, and T_{CC} temperatures (Eq. 5.5) measured between the most neutron-rich and most neutron-poor reaction systems (^{86}Kr+^{64}Ni and ^{78}Kr+^{58}Ni). (color online)
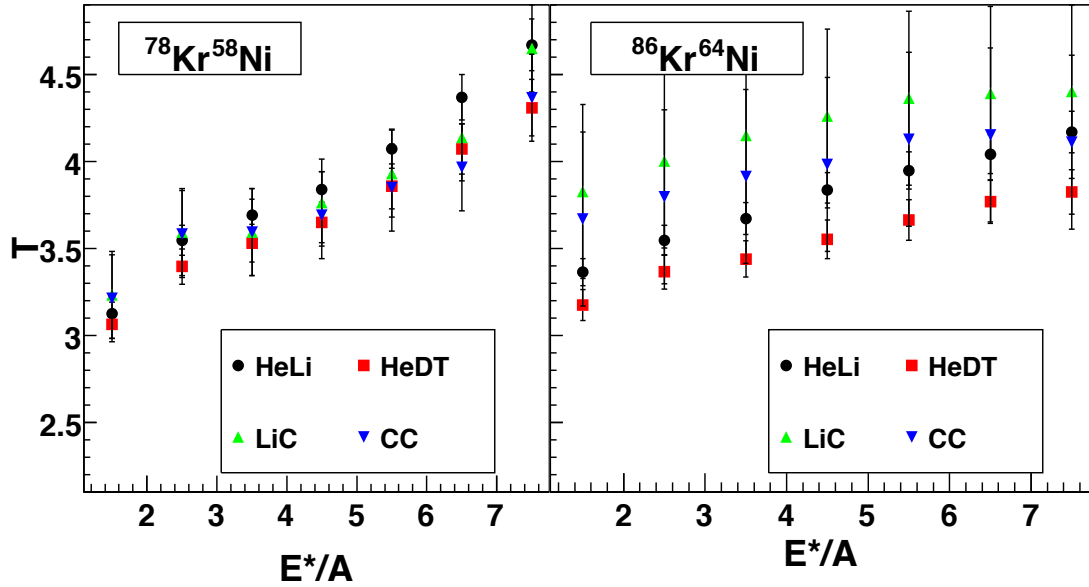
FIG. 37. T_{HeLi}, T_{HeDT}, T_{LiC}, and T_{CC} temperatures from Fig. 36 plotted as a function of the reaction systems (^{86}Kr+^{64}Ni and ^{78}Kr+^{58}Ni). (color online)

peratures regardless of the isotopes chosen for the thermometer. In contrast, the more neutron rich ^{86}Kr+^{64}Ni system shows a larger difference in temperature as a function of the isotopes used for the thermometer. In addition, the ^{86}Kr+^{64}Ni system exhibits a flatter trend of increasing temperature as a function of excitation energy as compared to the ^{78}Kr+^{58}Ni system. In the previous figure (Fig. 36), the T_{HeLi} and T_{HeDT} thermometers indicated that the less neutron rich source has a higher temperature. Conversely, the more neutron rich thermometer was shown to have a higher temperature in the T_{LiC} and T_{CC} thermometers. This change in dependence on source N/Z may result from the sensitivity of the N<Z isotopes to the source N/Z.

As seen in Fig. 33, even after estimating secondary decay corrections, the observed temperature obtained from the double isotope ratios are noticeably lower than

expected for this size of source. This could be a product of sequential decay [81]. If the fragments are not emitted simultaneously but rather sequentially, the temperatures obtained would be affected. The He based thermometers have been shown in the Expanding Emitting Source model [71, 81] to have a strong dependance on the time at which the particle is emitted. Higher Z, such as carbon, based thermometers have been proposed to be less dependent on the time scale of fragment emission and to sample the system very late in the emission process [71].

The effect of sequential decay on the double isotope thermometers has been studied through relating the fragment velocity to time of emission. Fragment velocity cuts in the source frame were made on the four double isotope thermometers studied (Eq. 5.5). The observed temperatures as a function of fragment velocities are plotted in the top panels of Fig. 38 for the ^{78}Kr+^{58}Ni and ^{86}Kr+^{64}Ni systems.

In the top panels of Fig. 38, the measured temperature exhibits an increase with fragment velocity. This increase is seen in the He based thermometers for both the ^{86}Kr+^{64}Ni and ^{78}Kr+^{58}Ni systems. For the T$_{HeLi}$ and T$_{HeDT}$ thermometers, the ^{78}Kr+^{58}Ni system has a slightly higher temperature across the velocity bins. This is the same behavior as is observed for the velocity integrated temperature. In addition, the small difference with respect to source N/Z increases with the fragment velocity. In the C based thermometers, the neutron-poor system shows the same steadily increasing trend in temperature that is seen in the He thermometers. However, only at low velocity does the ^{86}Kr+^{64}Ni system have a higher temperature relative to the ^{78}Kr+^{58}Ni system as was observed in the velocity integrated thermometer. In the ^{86}Kr+^{64}Ni system this thermometer not only falls below the ^{78}Kr+^{58}Ni system, but also decreases in absolute value.

To investigate this decrease in temperature as a function of fragment velocity, the individual isotopic ratios have been plotted in the middle (^{86}Kr+^{64}Ni) and bottom
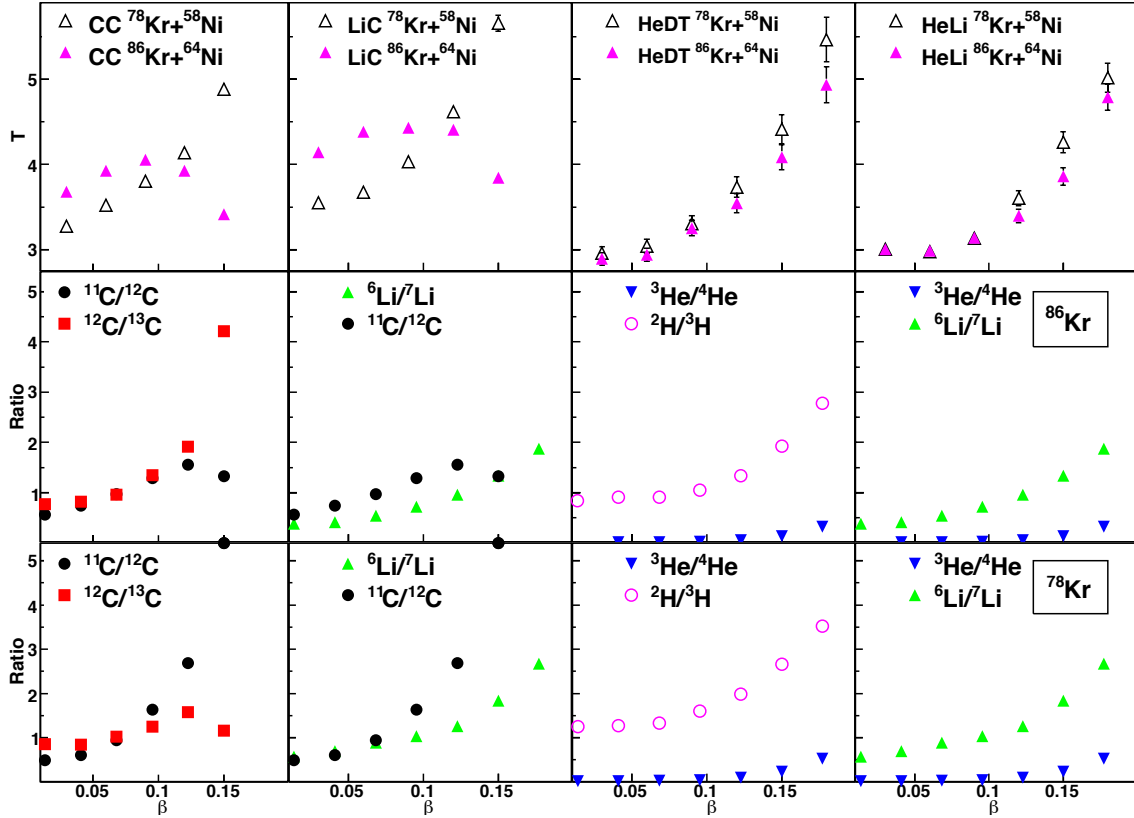
FIG. 38. Top: Temperature versus fragment velocity in the frame of the source for the ^{78}Kr+^{58}Ni and ^{86}Kr+^{64}Ni reaction systems. Middle: Isotope ratios for the ^{86}Kr+^{64}Ni system. Bottom: Isotope ratios for the ^{78}Kr+^{58}Ni system. (color online)

(^{78}Kr+^{58}Ni) panels of this figure. The He based thermometers show a smoothly increasing trend in the component isotope ratios as a function of fragment velocity. This same smooth trend can be seen in the ^{6,7}Li and ^{12,13}C isotopes used in the C thermometers. The decrease in temperature seen in the ^{86}Kr+^{64}Ni system is caused by the decrease in the ^{11,12}C ratio at high velocity. This change in the ^{11,12}C ratio at high velocity does not occur in the ^{78}Kr+^{58}Ni system. As mentioned earlier, the N<Z isotopes have been shown [71] to be more dependent than the N≥Z isotopes on
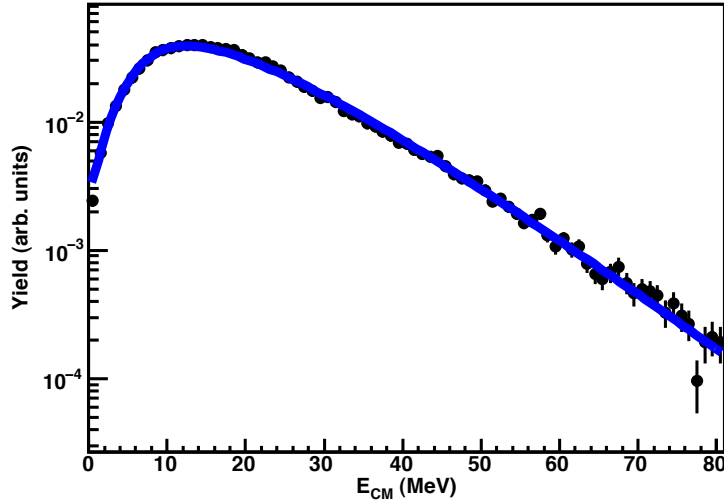
FIG. 39. Center of mass (projectile frame) energy distribution for Li particles. The line is the Eq. 5.6 fit to the distribution. (color online)

the N/Z of the source. The evolution of the ^{12,13}C and ^{11,12}C ratios plotted in Fig. 38 are consistent with this.

The double isotope thermometer is a chemical thermometer and thus should not depend on fragment motion in any way. This means that while the isotope ratios are subject to errors due to feeding from secondary decay and fragment time of emission, the temperature should not be intrinsically affected by Coulomb driven expansion or collective motion of the source. However, the yields of isotopes along the beam axis are known to be asymmetric. Thus, the data cuts used to define the source can alter the measured isotope ratios. This source dependence can reduce the impact of comparisons between reaction mechanisms and data sets.

In this data, a second thermometer has been derived from moving source fitting. This fitting has been widely used as a method of defining the probability of a fragment resulting from a given source such as pre-equillibrium, quasi-projectile, quasi-target,

etc. However, because cuts have been imposed to define the quasi-projectile source in this data, the fitting is conducted assuming a single well defined source with the aim of measuring the source temperature. Moving source fitting obtains a value for temperature from the energy distribution of particles (Fig. 39). This distribution has been parameterized by Moretto [82] as

$$P(x)dx \propto \left\{ (2x-p)exp\left(-\frac{x}{T}\right) erfc\left(\frac{p-2x}{2\sqrt{pT}}\right) + 2\sqrt{\frac{pT}{\pi}}exp\left(-\frac{p^2+4x^2}{4pT}\right) \right\} dx \tag{5.6}$$

where P(x) is the probability of a given energy value, x is the Coulomb barrier corrected fragment energy in the source frame, p is an amplification parameter, and T is the temperature. The x variable is parameterized as x = E-k*CB. In this parameterization, CB is the touching spheres Coulomb Barrier calculated with r_0 = 1.9 [5]. The parameter k is a fitting parameter representing the fraction of the barrier required to fit the experimental distribution. An example fit of this function to Li particles is plotted in Fig. 39. The fit reproduces this Li data well with parameter values of p=1.3, T=9.5 MeV, and Coulomb fraction k = ∼0.8.

The amplification parameter p corresponds to fluctuations in the relative strength of the surface and Coulomb potential energy contributions. As p becomes large, the energy distribution becomes Gaussian in shape. Conversely, small values of p correspond to Maxwellian distributions of the energy spectra. The evolution of p with respect to particle type and excitation energy is shown in Fig. 40 for the ^{78}Kr+^{58}Ni and ^{86}Kr+^{64}Ni systems. The magnitude of this parameter clearly increases with Z as well as with excitation energy. This parameter yields similar values for both sources.

A series of temperatures were obtained by fitting the slopes of Z=3-7 elements. This collection of caloric curves are plotted in the left panels of Fig. 41. The errors plotted in this figure are statistical. However, a reasonable estimate of the systematic
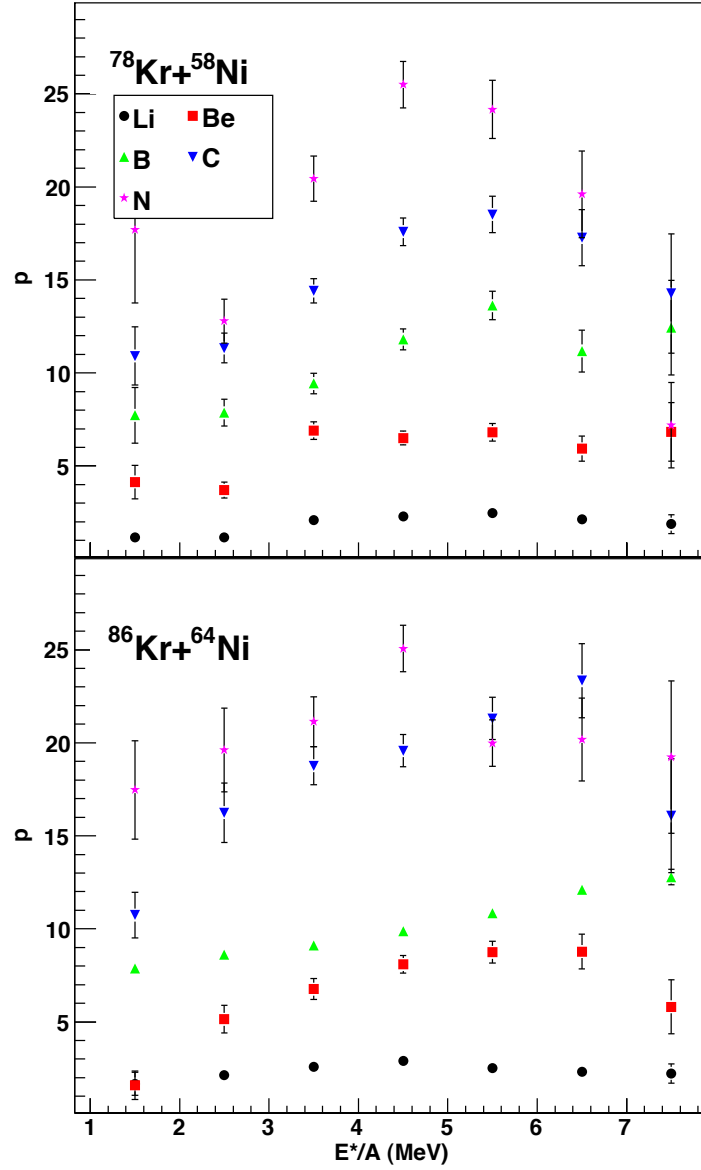
FIG. 40. The moving source fitting parameter p (Eq. 5.6) as a function of particle type and excitation energy of the source. Top) ^{78}Kr+^{58}Ni Bottom) ^{86}Kr+^{64}Ni. (color online)

error in the measured temperatures is ∼0.5 MeV. The caloric curves plotted in this figure indicate that for Z=4-7, the measured temperatures are within errors of each other across all excitation energies. Additionally, Fig. 41 indicates that the temperature difference between the ^{78}Kr+^{58}Ni and ^{86}Kr+^{64}Ni systems is negligible across all fragment Z.

In addition to extracting temperature from moving source fits, a study by Viola *et al.* [5] of light ion induced reactions demonstrated that the density of the system may be derived from moving source fitting. The Coulomb repulsion (k∗CB) was calculated between the fragment of interest and the residue. The residue was assumed to be a single fragment defined as the sum of all uncollected charge of the composite system. This assumption implies that the fragment of interest is the last fragment emitted. Thus, the source size is minimized and detection of the residue is not required. The assumption is useful because, in light-ion induced reactions, it is likely that a large residue fragment would not be detected.

In this thesis data of reconstructed quasi-projectiles there are no large missing portions of the source. The residue in this case is defined as all fragments detected in the event other than the fragment of interest. This assumes that the fragment in question is the first fragment emitted from the source. The Coulomb repulsion (k∗CB) was approximated by fitting with Eq. 5.6 where the factor k is a fitting variable corresponding to the fraction of the Coulomb barrier observed for a given particle within an E*/A bin.

Example energy spectra in the fragmenting source frame are plotted in Fig. 42 for carbon fragments. The distributions have been normalized to provide visual separation. The peaks of these spectra evolve with the E*/A of the source. This is most visible in the three lowest E*/A distributions. The Coulomb barrier is strongly correlated to the position of the distribution peak. Thus, the evolution in peak position
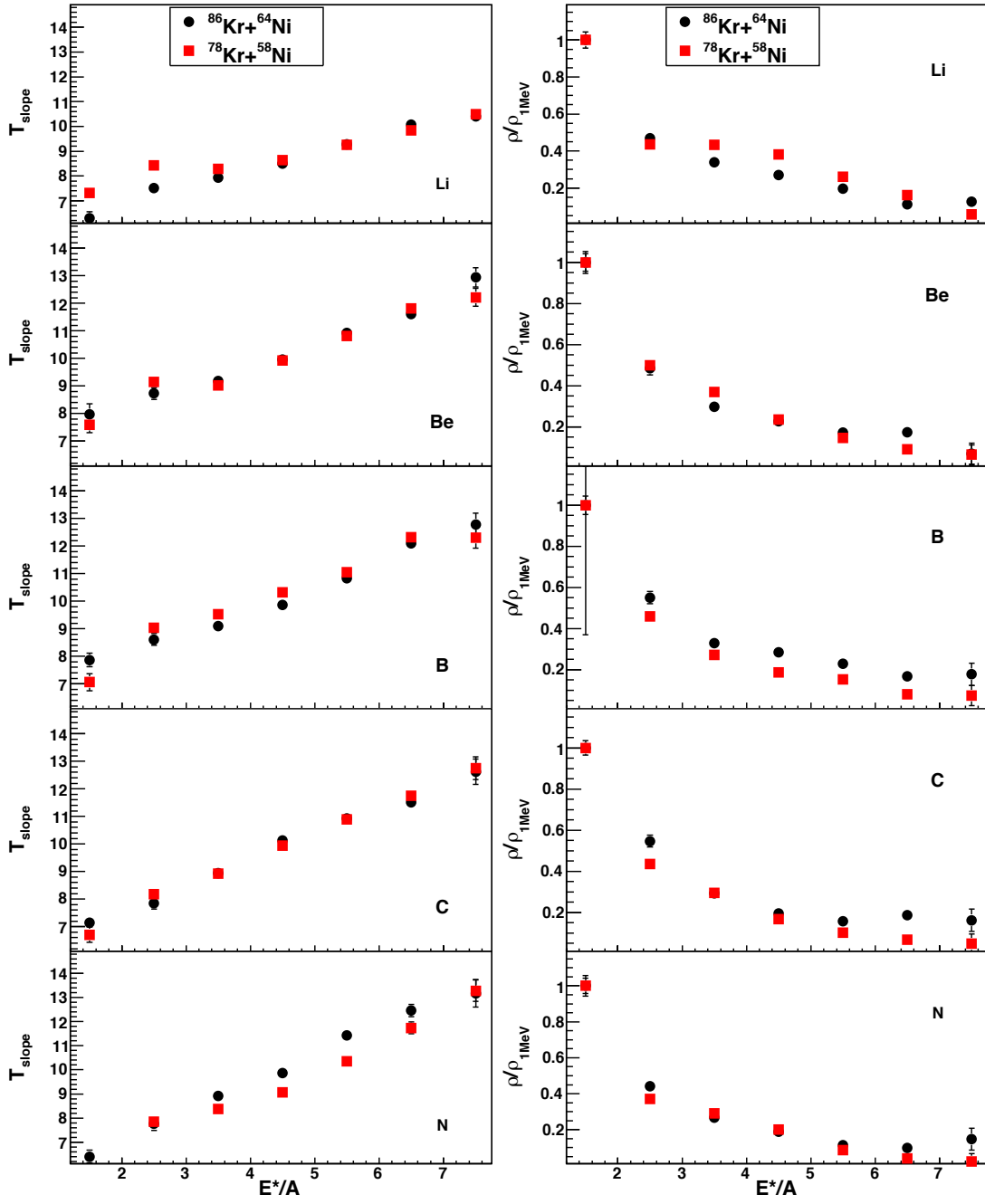
FIG. 41. Left: T_{slope} as a function of E^*/A of the source event for Z=3-7 elements. Right: The associated densities obtained from the fitting procedure and normalized to the lowest excitation energy bin. (color online)
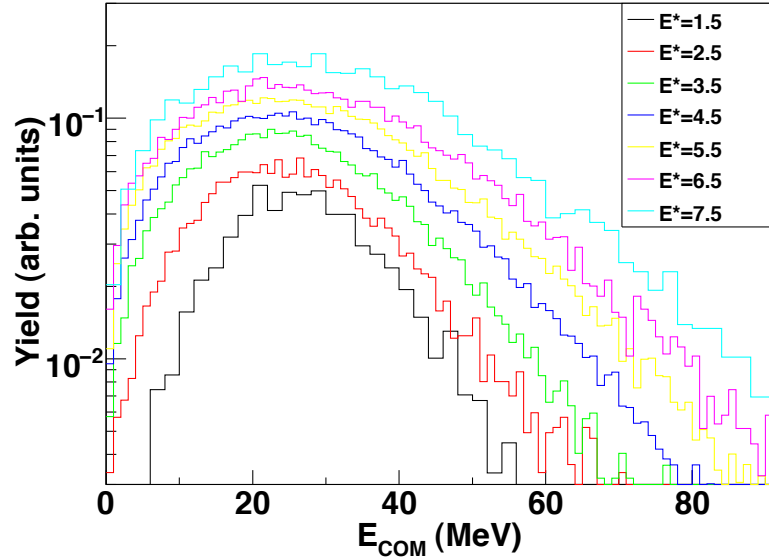
FIG. 42. Center of mass energy distributions for Z=6 cut on the excitation energy of the source. The lowest curve is 1.5 MeV and the curves are in 1 MeV E^*/A increments with the highest curve at 7.5 MeV. (color online)

seen in this figure is correlated to a decrease in source density.

The source density was derived by taking the cube of k obtained from the moving source fitting and normalizing the value obtained from each E^*/A bin to the value obtained for the lowest E^*/A bin. Though the density is designated as ρ/ρ_{1MeV}, it should be noted that it is likely that the density of a nucleus at 1 MeV of E^*/A is very near or equal to normal nuclear density. The density, as obtained from the moving source fitting and normalized to the E^*/A=1 MeV/A point is plotted in the right hand panels of Fig. 41 for Z=3–7. The two systems exhibit similar evolution in density across all E^*/A.

The average density as a function of E^*/A was calculated by averaging the density of each system and each element. This average density is plotted in Fig. 43. The calculated average density is clearly falling over the E^*/A = 1.5-7.5 range. The rate
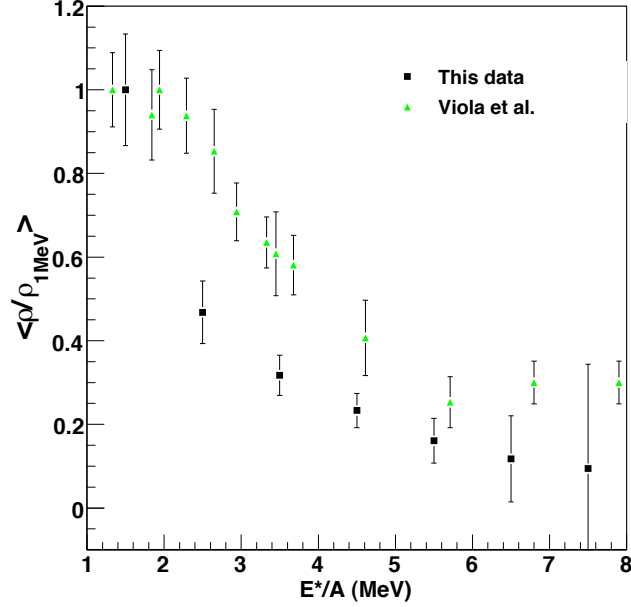
FIG. 43. Density (ρ/ρ_{1MeV}) obtained from averaging the density calculated from moving source fits to Z=3-7 spectra for the ^{78}Kr+^{58}Ni and ^{86}Kr+^{64}Ni systems. The average density is plotted in solid squares. In addition, the solid triangles are experimentally obtained densities from light-ion reactions [83]. (color online)

of decrease is greatest at the low E*/A though the density evolves over the entire excitation energy range.

A similar decrease in density with increasing excitation energy has been sen in previous data [83, 84]. Plotted with the average density from this data in Fig. 43, is the data of Viola et al [83] from light-ion reactions. The density from these two data sets changes at different rates for low E*/A. This difference results from the assumption that the fragment of interest is either emitted first (this data) or emitted last (ISiS data [83]). The time of fragment emission assumption is most important at low E*/A. Thus, these data sets provide upper and lower bounds for the change in density as a function of E*/A.

The temperatures obtained through moving source fits are well accepted to be relatively high for the reaction energy of this thesis [42]. Some years ago, it was proposed that this thermometer could reflect not only the thermal energy of the source, but also the fragment internal Fermi momentum. According to Bauer's hypothesis, this behavior is of increasing importance until a limiting value is reached around A=12 [42]. In this theory, the effect of the Fermi momentum is density dependent and would induce plateau like behavior in the caloric curves presented in Fig. 41.

The Fermi momentum explains the high value of T obtained for $E^*/A \sim$3-7 MeV. However, it does not explain the high values of temperature observed at lower excitation energy. These low E^*/A points could be exhibiting residual collective motion along the beam axis. Moreover, the collective behavior along the beam axis could be contributing across all of the E^*/A bins.

Residual collectivity along the beam axis has been addressed explicitly for the third thermometer which is derived from momentum fluctuations. As described in the previous chapter, the the temperature of a source may be measured through observing the momentum fluctuations of the fragments for a class of events. In this case, the fragments have been grouped into excitation energy bins. The momentum fluctuations show a strong mass dependence as well as residual collective behavior along the beam axis. The collective behavior has been removed by studying the momentum fluctuations in the transverse direction. The Fermi momentum contribution to the mass dependence of this thermometer is not present for protons. Consequently, the proton momentum fluctuations have been measured in the transverse direction to derive the source temperature.

The caloric curves obtained from the transverse momentum fluctuation of protons from the ^{78}Kr+^{58}Ni and ^{86}Kr+^{64}Ni reaction systems are plotted in Fig. 44. This thermometer indicates that the systems are at temperatures well within systematic
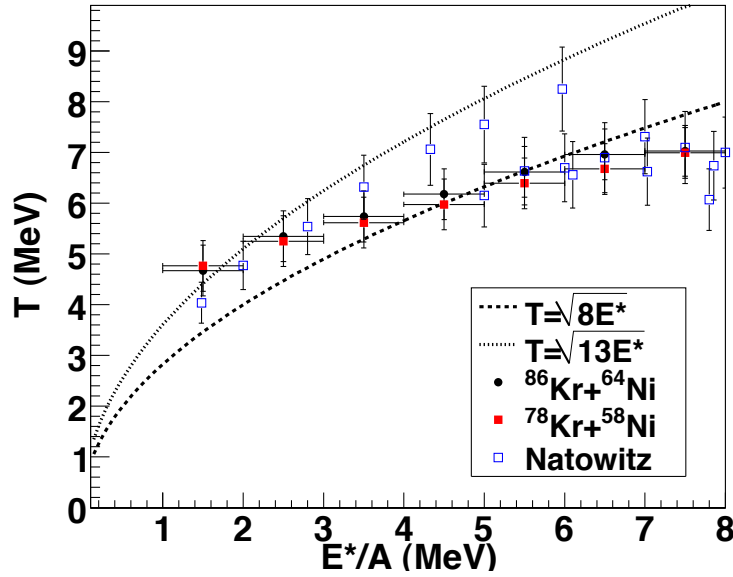
FIG. 44. Q_{xy} temperature obtained from protons as a function of E^*/A of the source event for ^{78}Kr+^{58}Ni and ^{86}Kr+^{64}Ni. For reference the caloric curve for A=60-100 from the Natowitz compilation [28] as well as two Fermi Gas ($T = \sqrt{aE^*/A}$ with a = 8, 13) curves are plotted. (color online)

errors of each other. Secondary decay should not affect this result because it is random in direction and would thus cancel out. Furthermore, movement of the nuclear system from evaporation to multi-fragmentation is theoretically unimportant in this thermometer due to random fragment emission directions.

To conclude, this chapter has investigated the effect of the source N/Z ratio on the measured temperatures. Three thermometers were investigated: the double isotope thermometer, the slope thermometer from moving source fits, and the momentum fluctuation thermometer.

The double isotope thermometer showed a strong dependence on the N/Z of the source. This dependence was introduced through the N<Z isotopes. The temper-

atures measured were relatively low compared to other thermometers and reference caloric curves. These low values are partially due to secondary decay corrections which do not change any source N/Z trends but only alter the absolute value of temperature by $\sim$20%. In addition, the temperatures obtained with this thermometer are affected by the assumption of simultaneous multi-fragmentation versus sequential binary decay of the excited source.

The slope thermometer produced consistent temperatures across the Z=4-7 intermediate mass fragments. The temperatures are attributed here to a combination of thermal energy, Fermi momentum of nucleons, and collective motion of the fragments along the beam axis. The slope thermometer did not show any statistically significant dependence of the measured temperature on the source neutron to proton ratio.

Finally, the momentum fluctuation thermometer has been investigated. This thermometer, as shown in the previous chapter, exhibits a small contamination from collective motion of the fragments along the beam axis. Thus, in this chapter the transverse direction is explored to avoid any contamination from collective motion in the beam direction. In addition, this study focused on proton momentum fluctuations since heavier particles may contain contributions from Fermi momentum. The proton transverse momentum fluctuations were used to investigate the temperature dependence on the source N/Z. Any source N/Z dependence of the measured temperature has been shown here to be well within errors for the ^{78}Kr+^{58}Ni and ^{86}Kr+^{64}Ni systems.

CHAPTER VI

SCALING

Scaling studies are a very useful experimental tool for comparing fragmenting sources. This tool has strong theoretical ties to the nuclear equation of state that extend beyond the nuclear phase transition debate. For example, both power law and isoscaling studies exhibit a strong sensitivity to the asymmetric portion of the nuclear equation of state. Additionally, isoscaling studies provide a direct experimental link to the symmetry energy coefficient C_{sym}.

To extract power law scaling, both charge and mass distributions can be examined. Historically, there is little consensus about the region in Z or A that should be fit to extract an experimental value of the slope parameter τ [1, 5, 8, 9]. However, there are two fragment size factors to bear in mind. At the low end of a charge or mass distribution, the number of bound isotopes varies widely with Z leading to non-statistical behavior [1, 85]. Additionally, the largest fragment produced in an event has been associated with a remaining liquid drop and omitting this particle has been shown to improve the power law behavior of the distribution [34].

With the largest fragment removed, the effect of the chosen charge distribution fitting region on the evolution of the τ parameter is shown in Fig. 45 for the ^{86}Kr+^{64}Ni system. In this plot (Fig. 45), the charge distributions were fitted with

$$Yield = CZ^{-\tau} \tag{6.1}$$

where C is a free fitting parameter, Z is the charge of the fragment, and τ is the power law exponent of Fisher scaling.

From Fig. 45, it is clear that the fitting region chosen has a significant effect on the magnitude of τ. These fitting regions were selected with source contamination
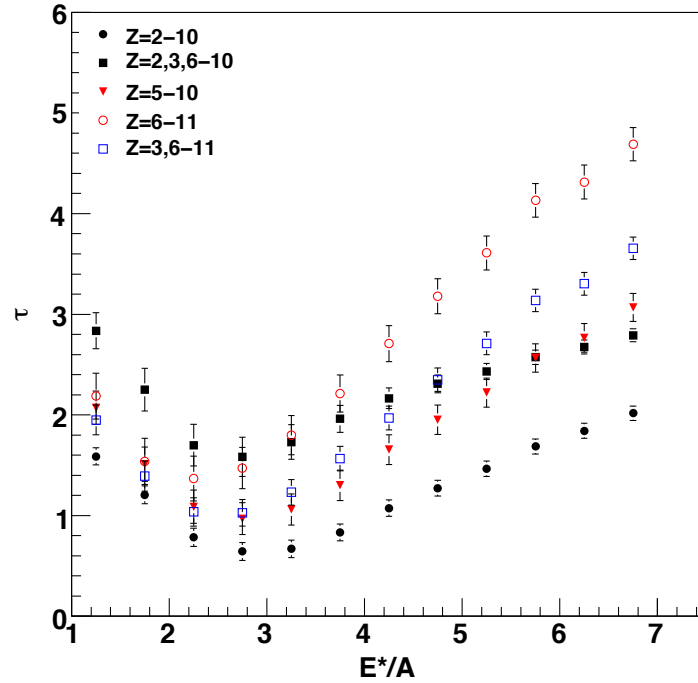
FIG. 45. Comparison of the value and behavior of the τ parameter (Eq. 6.1) as a function of E*/A from fitting various regions of the charge yield distributions. (color online)

and particle yield fluctuations in mind. The fitting regions omit Z=4 because ^{8}Be is unbound which significantly lowers the overall yield of this element. A fitting region with Z=5 omitted was also tested because this element was found to have a lower yield than Z=6. Finally, the Z=1,2 fragments are relatively susceptible to source contamination and have been omitted from the fitting.

The value of τ plotted in Fig. 45 increases at high E*/A as low Z fragments are omitted from the fit. In addition, the value of τ_{min} varies widely with fitting region. In contrast to the widely varying values of τ, the position along the E*/A axis at which the minimum is reached is consistent within these fitting regions with

FIG. 46. Comparison of the value and behavior of the τ parameter (Eq. 6.1) as a function of E*/A from fitting various regions of the mass yield distributions. (color online)

an average value of 2.5–3 MeV/A.

Similar dependance on the fitting region can be observed when mass distributions are fitted with

$$Yield = CA^{-\tau}. \tag{6.2}$$

A selection of mass distribution fitting regions are plotted in Fig. 46. As seen in the charge distributions, the magnitude of τ varies with the fitting region chosen. The A$\leq$10 region was excluded due to the large fluctuations in the number of available isotopes for low Z elements [1, 85]. At low E*/A, the fitting regions yield consistent values of τ except for the A=11-19 fitting region which produced a significantly higher
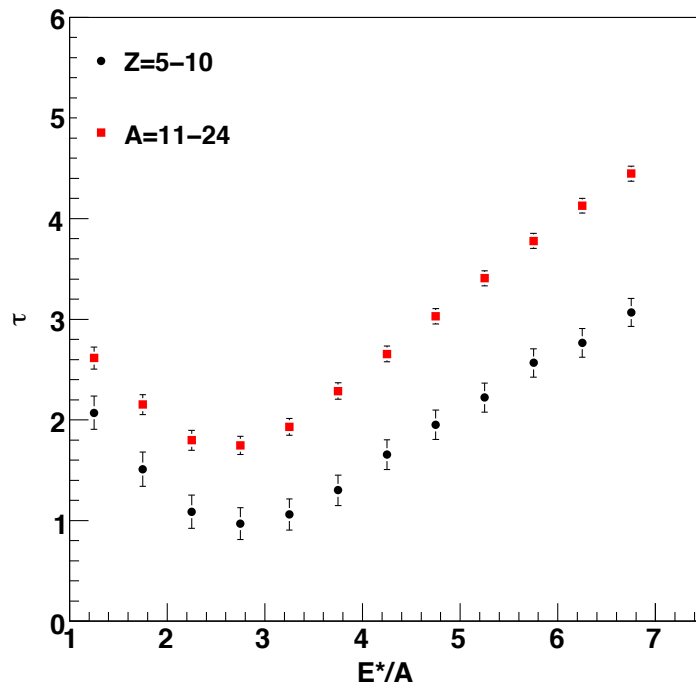
FIG. 47. Comparison of the value and behavior of the τ parameter (Eq. 6.1) as a function of E^*/A from fitting the charge and mass distributions. (color online)

value. The A=11-19 fitting region also provides a higher value of τ_{min} than the other fitting regions. At high energy, all of the fitting regions agree within errors except for the A=13-24 fitting region which diverges to much higher τ values. As seen previously in the charge distribution fitting, the region of E^*/A at which the τ reaches a minimum is fairly consistent within these mass fitting regions.

The fitting regions for both the charge and mass distributions were selected to maximize the width of the fitting region. The A=11–24 and Z=5–10 fitting regions are plotted together in Fig. 47. The position of the τ_{min} along the E^*/A axis is consistent for both mass and charge distributions though the value of τ_{min} is not equivalent. These two fits show a very similar evolution in τ across all E^*/A. The
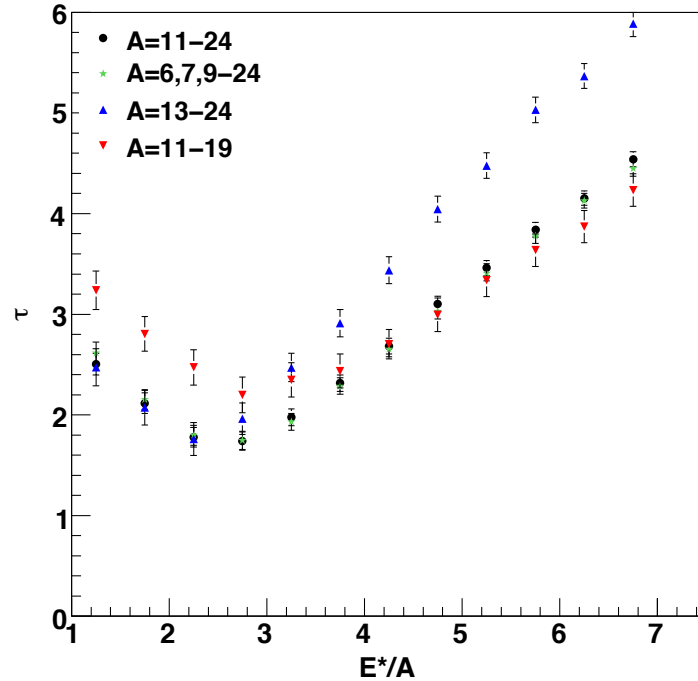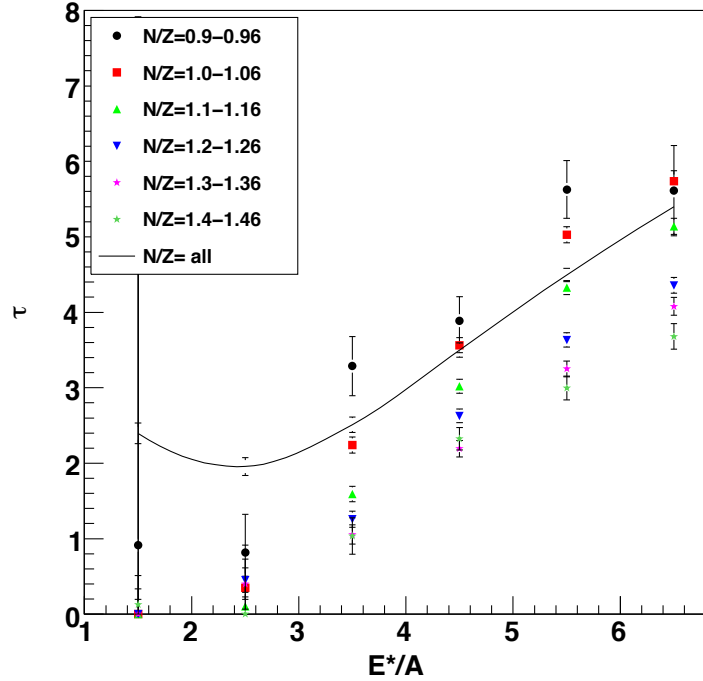
FIG. 48. Comparison of the value and behavior of the τ parameter (Eq. 6.1) as a
function of E^*/A from fitting the mass distributions for A=11–24. The solid
line is the τ obtained by fitting over all N/Z_{QP} bins. (color online)

mass distributions provide a wider fitting region free of obvious structure effects as
well as a theoretically acceptable value of τ_{min}. For these reasons, this scaling study
will focus on mass distributions fitted over the A=11–24 region.

In the previous chapter, the reconstructed quasi-projectiles from all four reaction
systems were divided into bins based on the N/Z_{meas} of the event. Fig. 48 shows the
evolution of τ as a function of E^*/A for each of these bins in N/Z_{meas}. For reference,
the τ points are also plotted for the system as a whole. Though the error bars are
large, the low N/Z_{meas} bins provide higher values of τ than the higher N/Z_{meas} bins
at high E^*/A. All of the N/Z_{meas} bins converge within errors at 2.5 MeV/A.
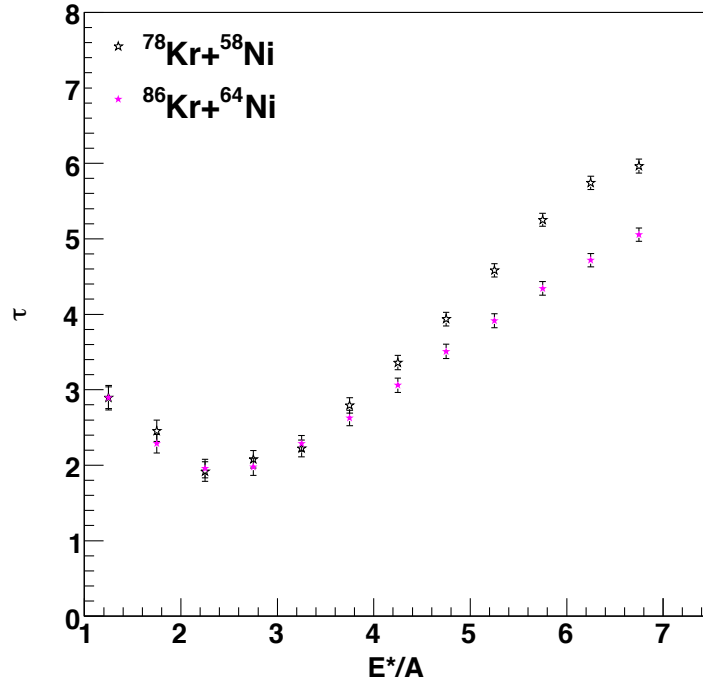
FIG. 49. Evolution of the τ parameter (Eq. 6.2) with respect to system excitation energy for the ^{86}Kr+^{64}Ni and ^{78}Kr+^{58}Ni systems. (color online)

To minimize the error bars, the most neutron-rich and least neutron-rich systems (^{86}Kr+^{64}Ni and ^{78}Kr+^{58}Ni respectively) were also studied. The $\tau(E^*/A)$ from mass distribution fitting can be seen in Fig. 49 for the two reaction systems. It is evident that the position and value of τ_{min} are not changing appreciably in these fits. However, above the τ_{min} at $\sim$3 MeV, ^{78}Kr+^{58}Ni yields larger τ than ^{86}Kr+^{64}Ni does. This difference increases with the E$^*/A$ of the source.

Away from the critical region, the mass distributions must be fitted using a modified Fisher equation

$$Yield = Y_0 A^{-\tau} X^{A^{2/3}} Y^A. \qquad (6.3)$$

incorporating terms for the surface (X$^{A^{2/3}}$) and volume (Y^A). In this equation, Y$_0$,
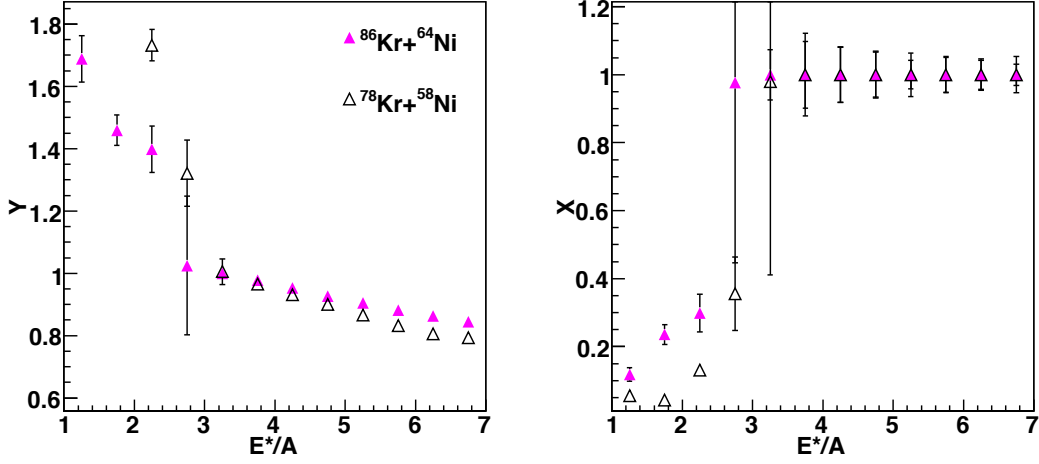
FIG. 50. Evolution of the X and Y parameters (Eq. 6.3) with respect to system excitation energy for the ^{86}Kr+^{64}Ni and ^{78}Kr+^{58}Ni systems. (color online)

X, and Y are fitting parameters [86]. At the critical point theory dictates that both X and Y equal 1 which yields Eq. 6.2. Above the critical point, theory also indicates that X (the surface) must equal 1.

The experimental mass distributions were fitted using Eq. 6.3. The value of τ in this case does not change with respect to E*/A. To obtain τ, the reference bin was chosen by fitting the E*/A bins in the 2-4.5 MeV region with Eq. 6.3. The fitting was carried out with τ required to be within the theoretical limits of 2-3. Additionally, the X,Y parameters were constrained to equal 1. The 3.25 MeV bin was chosen in each system as the bin with the lowest value of τ. The τ parameter was then held constant and the fragment yields fitted for each E*/A bin to obtain the X and Y values. Below the 3.25 MeV bin, the X and Y values were allowed to vary freely. However, at and above 3.25 MeV/A E*/A X was defined as 1.

The evolution of X and Y as a function of E*/A across the A=11–24 mass region for the ^{86}Kr+^{64}Ni and ^{78}Kr+^{58}Ni systems is shown in Fig. 50. The Y parameter

decreases to a lower value for the less neutron-rich source. The less neutron-rich source also exhibits a lower value of X below the 3.25 MeV/A bin. Because X≡1 above the limiting temperature, the deviation of Eq. 6.2 between the ^{86}Kr+^{64}Ni and ^{78}Kr+^{58}Ni systems seen in Fig. 49 for E*/A ≥ 3 MeV/A may be interpreted as reflecting the sensitivity of the volume term to the source N/Z.

The system wide fits with Eq. 6.3 provided τ values of 2.29 (0.12) and 2.21 (0.11) respectively. These minima are well within errors of each other. This insignificant source N/Z dependence of τ appeared inconsistent with the strong particle asymmetry (I) dependance seen by Bonasera *et al.* [4]. To examine the apparent discrepancy, particle scaling was investigated in this data for fragments with A=11-24. For consistency with the work of Bonasera *et al.*, the particle asymmetry is defined as

$$I = N - Z \tag{6.4}$$

where N is the neutron number and Z the proton number of the fragment.

Fig. 51 depicts the particle scaling fitted with Eq. 6.2 as a function of I and the reaction system. The left panels are derived from the ^{78}Kr+^{58}Ni system and the right panels from the ^{86}Kr+^{64}Ni system. The slope of the mass distribution clearly decreases as the asymmetry of the fragments increases. It is clear that the asymmetry (I) of the fragment has a large influence on the scaling parameter obtained from the fit. All fragment asymmetries show an increase in the slope with increased source N/Z. There is also an odd-even effect that necessitates two sets of fitting parameters to adequately describe the data. This odd-even behavior was also observed by Bonasera *et al.* [4] and was attributed to secondary decay through neutron emission.

The change in τ with respect to source N/Z was further investigated by implementing the six N/Z$_{meas}$ bins taken from the four reaction systems. The E*/A averaged τ for each of these bins was extracted and is plotted in Fig. 52. The slight
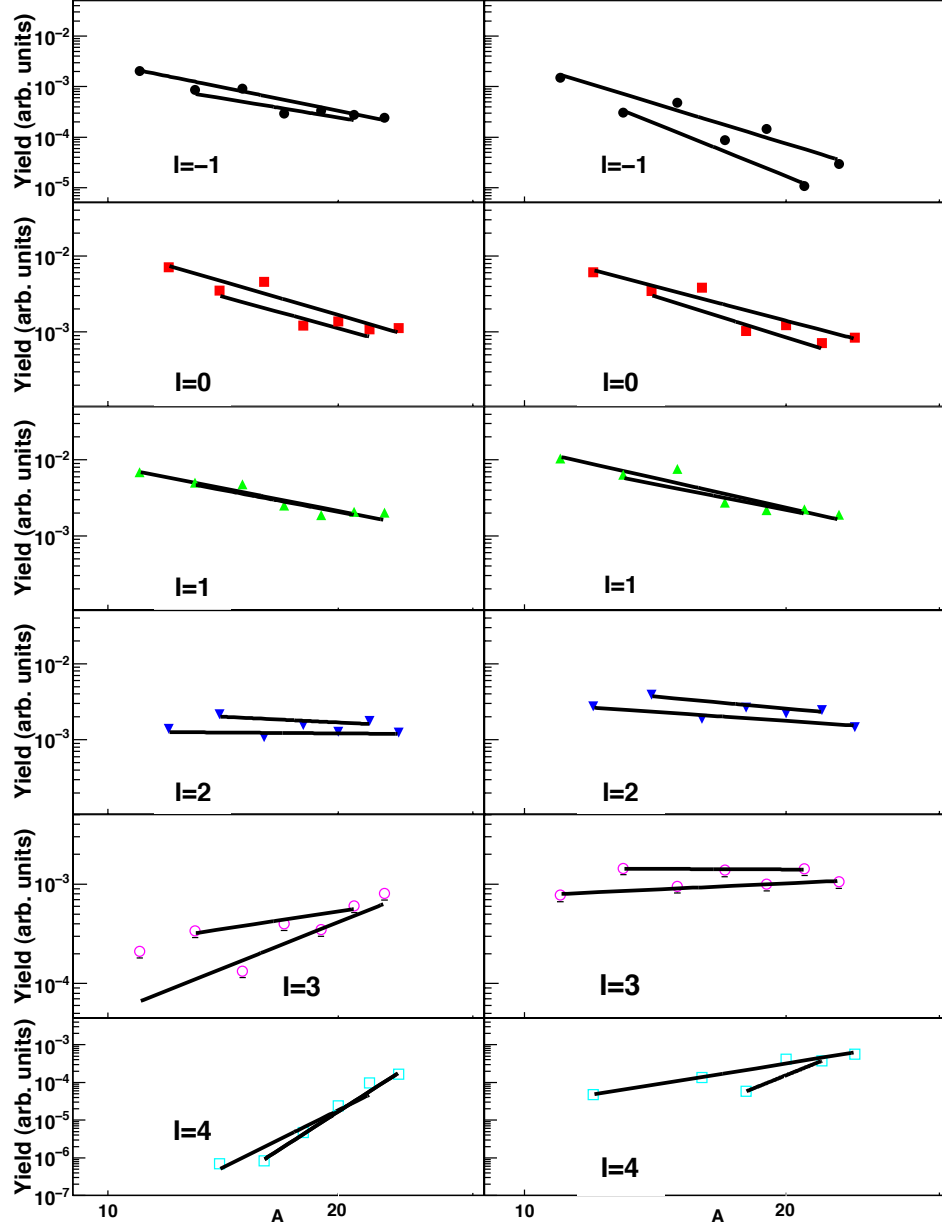
FIG. 51. Evolution of the fragment scaling as a function of system and particle asymmetry for A=11–24. Left) ^{78}Kr+^{58}Ni Right) ^{86}Kr+^{64}Ni (color online)
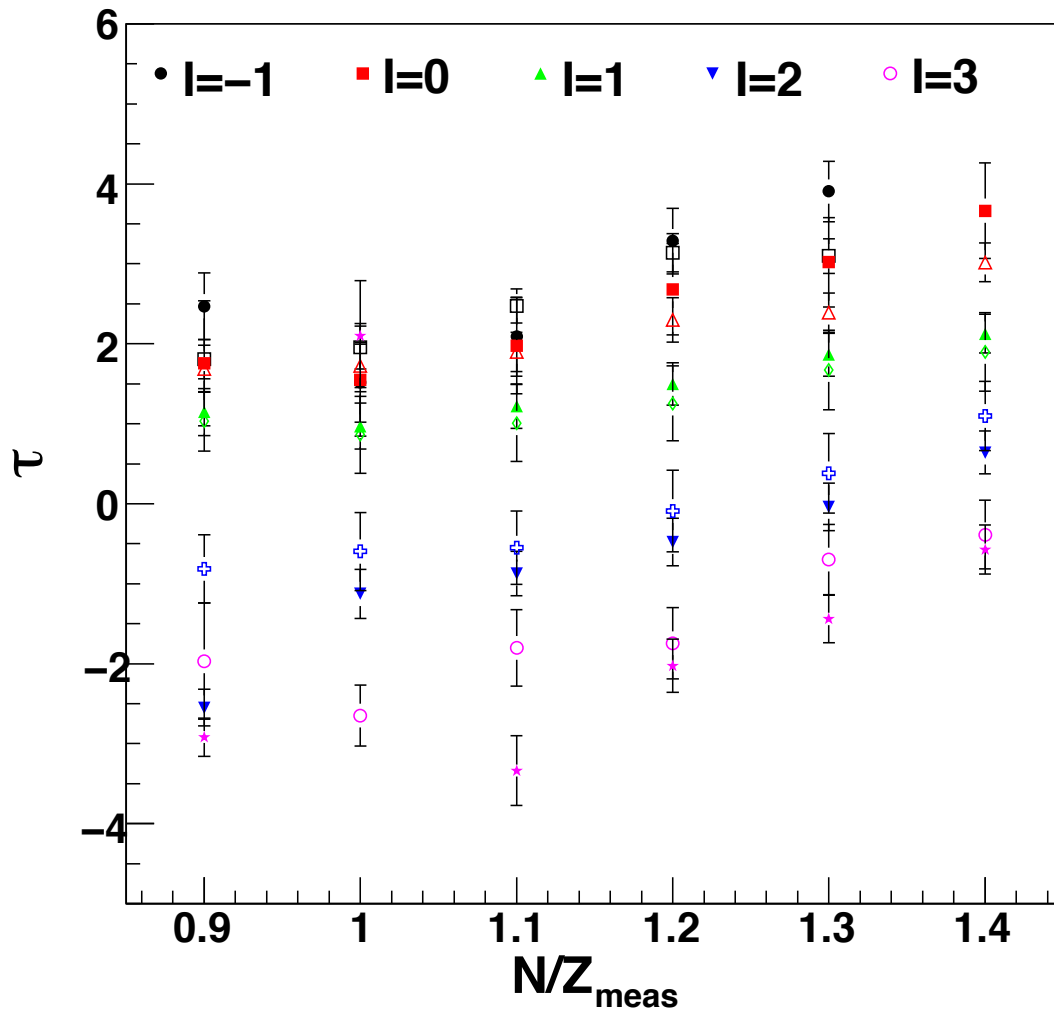
FIG. 52. Evolution of the fragment scaling as a function of system and particle asymmetry for A=11–24. Fragments with even Z are open symbols and fragments with odd Z are closed symbols. Symbol color indicates the I of the fragments. (color online)
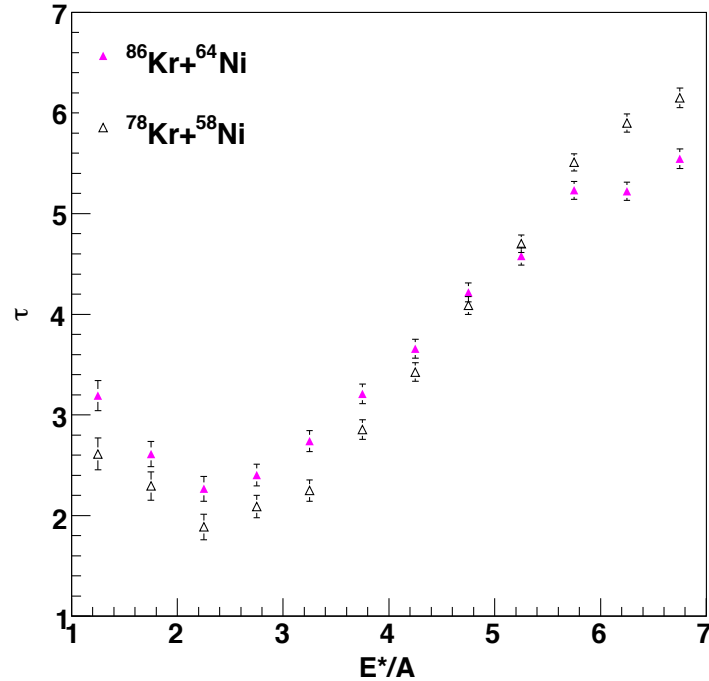
FIG. 53. Evolution of the fragment scaling τ as a function of system and E*/A for
I=0–2 fragments and A=11-24 using Eq. 6.2. (color online)

trend of increasing τ with increasing source N/Z seen in the last plot can be more
clearly seen here with the increased number of data points. For N/Z$_{meas}$ sources from
0.9–1.0, there is no significant change in τ as a function of source N/Z. However, the
individual fragment asymmetries still show a decrease in τ with increasing asymme-
try. The trend of increasing τ with increasing source N/Z seen in Fig. 51 is clearly
visible for N/Z$_{meas}$ $\geq$1.0. In light of the strong dependence of τ on the relative asym-
metry (I) of the measured fragments, the particle and system scaling are consistent.
In addition, the fragments exhibit a consistent sensitivity to the source asymmetry
regardless of the fragment I.

The insignificant change in τ as a function of source N/Z is also notably different
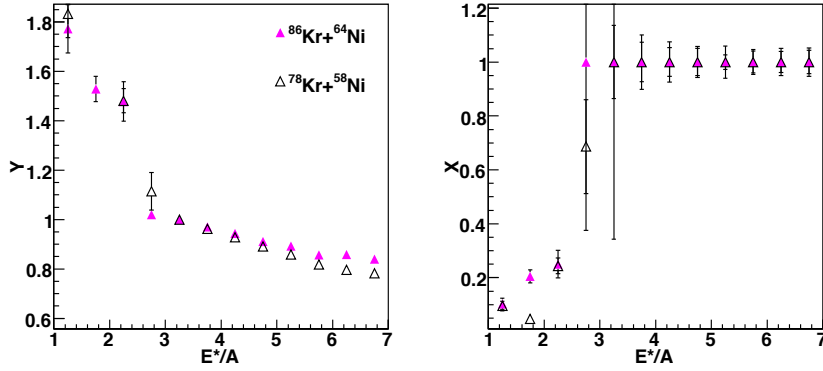
FIG. 54. Evolution of the X (surface) and Y (volume) parameters (Eq. 6.3) with respect to system excitation energy for the ^{86}Kr+^{64}Ni and ^{78}Kr+^{58}Ni systems for fragments with I=0–2. (color online)

than the results of Jandel *et al.* [9]. In that sumZ=12-15 study, the magnitude of τ_{min} increased more significantly with increasing N/Z. However, as reaction system size decreases the observed fragments will preferentially populate N∼Z isotopes. This may be the source of the similarity between this sumZ=30-34, I=0–2 and the sumZ=12-15 data.

The ^{78}Kr+^{58}Ni and ^{86}Kr+^{64}Ni mass distribution fitting with Eq. 6.2 was re-examined for fragments with I=0–2. The evolution of the τ parameter as a function of E*/A is shown in Fig. 53. Here the high energy tail of the distribution agrees between the two systems while value of τ_{min} is higher for the more neutron-rich source with respect to the less neutron-rich source. This behavior is similar to what was observed by Jandel *et al.* [9]. In that sumZ=12-15 study, the value of the τ_{min} increased with increasing N/Z as is seen here. The sumZ=12-15 study did not include free neutrons in the calculation of E*/A. Thus, the evolution of the position in E*/A of τ_{min} seen by Jandel *et al* cannot be compared to this data because of the difference in excitation energy calculations.

The I=0–2 mass distributions were also refitted with the modified scaling equation (Eq. 6.3). The same method was used for obtaining τ, X, and Y as above and yielded τ 2.73 (0.10) for ^{86}Kr+^{64}Ni and 2.24(0.11) for ^{78}Kr+^{58}Ni. However, in this case the 3.25 MeV bin was retained as the reference bin for consistency. The X and Y parameters are plotted in Fig. 54. The Y parameter is not appreciably different from the previous fitting (Fig. 50) across all isotopes. The X parameter is slightly lower with respect to the previous fitting for both sources. Both the volume and surface parameters retain source N/Z dependence.

The scaling methods (Eq. 6.2 and Eq. 6.3) implemented here provide some insight into the evolution of τ with respect to the N/Z$_{meas}$ of the source. Fitting with either equation illustrates the sensitivity of τ to the mass fitting region. Additionally, theory dictates that a single value of τ exist for a source. Thus, fitting with only the power law term (Eq. 6.2) shows the necessity of including the volume and surface terms to obtain a consistent value of τ across all energy bins. The source N/Z$_{meas}$ does not appear to make a statistically significant effect on the τ_{min} obtained with either Eq. 6.2 or Eq. 6.3 when fitting across all detected fragments. However, the surface and volume terms are sensitive to the source N/Z$_{meas}$.

In the scaling formulae investigated above (Eqs. 6.2 and 6.3), a consistent source N/Z dependence was observed. Thus, the fragments yields may also be parameterized by

$$Y = Y_0 A^{-\tau} e^{-\beta \Delta \mu A} \tag{6.5}$$

where Y is the yield, Y_0 is a normalization fitting parameter, τ is the scaling parameter, β is 1/T, and $\Delta\mu$ is the chemical potential difference between neutrons and protons which is the Gibbs free energy per nucleon (F(I/A)) [4]. At the energies and densities present in this data, this free energy is expected to be dominated by the

symmetry energy.

When using Eq. 6.5, the ratio of yields from two sources, differing only in neutron-to-proton ratio, may be related by:

$$R_{1,2} = Ce^{-\frac{\Delta FA}{T}}. \tag{6.6}$$

In this formula, C is a constant reflecting the ratios of the normalization parameters and ΔF is

$$\Delta F = (\mu_n - \mu_p)_1 - (\mu_n - \mu_p)_2 = \frac{N-Z}{A}\Delta H \tag{6.7}$$

where $\mu_{n,p}$ are the neutron and proton chemical potentials and ΔH is related to the difference in N/Z of the two sources. Scaling emerges when the -ln($R_{1,2}$)/A is plotted as a function of $\frac{N-Z}{A}$. The source N/Z_{meas} bins 1.0 - 1.06 (bin 2) and 1.2 - 1.26 (bin 4) were used to experimentally observe this scaling. The overall scaling obtained from the fragment yield ratios is plotted in Fig. 55 and exhibits a single linear slope corresponding to ΔH/T. In this plot, the ΔH/T is 0.983. The ΔH is linked to the symmetry energy coefficient C_{sym} through it's relation to the chemical potentials. However, the analytical derivation has not yet been established.

In the previous chapter, isoscaling was used to show the effect of source N/Z assumptions on experimental observables. However, isoscaling was originally derived to provide an experimental means to access the symmetry energy coefficient C_{sym} [73]. The analytical connection between isoscaling and C_{sym} is well established and has been utilized in experimental investigations of the nuclear symmetry energy [73, 75, 87, 88]. The α obtained from fitting the fragment yield ratios with Eq. 5.2 has been theoretically linked to C_{sym} through

$$\frac{\alpha}{\Delta} = \frac{4C_{sym}}{T} \tag{6.8}$$
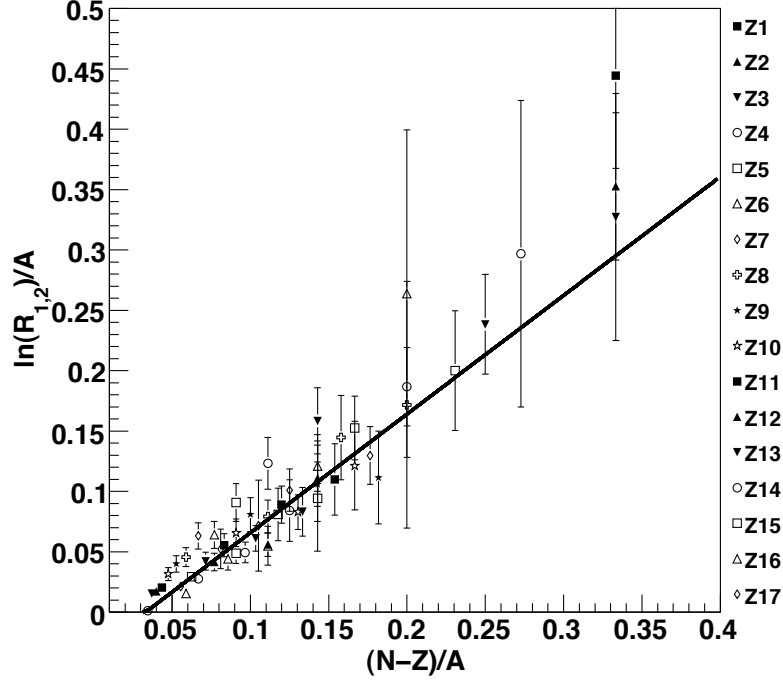
FIG. 55. Left: -ln(F/T)/A as a function of fragment (N-Z)/A. The slope of the fitted line corresponds to $\Delta H/T$.

where C_{sym} is the symmetry energy coefficient, T is temperature, and Δ is given by the following relationship

$$\Delta = \left(\frac{Z}{A}\right)_1^2 - \left(\frac{Z}{A}\right)_2^2. \tag{6.9}$$

Fig. 56 shows the isoscaling parameter α derived from various combinations of N/Z_{meas} bins. An additional point was included in Fig. 56 from the isoscaling of the ^{86}Kr+^{64}Ni and ^{78}Kr+^{58}Ni systems for the same quasi-projectile N/Z_{meas} bin (bin 2). This isoscaling provided a point with both the α and Δ very near zero. The α shows a linear dependence on the Δ calculated from the neutron-rich and neutron-poor sources. The slope of this linear dependence yields an average α/Δ of 15.9($\pm$0.3).

Using N/Z_{meas} bins 2 and 4, the evolution of α/Δ with respect to E^*/A can
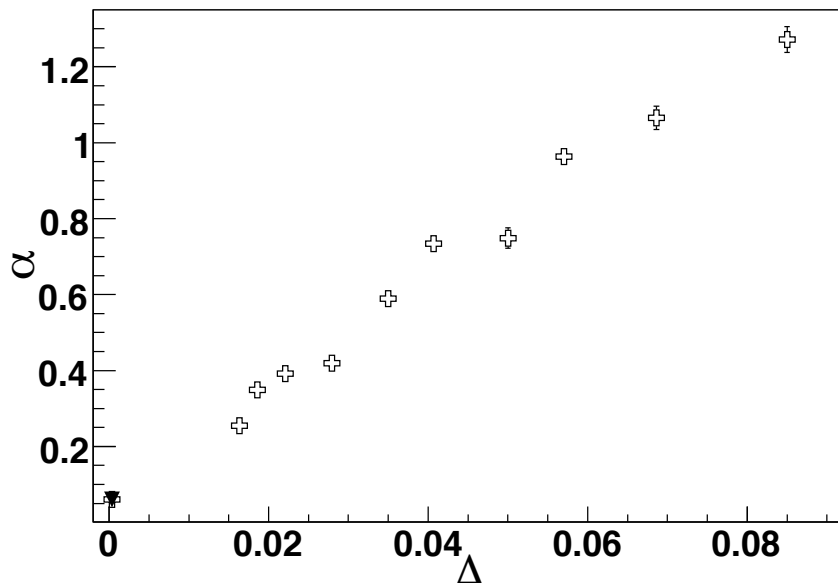
FIG. 56. Isoscaling α parameter as a function of the Δ of the reconstructed sources. The points were obtained from global α fits to combinations of five bins in N/Z (0.90–0.96,1.0–1.06, 1.1–1.16, 1.2–1.26, and 1.3–1.36) as a function of the calculated average $\Delta(Z/A)^2$ of the sources (Eq. 6.9). An additional point (triangle) is added from the isoscaling of ^{86}Kr+^{64}Ni and ^{78}Kr+^{58}Ni using the single N/Z bin 2 for each system. The propagated error on these values, where not visible, are smaller than the size of the points.

be seen in Fig. 57. The value of α/Δ is clearly decreasing with increasing source excitation energy. Because of the direct connection between α/Δ and C$_{sym}$, this decrease may indicate a decrease in C$_{sym}$ with increasing E*/A [89, 90]. However, to convert α/Δ into C$_{sym}$, the system temperature must be understood.

In the previous chapter, the source temperature was derived as a function of E*/A for this data. Over this 2.5-7.5 MeV E*/A region, the proton momentum fluctuation thermometer indicates a temperature change from $\sim$5.3 MeV to $\sim$7.2 MeV. Using T= 5.3 MeV, at E*/A =2.5 MeV/A, the measured α/Δ of $\sim$25 yields a C$_{sym}$ $\sim$26.6
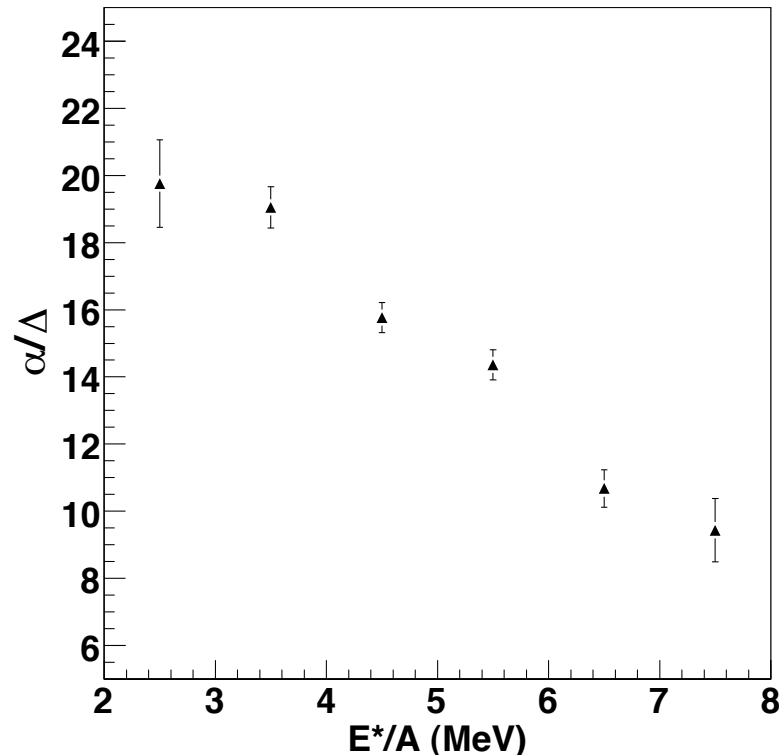
FIG. 57. Isoscaling α/Δ parameter as a function of the E^*/A of the reconstructed source. The source N/Z bins were chosen as 2 and 4. The propagated errors are based on fragment yields as described in the text.

MeV. Taking this same temperature of 5.3 MeV at E^*/A=7.5 MeV and α/Δ of 9.4 yields $C_{sym} \sim$12.6 MeV. However, if the temperature has indeed increased to 7.2 MeV at E^*/A=7.5 MeV the C_{sym} would become $\sim$16.7 MeV. Thus this change in temperature can account for less than 30% of the decrease in α/Δ observed here. From this estimation of ΔC_{sym}, it is clear that the change in temperature across this region is not sufficient to account for the observed decrease in the experimental α/Δ. The C_{sym} calculated for each excitation energy with constant and evolving temperature are plotted in Fig. 58. The decrease in C_{sym}, calculated with constant temperature, has the same overall shape as a function of E^*/A as the α/Δ plotted
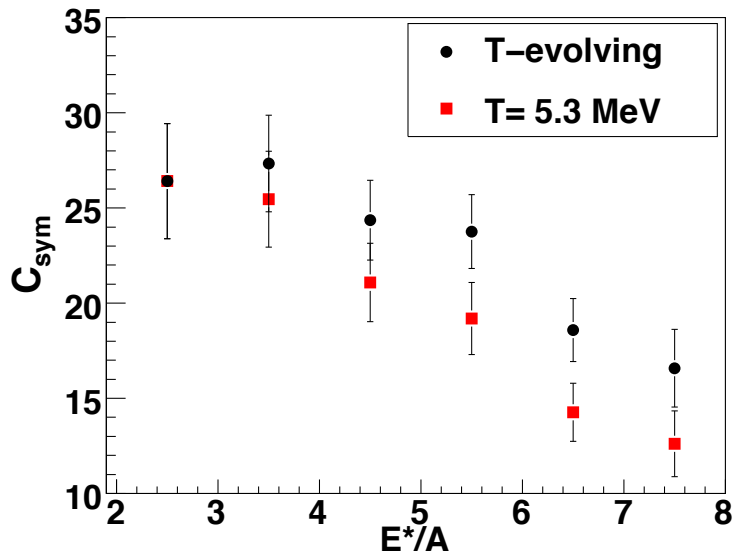
FIG. 58. $C_{sym}(E^*/A)$ derived from the isoscaling α/Δ and the the proton momentum fluctuation thermometer. Square symbols are calculated with constant T=5.3 MeV. Circles are calculated with evolving temperature. (color online)

above. In comparison, the evolution in C_{sym}, calculated with evolving values of temperature, shows a slightly flatter trend as a function of E^*/A.

To conclude, this chapter has focused on the source N/Z dependence of fragment yield scaling. A simple power law function (Eq. 6.2) was examined. This function is valid only near the phase transition region. The values of τ obtained were similar in the E^*/A=2-3 MeV region for the ^{86}Kr+^{64}Ni and ^{78}Kr+^{58}Ni systems. However, outside of this region the values varied significantly with the source N/Z. This behavior prompted analysis with the more complex yield function of Eq. 6.3 which incorporates terms for surface and volume. The taus for the ^{86}Kr+^{64}Ni and ^{78}Kr+^{58}Ni systems obtained with this second equation were well within errors of each other. The volume and surface terms, on the other hand, still exhibited significant sensitivity to the source N/Z.

To truly understand the fragment yields, a function incorporating an asymmetry term must be used. By including a fragment asymmetry term and taking the fragment yield ratio between the two sources, scaling studies become a useful method for understanding the neutron and proton chemical potentials and through these the symmetry energy coefficient C_{sym}. Eq. 6.6 relates the ratio of fragment yields to the free energy which at these temperatures and densities is likely dominated by the symmetry energy. The analytical connection between the scaling slope and C_{sym} has not been derived. However, isoscaling provides a connection between fragment yield ratios and C_{sym} through Eqs. 5.2 and 6.8. Isoscaling of this thesis data indicates that the symmetry energy coefficient (C_{sym}) decreases with increasing excitation energy of the source. The decrease seen in C_{sym} as a function of E^*/A is not removed by the change in source temperature.

CHAPTER VII

CONCLUSIONS

A widely studied group of experimental observables in nuclear physics are utilized to study the effects of the two component nature of nuclei. Asymmetry of the neutron to proton ratio contributes to the binding energy of nuclei across all temperatures and densities. This thesis has probed two groups of experimental observables for their dependence on this portion of the nuclear equation of state.

Fragment yield scaling was explored to study the source N/Z dependence of this observable. First, the yield was related to the mass of a fragment through a simple power law (Eq. 6.2). This function is valid only near the phase transition region and outside of this region the measured values varied significantly with the source N/Z. A more complex function with power law, volume, and surface terms (Eq. 6.3) was investigated next. The taus for the ^{86}Kr+^{64}Ni and ^{78}Kr+^{58}Ni systems obtained with this second equation were well within errors of each other. However, the volume and surface terms still exhibited significant sensitivity to the source N/Z. Both of these analyses indicated a strong sensitivity to the source N/Z. Thus, to truly understand the fragment yields, a function incorporating an asymmetry term must be used (Eq. 6.5). This term accounts for the effect of source N/Z on fragment yields through the neutron and proton chemical potentials. These chemical potentials provide a connection to the symmetry energy coefficient C$_{sym}$.

In scaling studies, the symmetry energy coefficient C$_{sym}$ may be accessed experimentally through the ratio of fragment yields from two sources differing in N/Z. In this thesis, isoscaling provided the connection between fragment yield ratios and C$_{sym}$ through Eqs. 5.2 and 6.8. This data indicates that the isoscaling α/Δ parameter decreases as the source E*/A increases. This trend of decreasing α/Δ has been

observed previously and linked to a decrease in C_{sym} with increasing E^*/A [90, 89].

To demonstrate that C_{sym} decreases with increasing E^*/A, the source temperature must be known. This thesis has examined the experimental temperature dependence on source N/Z_{meas} through constructing caloric curves. The nuclear caloric curve was studied using three methods of calculating nuclear temperature: the double isotope thermometer, the slope thermometer from moving source fits, and the momentum fluctuation thermometer.

The temperatures measured with the double isotope ratio thermometer were relatively low compared to those obtained with the other thermometers and reference caloric curves. These low values are partially remedied by secondary decay corrections. These corrections did not change any source N/Z trends but only altered the absolute value of temperature by $\sim 20\%$. In addition, the temperatures obtained with this thermometer may be affected by the method of source selection as well as the assumptions about the nuclear fragmentation mechanism. The double isotope thermometer showed a sensitivity to the source N/Z. This dependence was introduced through strong sensitivity of the $N<Z$ isotopes to the source N/Z.

The slope thermometer, on the other hand, did not show any statistically significant dependence on the source neutron to proton ratio. This thermometer yielded consistent temperatures across the $Z=4-7$ intermediate mass fragments. The apparent temperatures from the slope thermometer exhibit a combination of thermal energy, Fermi momentum of nucleons, and collective motion of the fragments along the beam axis.

The momentum fluctuation thermometer was the third thermometer investigated. This thermometer exhibits a small, residual contamination from the collective motion of the fragments along the beam axis. For this reason, the transverse direction has been explored. Additionally, a mass dependence was observed for this thermome-
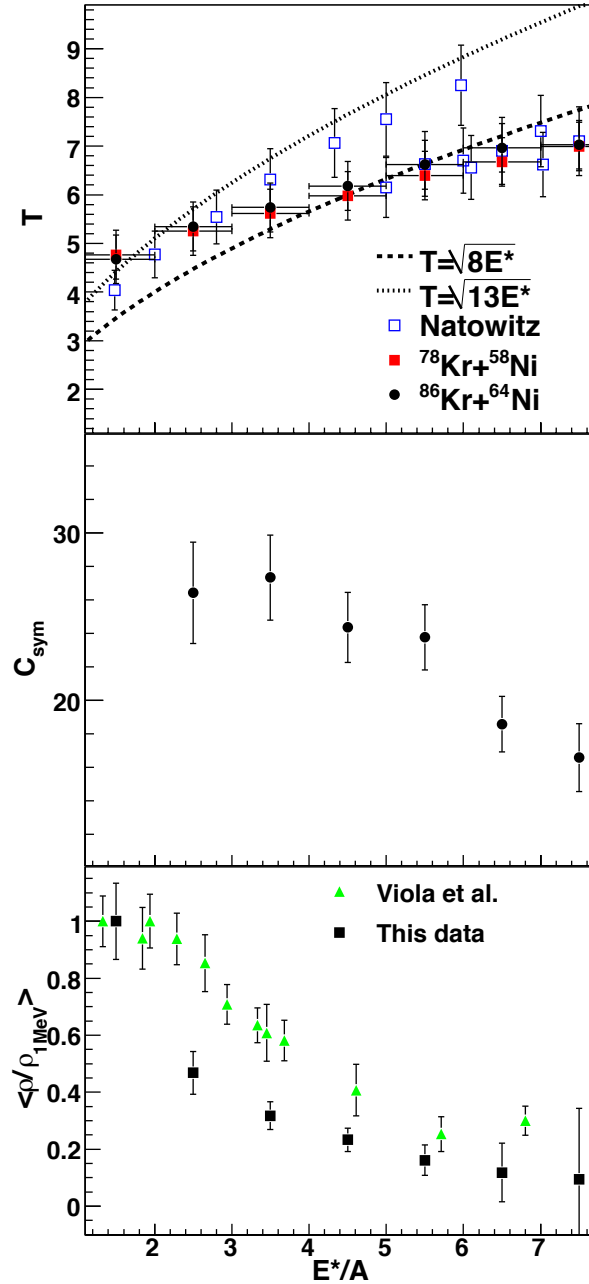
FIG. 59. Re-plotting of: Top) the Proton transverse momentum fluctuation thermometer for the ^{78}Kr+^{58}Ni and ^{86}Kr+^{64}Ni systems. Additionally, the Natowitz [28] compilation for A=60–100 and two Fermi gas curves are also plotted. Middle) C_{sym} obtained from isoscaling and the proton fluctuation thermometer as a function of the source E*/A. Bottom) Average density obtained from moving source fits to Z=3–7 fragments is plotted in solid squares. In addition, the solid triangles are experimentally obtained densities from light-ion reactions [83]. (color online)

ter. This mass dependence may be the result of Fermi momentum of nucleons. This effect is defined as zero for protons; consequently, the proton transverse momentum fluctuations were used to investigate the temperature dependence on the source N/Z.

The proton momentum fluctuation thermometer is re-plotted in the top panel of Fig. 59 for the ^{78}Kr+^{58}Ni and ^{86}Kr+^{64}Ni systems. For reference, the compilation of Natowitz *et al.* [28] and two Fermi Gas curves ($T = \sqrt{aE^*/A}$ with a = 8, 13) are plotted. As shown in this figure, the proton momentum temperatures are similar to what is obtained from a Fermi Gas at low E^*/A and are consistent with the Natowitz compilation [28] throughout the E^*/A range. Source N/Z dependence of the measured temperature is well within errors for the ^{78}Kr+^{58}Ni and ^{86}Kr+^{64}Ni systems.

The temperatures obtained from the proton momentum fluctuation thermometer were used to convert the isoscaling α/Δ to C_{sym}. C_{sym} shows a decreasing trend as a function of E^*/A. This result is re-plotted here as the middle panel of Fig. 59. It should be noted that the experimental values of α obtained here may be modified by fragment secondary decays [91].

The asymmetry term of the nuclear equation of state is a function of both the temperature and density of the source. The density of the ^{78}Kr+^{58}Ni and ^{86}Kr+^{64}Ni systems was calculated from moving source fitting of the data. The average system density, re-plotted in Fig. 59, was calculated by averaging the density extracted from fitting the kinetic energy spectra of the Z=3–7 elements from the ^{78}Kr+^{58}Ni and ^{86}Kr+^{64}Ni systems. The density is clearly falling over the E^*/A = 1.5-7.5 range. The rate of decrease is greatest at low E^*/A though the density evolves over the entire excitation energy range. For reference, density points as a function of E^*/A are also included in the bottom panel of Fig. 59 from the analysis of Viola et al [83]. These two data sets provide upper and lower bounds for the change in density as a function of E^*/A.

In conclusion, the proton fluctuation thermometer, derived in this thesis and implemented on this data, does not indicate a significant dependence of the measured temperature on the source N/Z. In addition, this thesis has shown that the experimentally obtained symmetry energy coefficient C_{sym} is decreasing by as much as 60% over the E^*/A=2.5–7.5 range. Additionally, both the temperature and density of the source evolve as the E^*/A increases. The momentum thermometer indicates that the temperature increases by ∼15-25% across the E^*/A=2.5–7.5 MeV region. Meanwhile, across this same E^*/A=2.5–7.5 MeV region, the density decreases by ∼50–75%. Thus, the experimentally observed decrease in C_{sym} with E^*/A is well correlated to the temperature and density changes observed in this data.

REFERENCES

[1] J. Finn, S. Agarwal, A. Bujak, J. Chuang, L. Gutay, A. Hirsch, R. Minich, N. Porile, R. Scharenberg, and B. Stringfellow, Phys. Rev. Lett. **49**, 1321 (1982).

[2] S. Hojjati, Jour. of Young Invest. **11** (2004).

[3] R. Wada, R. Tezkratt, K. Hagel, F. Haddad, A. Kolomiets, Y. Lou, J. L. N. M. Shimooka, S. Shlomo, D. Utley, B. Xiao, N. Mdeiwayeh, and J. Natowitz, Phys. Rev. C **55**, 227 (1997).

[4] A. Bonasera, Z. Chen, R. Wada, K. Hagel, J. Natowitz, P. Sahu, L. Qin, S. Kowalski, T. Keutgen, T. Materna, and T. Nakagawa, Phys. Rev. Lett. **101**, 122702 (2008).

[5] V. Viola, K. Kwiatkowski, L. Beaulieu, D. Bracken, H. Breuer, J. Brzychczyk, R. de Souza, D. Ginger, W. Hsi, R. Korteling, T. Lefort, W. Lynch, K. Morley, R. Legrain, L. Pienkowski, E. Pollacco, E. Renshaw, A. Ruangma, M. Tsang, C. Volant, G. Wang, S. Yennello, and N. Yoder, Phys. Rep. **434**, 1 (2006).

[6] P. Mastinu, M. Belkacen, M. D'Agostino, M. Bruno, P. Milazzo, G. Vannini, D. R. Bowman, N. Colonna, J. D. Dinius, A. Ferrero, M. L. Fiandri, C. K. Gelbke, T. Glasmacher, F. Gramegna, D. O. Handzy, D. Horn, W. C. Hsi, M. Huang, I. Iori, G. J. Kunde, M. A. Lisa, W. G. Lynch, G. V. Margagliotti, C. P. Montoya, A. Moroni, G. F. Peaslee, F. Petruzzelli, R. Rui, C. Schwarz, M. B. Tsang, C. Williams, V. Latora, and A. Bonasera, Phys. Rev. Lett. **76**, 2646 (1996).

[7] N. LeNeindre, E. Bonnet, J. Wieleczko, B. Borderie, F. Gulminelli, M. Rivet, R. Bougault, A. Chbihi, R. Dayras, J. Frankland, E. Galichet, D. Guinet,

P. Lautesse, A. L. Fèvre, O. Lopez, J. Lukasik, D. Mercier, J. Moisan, M. Pârlog, E. Rosato, R. Roy, C. Schwarz, C. Sfienti, B. Tamain, W. Trautmann, A. Trzcinski, K. Turzo, E. Vient, M. Vigilante, and B. Zwieglinski, Nucl. Phys. A **795**, 47 (2007).

[8] Y. Ma, R. Wada, K. Hagel, J. Wang, T. Keutgen, Z. Majka, M. Murray, L. Qin, P. Smith, J. B. Natowitz, R. Alfaro, J. Cibor, M. Cinausero, Y. E. Masri, D. Fabris, E. Fioretto, A. Keksis, M. Lunardon, A. Makeev, N. Marie, E. Martin, A. Martinez-Davalos, A. Menchaca-Rocha, G. Nebbia, G. Prete, V. Rizzi, A. Ruangma, G. Souliotis, P. Staszel, M. Veselsky, G. Viesti, E. M. Winchester, and S. J. Yennello, Phys. Rev. C **69**, 031604(R) (2004).

[9] M. Jandel, S. Wuenschel, D. Shetty, G. Souliotis, A. Keksis, and S. Yennello, Phys. Rev. C **74**, 054608 (2006).

[10] A. Kelic, J. Natowitz, and K. Schmidt, Eur. Phys. J. A **30**, 203 (2006).

[11] V. Viola and R. Bougault, Eur. Phys. J. A **30**, 215 (2006).

[12] Y. Ma, Eur. Phys. J. A **30**, 227 (2006).

[13] B. Borderie and M. Rivet, Prog. in Part. and Nucl. Phys. **64**, 551 (2008).

[14] J. Besprosvany and S. Levitt, Phys. Lett. B **217**, 1 (1989).

[15] P. Chomaz and F. Gulminelli, Phys. Lett. B **447**, 221 (1999).

[16] C. Hoel, L. Sobotka, and R. Charity, Phys. Rev. C **75**, 017601 (2007).

[17] W. Trautman, C. Sfienti, P. Adrich, T. Aumann, C. Bacri, T. Barczyk, R. Bassini, S. Bianchin, C. Boiano, A. Botvina, A. Boudard, J. Brzychczyk, A. Chbihi, J. Cibor, B. Czech, M. D. Napoli, J. Ducret, H. Emling, J. Frankland,

M. Hellstroem, D. Henzlova, G. Imme, I. Iori, H. Johansson, K. Kezzar, A. Lafri-akh, A. L. Fevre, E. L. Gentil, Y. Leifels, J. Luehning, J. Lukasik, W. Lynch, U. Lynen, Z. Majka, M. Mocko, W. Mueller, A. Mykulyak, H. Orth, A. Otte, R. Palit, P. Pawlowski, A. Pullia, G. Raciti, E. Rapisarda, H. Sann, C. Schwarz, H. Simon, K. Suemmerer, M. Tsang, G. Verde, C. Volant, M. Wallace, H. Weick, J. Wiechula, A. Wieloch, and B. Zwieglinski, arXiv:0807.5102 .

[18] W. Friedman, Phys. Rev. Lett. **60**, 2125 (1988).

[19] D. Lacroix, A. V. Lauwe, and D. Durand, Phys. Rev. C **69**, 054604 (2004).

[20] A. Ono, Phys. Rev. C **59**, 853 (1999).

[21] M. Papa, T. Maruyama, and A. Bonasera, Phys. Rev. C **64**, 024612 (2001).

[22] K. S. Krane, *Introductory Nuclear Physics*, 1st ed. (Wiley, New York, 1987).

[23] R. A. Dunlap, *An Introduction to the Physics of Nuclei and Particles* (Thomson Learning, Belmont, CA, 2004).

[24] G. Satchler, Phys. Rev. **109**, 429 (1958).

[25] M. Fisher, Physics **3**, 255 (1967).

[26] R. Minich, S. Agarwal, A. Bujak, J. Chuang, J. Finn, L. Gutay, A. Hirsch, N. Porile, R. Scharenberg, and B. Stringfellow, Phys. Lett. B **118**, 458 (1982).

[27] A. Hirsch, A. Bujak, J. Finn, L. Gutay, R. Minich, N. Porile, R. Scharenberg, B. Stringfellow, and F. Turkot, Phys. Rev. C **29**, 508 (1984).

[28] J. Natowitz, R. Wada, K. Hagel, T. Keutgen, M. Murray, A. Makeev, L. Qin, P. Smith, and C. Hamilton, Phys. Rev. C **65**, 034618 (2002).

[29] M. Baldo, Y. Cai, G. Giansiracusa, U. Lombardo, and H. Song, Phys. Lett. B **340**, 13 (1994).

[30] S. Wuenschel, R. Dienhoffer, G. Souliotis, S. Galanopoulos, Z. Kohley, K. Hagel, D. Shetty, K. Huseman, L. May, S. Soisson, B. Stein, A. Caraley, and S. Yennello, Phys. Rev. C **79**, 061602 (2009).

[31] D. Rowland, R. Laforest, E. Ramakrishnan, M. Veselsky, E. Winchester, A. Ruangma, E. Martin, and S. Yennello, Phys. Rev. C **67**, 064602 (2003).

[32] P. Chomaz, AIP Conf. Proc. **610**, 167 (2002).

[33] M. D'Agostino, A. Botvina, M. Bruno, A. Bonasera, J. Bondorf, R. Bougault, P. Desesquelles, E. Garaci, F. Gulminelli, I. Iori, N. LeNeindre, G. Margagliotti, I. Mishustin, A. Moroni, A. Pagano, and G. Vannini, Nucl. Phys. A **650**, 329 (1999).

[34] Y. Ma, J. Natowitz, R. Wada, K. Hagel, J. Wang, T. Keutgen, Z. Majka, M. Murray, L. Qin, P. Smith, R. Alfaro, J. Cibor, M. Cinausero, Y. E. Masri, D. Fabris, E. Fioretto, A. Keksis, M. Lunardon, A. Makeev, N. Marie, E. Martin, A. Martinez-Davalos, A. Menchaca-Rocha, G. Nebbia, G. Prete, V. Rizzi, A. Ruangma, D. V. Shetty, G. Souliotis, P. Staszel, M. Veselsky, G. Viesti, E. M. Winchester, and S. J. Yennello, Phys. Rev. C **71**, 054606 (2005).

[35] F. Gulminelli and P. Chomaz, Int. Jour. of Mod. Phys. E **8**, 527 (1999).

[36] S. Albergo, S. Costa, E. Costanzo, and A. Rubbino, Nuovo Cimento **89**, 1 (1985).

[37] M. Tsang, W. Lynch, H. Xi, and W. Friedman, Phys. Rev. Lett. **78**, 3836 (1997).

[38] D. Tamain, E. Durand, and B. Suraud, *Nuclear Dynamics in the Nucleonic Regime* (Institute of Physics, Bristol and Philadelphia, 2001).

[39] R. Wada, D. Fabris, K. Hagel, G. Nebbia, Y. Lou, M. Gonin, J. B. Natowitz, R. Billerey, B. Cheynis, A. Demeyer, D. Drain, D. Guinet, C. Pastor, L. Vagneron, K. Zaid, J. Alarja, A. Giorni, D. Heuer, C. Morand, B. Viano, C. Mazur, C. Ng, S. Leray, R. Lucas, M. Ribrag, and E. Tomasi, Phys. Rev. C **39**, 497 (1989).

[40] T. Odeh, R. Bassini, M. Begemann-Blaich, S. Fritz, S. Gaff-Ejakov, D. Gourio, C. Gross, G. Imme, I. Iori, U. Kleinevo, G. J. Kunde, W. D. Kunze, U. Lynen, V. Maddalena, M. Mahi, T. Mohlenkamp, A. Moroni, W. F. J. Muller, C. Nociforo, B. Ocker, F. Petruzzelli, J. Pochodzalla, G. Raciti, G. Riccobene, F. P. Romano, A. Saija, and M. Schnittker, Phys. Rev. Lett. **84**, 4557 (2000).

[41] A. Ruangma, *Caloric Curve of 8 GeV/c Pion and Anti-proton + 197Au Reactions*, PhD thesis, Texas A&M University, 2002.

[42] W. Bauer, Phys. Rev. C **51**, 803 (1995).

[43] S. Jeong, D. Cussol, D. Durand, R. Laforest, J. Peter, J. C. Angélique, G. Auger, G. Bizard, R. Brou, A. Buta, C. Cabot, Y. Cassagnou, E. Crema, Y. E. Masri, P. Eudes, Z. Y. He, A. Kerambrun, C. Lebrun, R. Legrain, J. P. Patry, A. Péghaire, R. Régimbart, E. Rosato, F. Saint-Laurent, J. C. Steckmeyer, B. Tamain, and E. Vient, Nucl. Phys. A **604**, 208 (1996).

[44] W. C. Hsi, G. J. Kunde, J. Pochodzalla, W. G. Lynch, M. B. Tsang, M. L. Begemann-Blaich, D. R. Bowman, R. J. Charity, F. Cosmo, A. Ferrero, C. K. Gelbke, T. Glasmacher, T. Hofmann, G. Imme, I. Iori, J. Hubele, J. Kempter, P. Kreutz, W. D. Kunze, V. Lindenstruth, M. A. Lisa, U. Lynen, M. Mang, A. Moroni, W. F. J. Muller, M. Neumann, and B. Ocker, Phys. Rev. Lett. **73**, 3367 (1994).

[45] G. Imme, W. Trautman, C. Sfienti, P. Adrich, T. Aumann, C. Bacri, T. Barczyk, R. Bassini, S. Bianchin, C. Boiano, A. Botvina, A. Boudard, J. Brzychczyk, A. Chbihi, J. Cibor, B. Czech, M. D. Napoli, J. Ducret, H. Emling, J. Frankland, M. Hellstroem, D. Henzlova, , I. Iori, H. Johansson, K. Kezzar, A. Lafriakh, A. L. Fevre, E. L. Gentil, Y. Leifels, J. Luehning, J. Lukasik, W. Lynch, U. Lynen, Z. Majka, M. Mocko, W. Mueller, A. Mykulyak, H. Orth, A. Otte, R. Palit, P. Pawlowski, A. Pullia, G. Raciti, E. Rapisarda, H. Sann, C. Schwarz, H. Simon, K. Suemmerer, M. Tsang, G. Verde, C. Volant, M. Wallace, H. Weick, J. Wiechula, A. Wieloch, and B. Zwieglinski, arXiv:nucl-ex/9607003v1 (1996).

[46] J. Pochodzalla, T. Mohlenkamp, T. Rubehn, A. Schuttauf, A. Worner, E. Zude, M. Begemann-Blaich, T. Blaich, H. Emling, A. Ferrero, C. Gross, G. Imme, I. Iori, G. J. Kunde, W. D. Kunze, V. Lindenstruth, U. Lynen, A. Moroni, W. F. J. Muller, B. Ocker, G. Raciti, H. Sann, C. Schwarz, W. Seidel, V. Serfling, J. Stroth, and W. Trautmann, Phys. Rev. Lett. **75**, 1040 (1995).

[47] W. Trautman, C. Sfienti, P. Adrich, T. Aumann, C. Bacri, T. Barczyk, R. Bassini, S. Bianchin, C. Boiano, A. Botvina, A. Boudard, J. Brzychczyk, A. Chbihi, J. Cibor, B. Czech, M. D. Napoli, J. Ducret, H. Emling, J. Frankland, M. Hellstroem, D. Henzlova, G. Imme, I. Iori, H. Johansson, K. Kezzar, A. Lafriakh, A. L. Fevre, E. L. Gentil, Y. Leifels, J. Luehning, J. Lukasik, W. Lynch, U. Lynen, Z. Majka, M. Mocko, W. Mueller, A. Mykulyak, H. Orth, A. Otte, R. Palit, P. Pawlowski, A. Pullia, G. Raciti, E. Rapisarda, H. Sann, C. Schwarz, H. Simon, K. Suemmerer, M. Tsang, G. Verde, C. Volant, M. Wallace, H. Weick, J. Wiechula, A. Wieloch, and B. Zwieglinski, Phys. Rev. C **76**, 064606 (2007).

[48] T. Lefort, L. Beaulieu, A. Botvina, D. Durand, K. Kwiatkowski, W.-c. Hsi, L. Pienkowski, H. Breuer, R. G. Korteling, R. Laforest, E. Martin, E. Ramakr-

ishnan, D. Rowland, A. Ruangma, V. E. Viola, E. Winchester, and S. J. Yennello, Phys. Rev. C **62**, 031604 (2000).

[49] S. Wuenschel, K. Hagel, R. Wada, J. Natowitz, S. Yennello, Z. Kohley, C. Bottosso, L. May, W. Smith, D. Shetty, B. Stein, S. Soisson, and G. Prete, Nucl. Instrum. Methods Phys. Res. A **604**, 578 (2009).

[50] K. Kwiatkowski, D. Bracken, K. Morley, J. Brzychczyk, E. Renshaw-Foxford, K. Komisarcik, V. E. Viola, N. R. Yoder, J. Dorsett, J. Poehlman, N. Madden, and J. Ottarson, Nucl. Instrum. Methods Phys. Res. A **360**, 571 (1995).

[51] J. Pouthas, B. Borderie, R. Dayras, E. Plagnol, M. Rivet, F. Saint-Laurent, J. Steckmeyer, G. Auger, C. Bacri, S. Barbey, A. Barbier, A. Benkirane, J. Benlliure, B. Berthier, E. Bougamont, P. Bourgault, P. Box, R. Bzyl, B. Cahan, Y. Cassagnou, D. Charlet, J. Char-vet, A. Chbihi, T. Clerc, N. Copinet, D. Cuss01, M. Engrand, J. Gautier, Y. Huguet, . Jouniaux, J. Laville, P. L. Botlan, A. Leconte, R. Legrain, P. Lelong, M. L. Guay, L. Martina, C. Mazur, P. Mosrin, L. Olivier, J. Passerieux, S. Pierre, B. Piquet, E. Plaige, E. Pollacco, B. Raine, A. Richard, J. Ropert, C. Spitaels, L. Stab, D. Sznajderman, L. Tassangot, J. Tillier, M. Tripon, P. Vallerand, C. Volant, P. Volkov, J. Wieleczko, and G. Wittwer, Nucl. Instrum. Methods Phys. Res. A **357**, 418 (1995).

[52] R. Schmitt, L. Cooke, G. Derrig, D. Fabris, B. Hurst, J. Natowitz, G. Nebbia, D. OKelly, B. Srivastava, W. Turmel, D. Utley, H. Utsunomiya, and R. Wada, Nucl. Instrum. Methods Phys. Res. A **354**, 487 (1995).

[53] R. Wada, T. Keutgen, K. Hagel, Y. Ma, J. Wang, M. Murray, L. Qin, P. Smith, J. B. Natowitz, R. Alfarro, J. Cibor, M. Cinausero, Y. E. Masri, D. Fabris,

E. Fioretto, A. Keksis, S. Kowalski, M. Lunardon, A. Makeev, N. Marie, E. Martin, Z. Majka, A. Martinez-Davalos, A. Menchaca-Rocha, G. Nebbia, G. Prete, V. Rizzi, A. Ruangma, D. V. Shetty, G. Souliotis, P. Staszel, M. Veselsky, G. Viesti, E. M. Winchester, S. J. Yennello, W. Zipper, and A. Ono, Phys. Rev. C **69**, 044610 (2004).

[54] Geant http://wwwasd.web.cern.ch/wwwasd/geant/.

[55] C. Zeitnitz and T. Gabriel, Nucl. Instrum. Methods Phys. Res. A **349**, 106 (1994).

[56] J. Poitou and C. Signarbieux, Nucl. Instrum. Methods Phys. Res. A **114**, 113 (1974).

[57] Srim http://www.srim.org, 2009.

[58] R. Brun and F. Rademakers, Nucl. Instrum. Methods Phys. Res. A **389**, 81 (1997).

[59] B. Davin, R. deSouza, R. Yanez, Y. Larochelle, R. Alfaro, H. Xu, A. Alexander, K. Bastin, L. Beaulieu, J. Dorsett, G. Fleener, L. Gelovani, T. Lefort, J. Poehlman, R. Charity, L. Sobotka, J. Elson, A. Wagner, T. Liu, X. Liu, W. Lynch, L. Morris, R. Shomin, W. Tan, M. Tsang, G. Verde, and J. Yurkon, Nucl. Instrum. Methods Phys. Res. A **473**, 302 (2001).

[60] Pico systems www.pico-systems.com.

[61] S. Wuenschel, K. Hagel, L. May, R. Wada, and S. Yennello, AIP Conf. Proc. **1099**, 816 (2009).

[62] L. May, Z. Kohley, S. Wuenschel, K. Hagel, R. Wada, and S. Yennello, Nucl. Instrum. Methods Phys. Res. A (in progress) .

[63] M. Mocko, M. Tsang, L. Andronenko, M. Andronenko, F. Deluanay, M. Famiano, T. Ginter, V. Henzl, D. Henzlova, H. Hua, S. Lukyanov, W. G. Lynch, A. M. Rogers, M. Steiner, A. Stolz, O. Tarasov, M. van Goethem, G. Verde, W. S. Wallace, and A. Zalessov, Phys. Rev. C **74**, 054612 (2006).

[64] G. Souliotis, M. Veselsky, D. Shetty, L. Trache, and S. Yennello, Nucl. Phys. A **746**, 526c (2004).

[65] L. Tassan-Got, Nucl. Instrum. Methods Phys. Res. B **194**, 503 (2002).

[66] A. Bonasera, M. di Toro, and C. Gregoire, Nucl. Phys. A **463**, 653 (1987).

[67] J. Steckmeyer, E. Genouin-Duhamel, E. Vient, J. Colin, D. Durand, R. Bougault, B. Bouriquet, R. Brou, P. Buchet, J. Charvet, A. Chbihi, D. Cussol, R. Dayras, N. DeCesare, A. Demeyer, D. Dore, J. Frankland, E. Galichet, E. Gerlic, D. Guinet, S. Hudan, P. Lautesse, F. Lavaud, J. Laville, J. Lecolley, C. Leduc, R. Legrain, N. L. Neindre, O. Lopez, M. Louvel, A. Maskay, L. Nalpas, J. Normand, M. Parlog, P. Pawłowski, E. Plagnol, M. Rivet, E. Rosato, F. Saint-Laurent, G. Tabacaru, B. Tamain, L. Tassan-Got, O. Tirel, K. Turzo, M. Vigilante, C. Volant, and J. Wieleczko, Nucl. Phys. A **686**, 537 (2001).

[68] D. Dore, P. Buchet, J. Charvet, R. Dayras, L. Nalpas, D. Cussol, N. Bellaize, F. Bocage, R. Bougault, B. Bouriquet, R. Brou, A. Chbihi, J. Colin, A. Demeyer, D. Durand, J. Frankland, E. Galichet, E. Genouin-Duhamel, E. Gerlic, D. Guinet, S. Hudan, P. Lautesse, F. Lavaud, J. Laville, J. Lecolley, C. Leduc, N. L. Neindre, O. Lopez, M. Louvel, A. Maskay, J. Normand, M. Parlog, P. Pawlowski, E. Plagnol, M. Rivet, E. Rosato, F. Saint-Laurent, J. Steckmeyer, M. Stern, G. Tabacaru, B. Tamain, L. Tassan-Got, O. Tirel, E. Vient, and J. Wieleczko, Phys. Lett. B **491**, 15 (2000).

[69] T. Lefort, L. Beaulieu, K. Kwiatkowskit, W. Hsi, V. Viola, R. Laforest, E. Martin, E. Ramakrishnan, D. Rowland, A. Ruangma, E. winchester, S. Yennello, L. Pienkowski, R. Korteling, and H. Breuer, Phys. Rev. C **64**, 064603 (2001).

[70] V. Viola, Private communication.

[71] V. Viola, K. Kwiatkowski, and W. Friedman, Phys. Rev. C **59**, 2660 (1999).

[72] M. Tsang, C. Gelbke, X. Liu, W. Lynch, W. Tan, G. Verde, H. Xu, W. Friedman, R. Donangelo, S. Souza, C. Das, S. DasGupta, and D. Zhabinsky, Phys. Rev. C **64**, 054615 (2001).

[73] M. Tsang, W. Friedman, C. Gelbke, W. Lynch, G. Verde, and H. Xu, Phys. Rev. Lett. **86**, 5023 (2001).

[74] H. S. Xu, M. B. Tsang, T. X. Liu, X. D. Liu, W. G. Lynch, W. P. Tan, A. VanderMolen, G. Verde, A. Wagner, H. F. Xi, C. K. Gelbke, L. Beaulieu, B. Davin, Y. Larochelle, T. Lefort, R. T. deSouza, R. Yanez, V. E. Viola, R. J. Charity, and L. G. Sobotka, Phys. Rev. Lett. **85**, 716 (2000).

[75] M. Tsang, W. Friedman, C. Gelbke, W. Lynch, G. Verde, and H. Xu, Phys. Rev. C **64**, 041603(R) (2001).

[76] A. S. Botvina, O. V. Lozhkin, and W. Trautmann, Phys. Rev. C **65**, 044610 (2002).

[77] D. Shetty, G. Souliotis, S. Galanopoulos, Z. Kohley, S. Soisson, B. Stein, S. Wuenschel, and S. Yennello, [nucl-ex] arXiv:0802.0664v1 .

[78] S. Galanopoulos, G. Souliotis, M. Jandel, D. Shetty, Z. Kohley, S. Soisson, B. Stein, S. Wuenschel, and S. Yennello, AIP Conf. Proc. **1099**, 786 (2009).

[79] L. Tassan-Got and C. Stephan, Nucl. Phys. A **524**, 121 (1991).

[80] J. Bondorf, A. Botvina, A. Iljinov, I. Mishustin, and K. Sneppen, Phys. Rep. **257**, 133 (1995).

[81] J. Wang, R. Wada, T. Keutgen, K. Hagel, Y. Ma, M. Murray, L. Qin, A. Botvina, S. Kowalski, T. Materna, J. B. Natowitz, R. Alfarro, J. Cibor, M. Cinausero, Y. ElMasri, D. Fabris, E. Fioretto, A. Keksis, M. Lunardon, A. Makeev, N. Marie, E. Martin, Z. Majka, A. Martinez-Davalos, A. Menchaca-Rocha, G. Nebbia, G. Prete, V. Rizzi, A. Ruangma, D. V. Shetty, G. Souliotis, P. Staszel, M. Veselsky, G. Viesti, E. M. Winchester, S. J. Yennello, and W. Zipper, Phys. Rev. C **72**, 024603 (2005).

[82] L. Moretto, Nucl. Phys. A **247**, 211 (1975).

[83] V. Viola, K. Kwiatkowski, J. Natowitz, and S. Yennello, Phys. Rev. Lett. **93**, 132701 (2004).

[84] J. B. Natowitz, K. Hagel, Y. Ma, M. Murray, L. Qin, S. Shlomo, R. Wada, and J. Wang, Phys. Rev. C **66**, 031601(R) (2002).

[85] E. Winchester, J. Winger, R. Laforest, E. Martin, E. Ramakrishnan, D. Rowland, A. Ruangma, S. Yennello, G. Westfall, A. VanderMolen, and E. Norbeck, Phys. Rev. C **63**, 014601 (2001).

[86] M. Belkacem, V. Latora, and A. Bonasera, Phys. Rev. C **52**, 271 (1995).

[87] G. Souliotis, M. Veselsky, D. Shetty, and S. Yennello, Phys. Lett. B **588**, 35 (2004).

[88] D. Shetty, S. Yennello, E. Martin, A. Keksis, and G. Souliotis, Phys. Rev. C **68**, 021602 (2003).

[89] G. Souliotis, A. Botvina, D. Shetty, A. Keksis, M. Jandel, M. Veselsky, and S. Yennello, Phys. Rev. C **75**, 011601(R) (2007).

[90] D. Shetty, S. Yennello, and G. Souliotis, Phys. Rev. C **76**, 024606 (2007).

[91] D. Shetty, A. Botvina, S. Yennello, G. Souliotis, E. Bell, and A. Keksis, Phys. Rev. C **71**, 024602 (2005).

APPENDIX A

DETECTOR LAYOUT

This section contains information on the physical layout of the detector array. The rings are labeled with their respective detectors, power supply boards, and motherboards. In addition, some information about signal cable number in is included for the R10-11 region of the detector. Notes are also included about configuration anomalies.

It is important to note that depicted in Fig. 63 is the one J offset on R8-9 in the relationship between the flat the HV board is on and the Js of the flats that it powers. This offset it indicated with the arrows along the outer circle on the left hand side. Also of interest is that there is no observable correlation between CsI113 and any Si in NIMROD-ISiS.
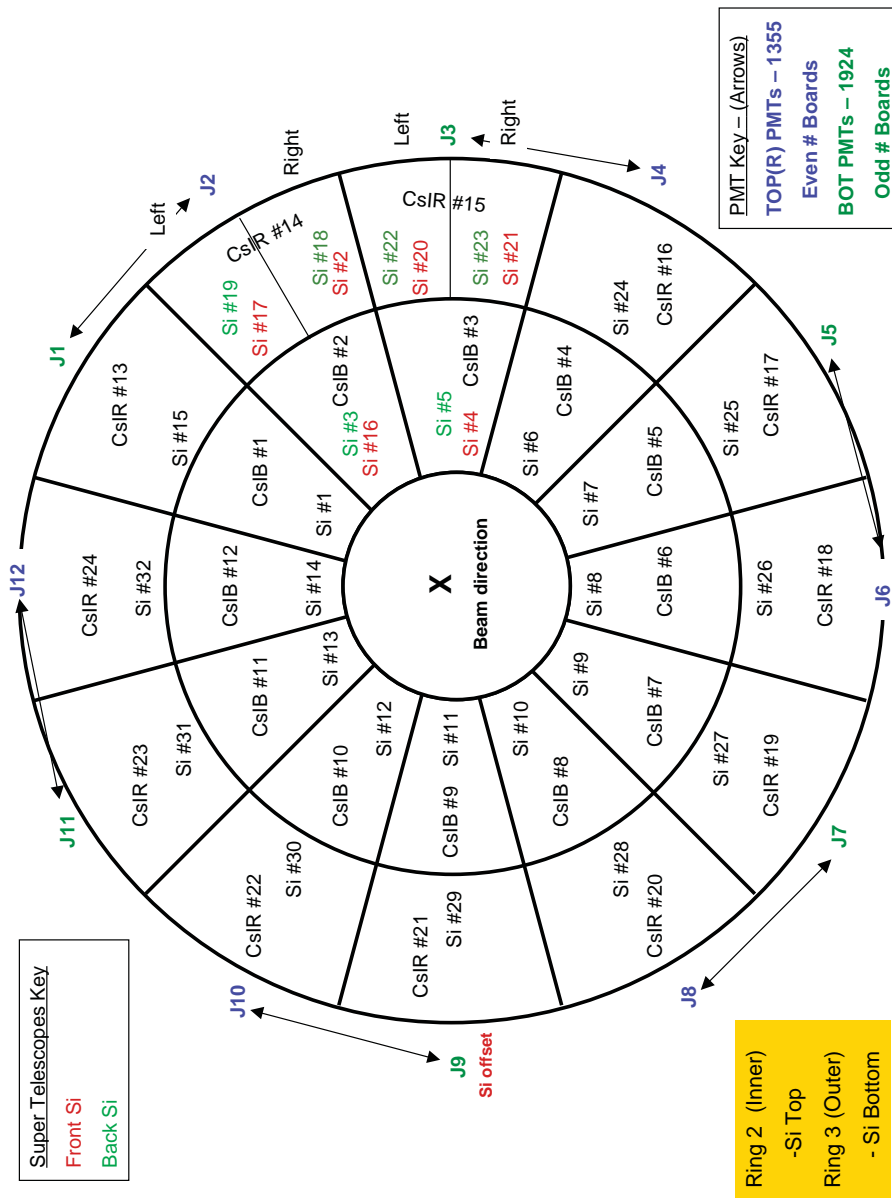
FIG. 60. Detector layout Ring 2-3.(color online.)
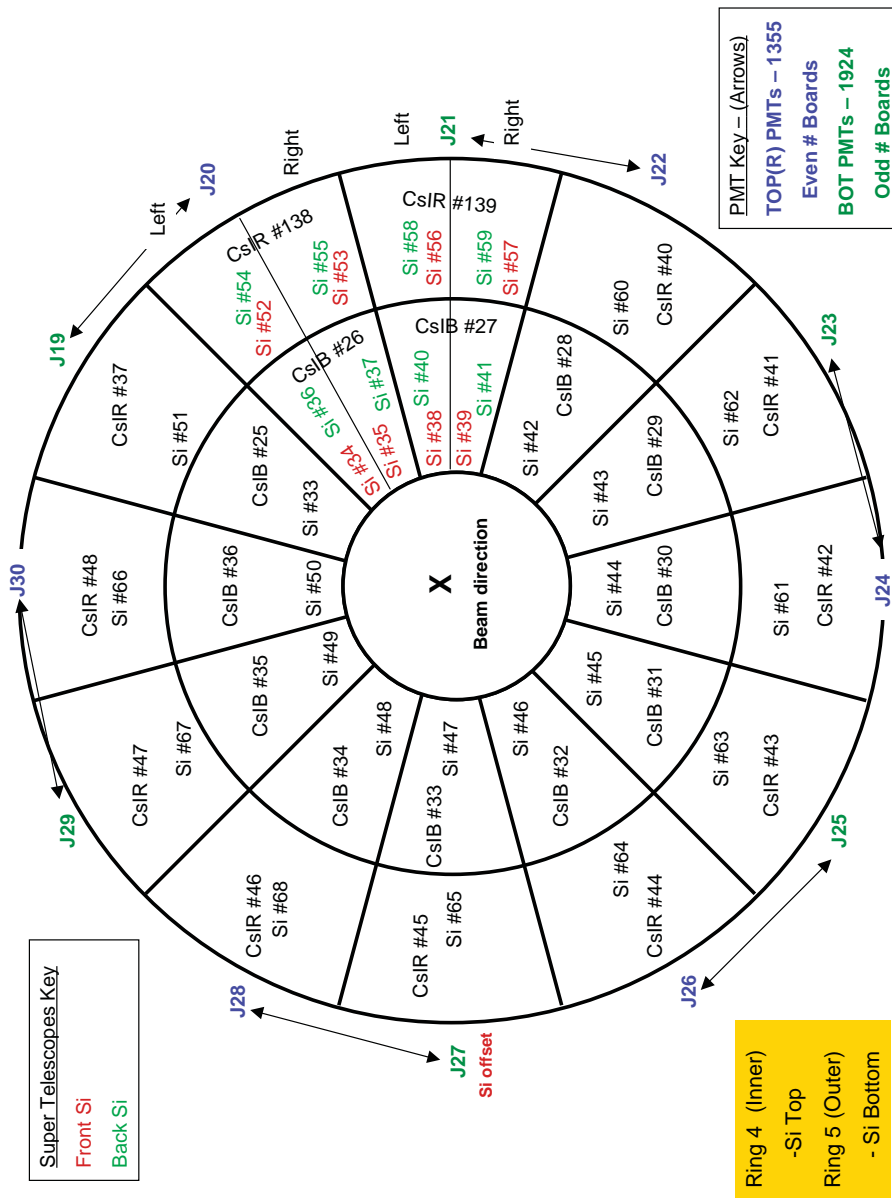
FIG. 61. Detector layout Ring 4-5.(color online.)
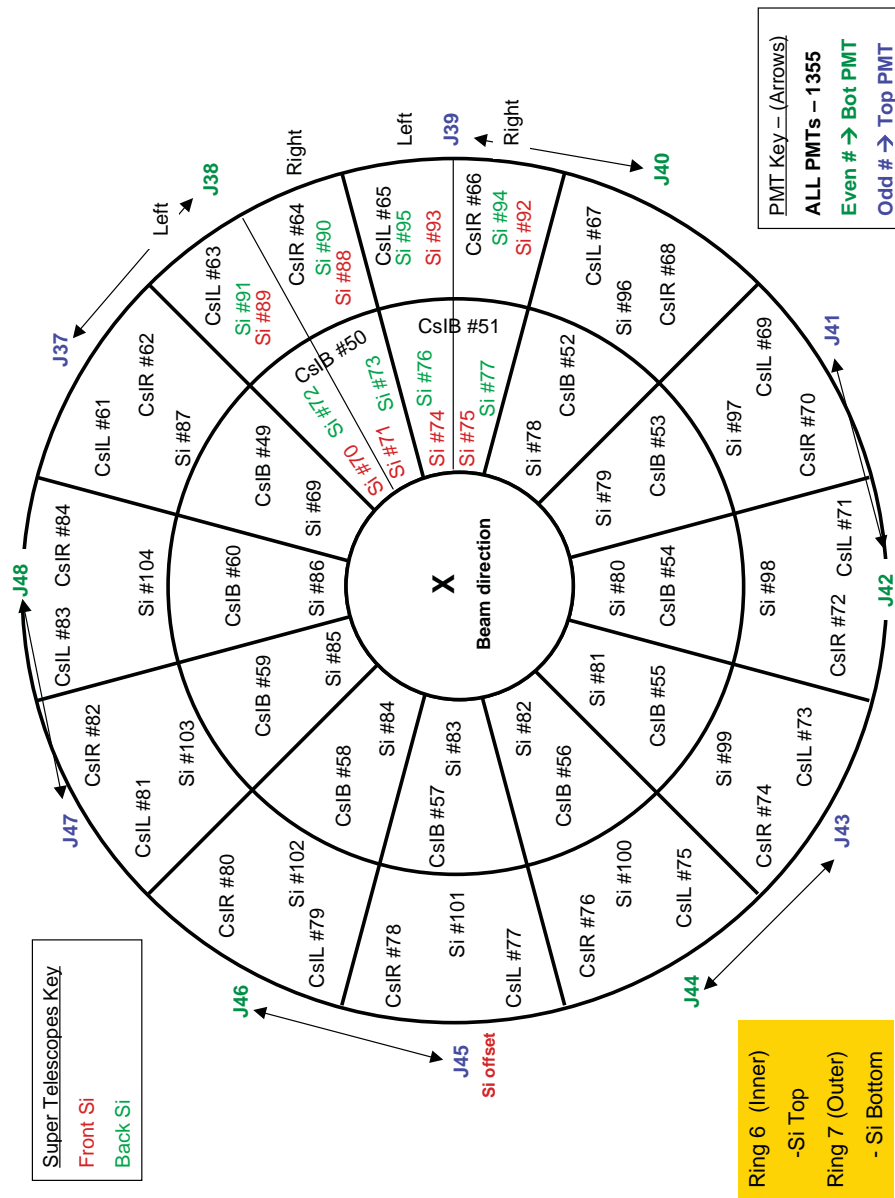
FIG. 62. Detector layout Ring 6-7. (color online.)
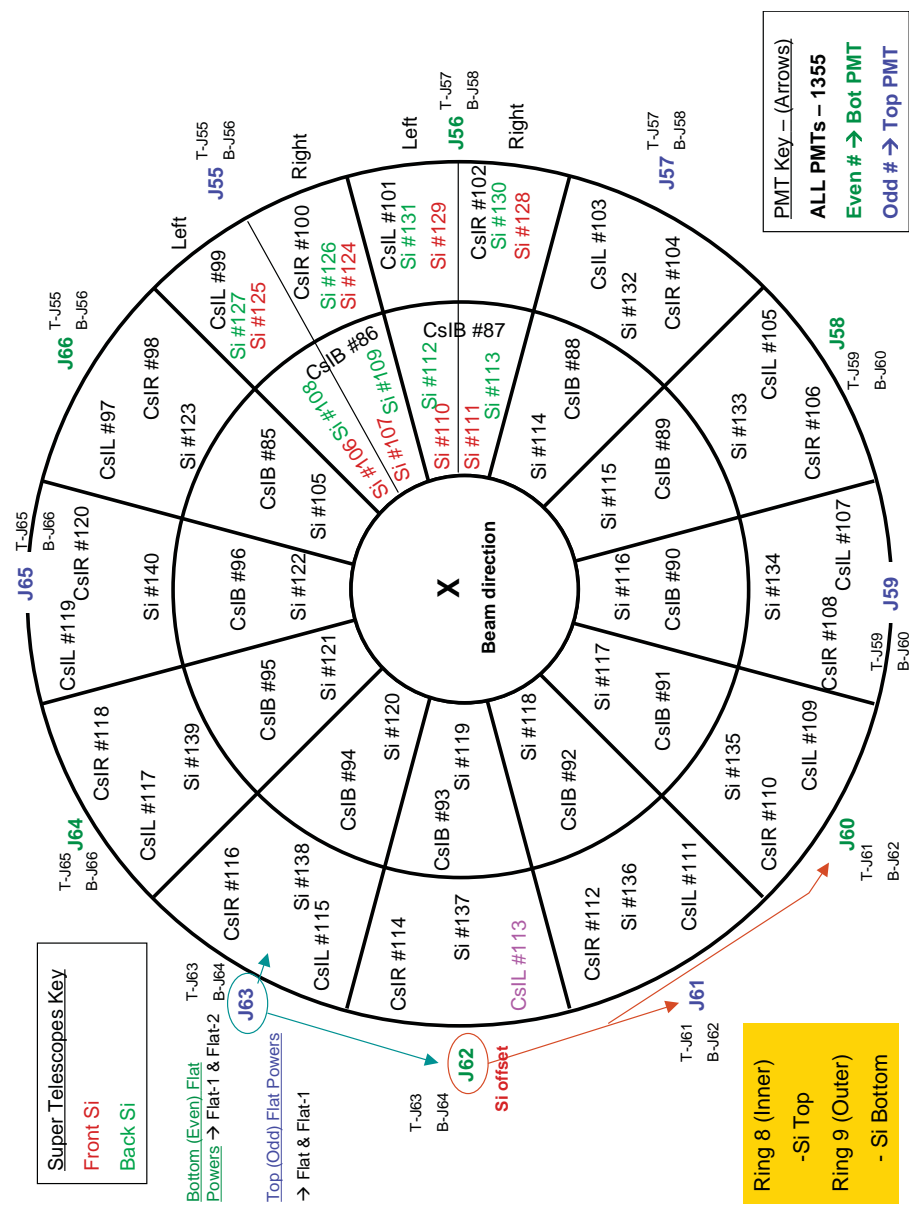
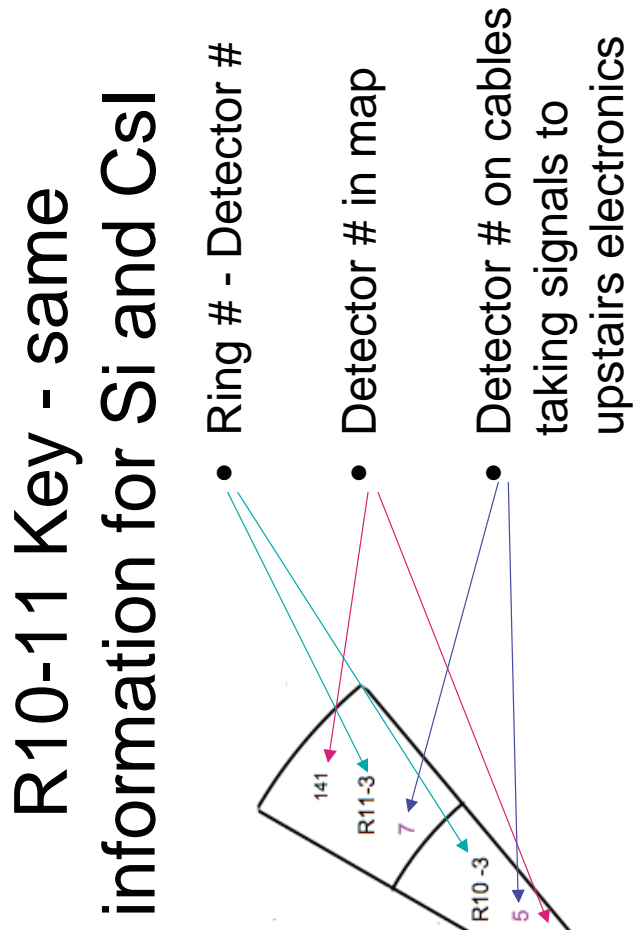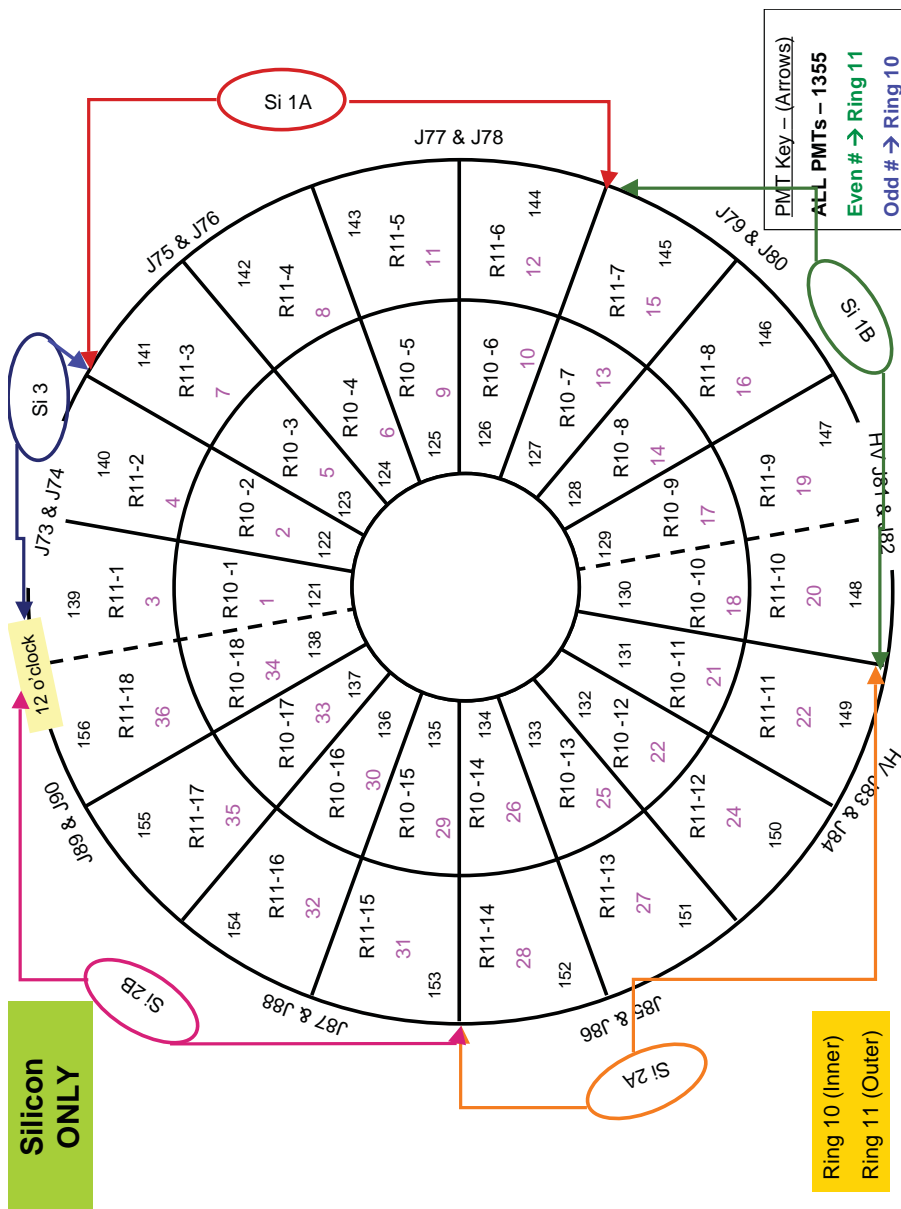FIG. 63. Detector layout Ring 8-9. (color online.)

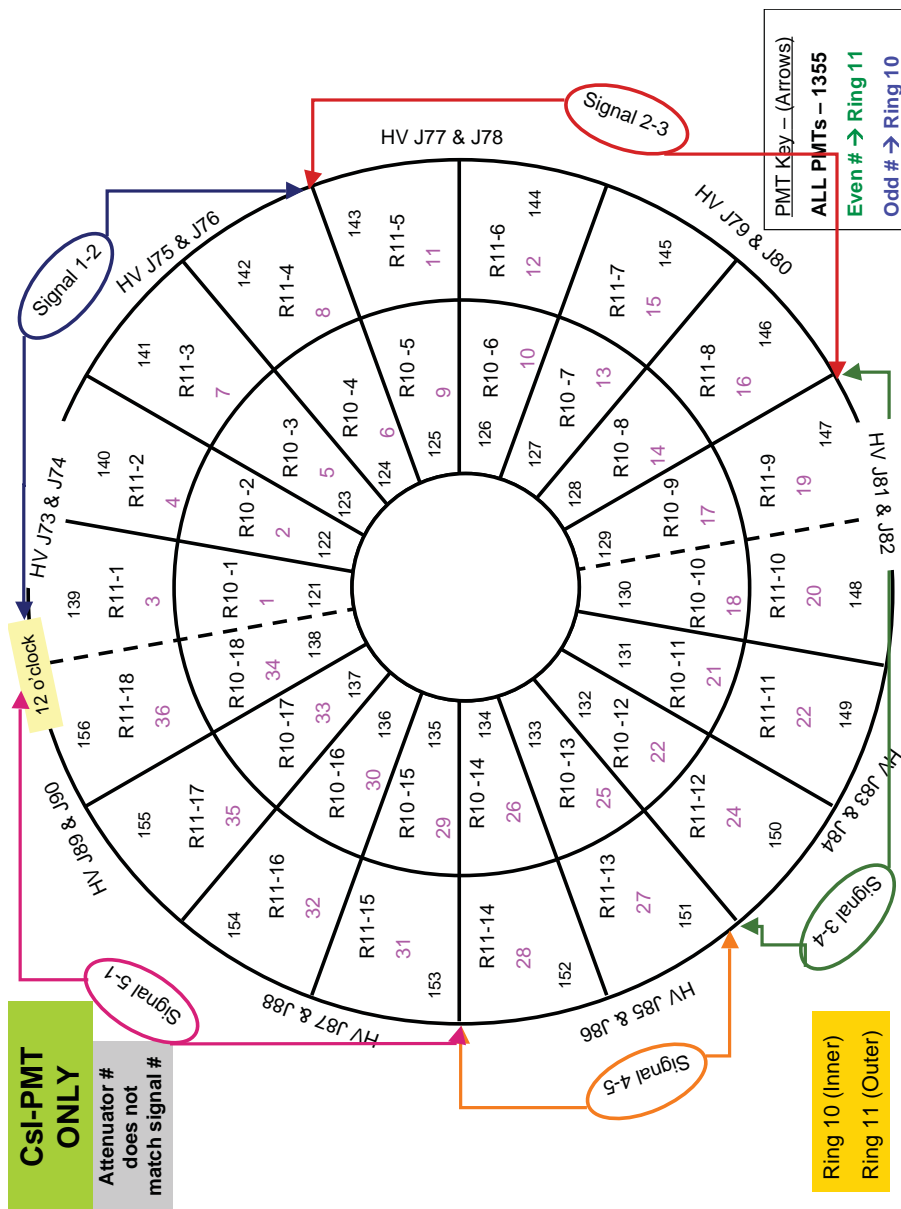# R10-11 Key - same information for Si and CsI

- Ring # - Detector #

- Detector # in map

- Detector # on cables taking signals to upstairs electronics

141
R11-3
7
R10 -3
5
123

FIG. 64. Detector layout key Ring 10-11 Si. (color online.)

FIG. 65. Detector layout Ring 10-11 Si. (color online.)

FIG. 66. Detector layout Ring 10-11 CsI. (color online.)

APPENDIX B

CALIBRATION BEAMS

TABLE VII. Calibration beams.

Ring	Run 208 (p,p')	Run 209 (p,p) GS+1st Ex	Run 210 (ne,ne)	Run 212 (a,a)	Run 232 (p,p)	Run 232 (d,d)	Run 233 (p,p) GS+1st Ex	Run 233 (d,d) GS+1st Ex
2	55	29	499.79	99.49	30	60	45	52.5
3	55	29.5	499.5	99.48	30	60	45	52.5
4	55	30	498.7	99.44	30	59.98	44.99	52.485
5	55	30.5	497.7	99.4	30	59.97	44.985	52.4775
6	54.98	30.99	495.7	99.3	29.98	59.95	44.965	52.4575
7	54.96	31.48	492.5	99.2	29.97	59.9	44.935	52.4175
8	54.93	31.965	486.9	98.97	29.96	59.84	44.9	52.37
9	54.88	32.44	480	98.7	29.4	59.75	44.575	52.1625
10	54.75	32.875	457	97.7	29.86	59.46	44.66	52.06
11	54.6	27.3	435	96.78	29.8	59.16	44.48	51.82

APPENDIX C

ENERGY SPECTRA IN LAB FRAME
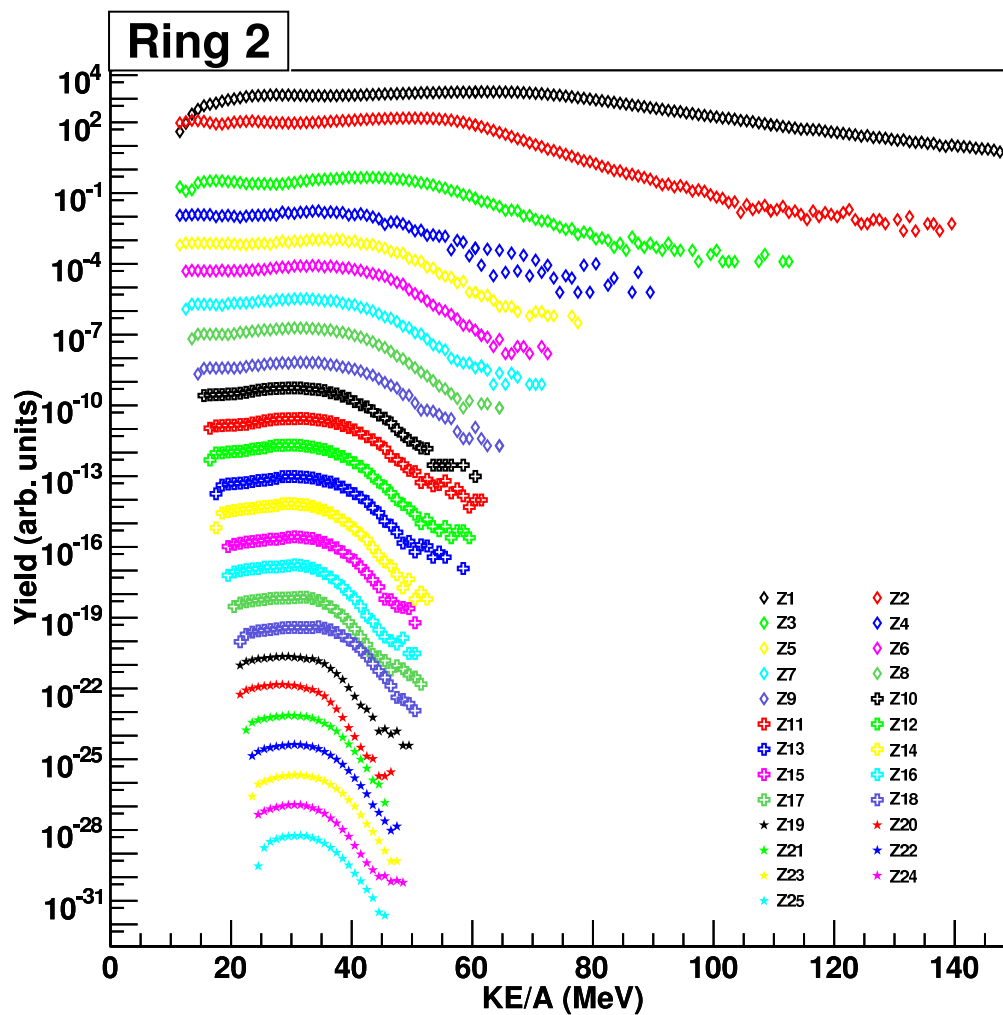
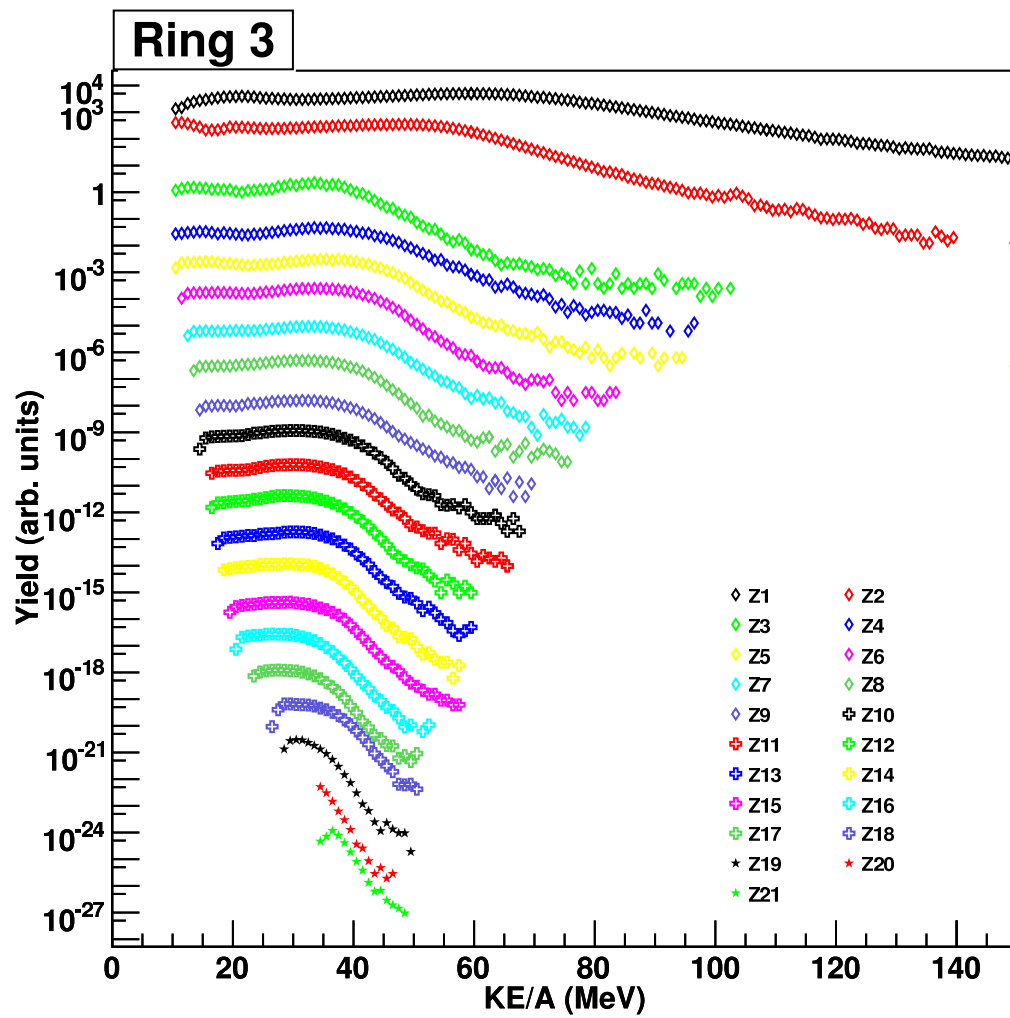FIG. 67. Lab frame energy spectra for ring 2. (color online.)

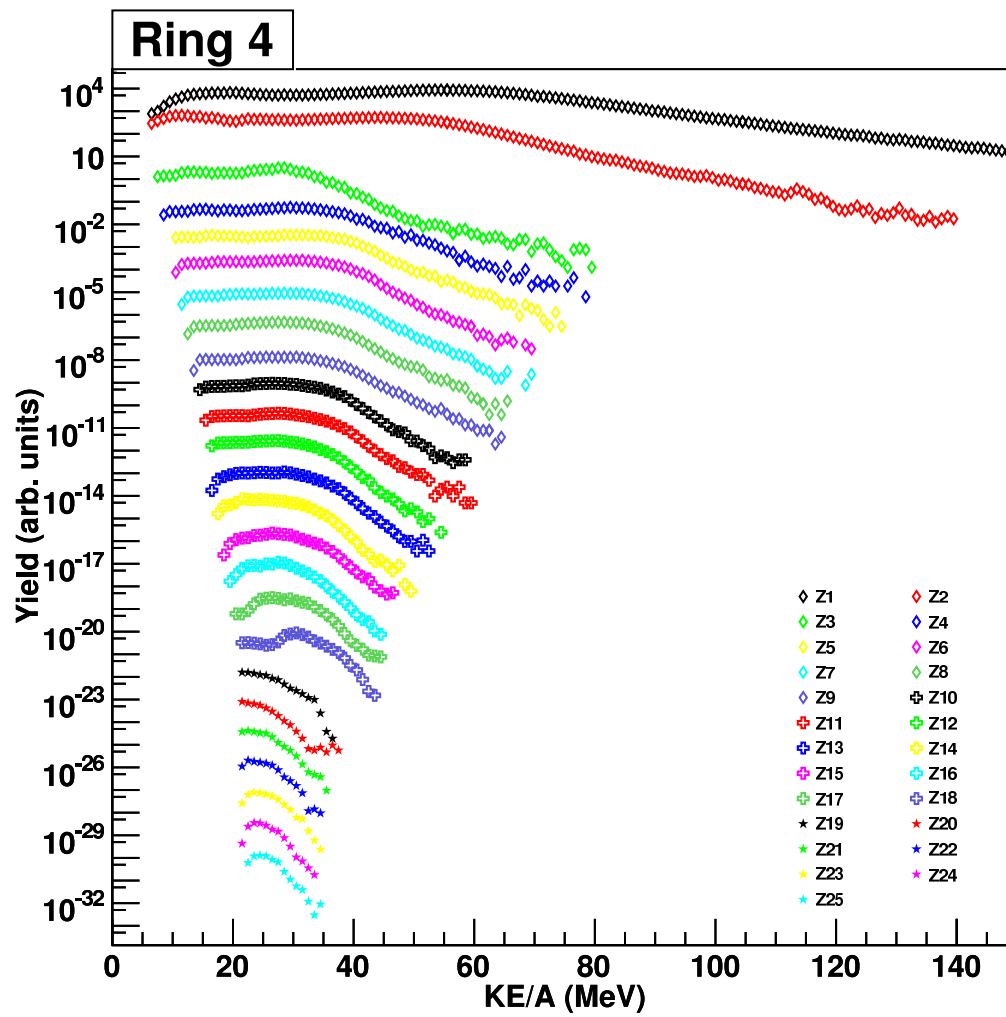FIG. 68. Lab frame energy spectra for ring 3. (color online.)

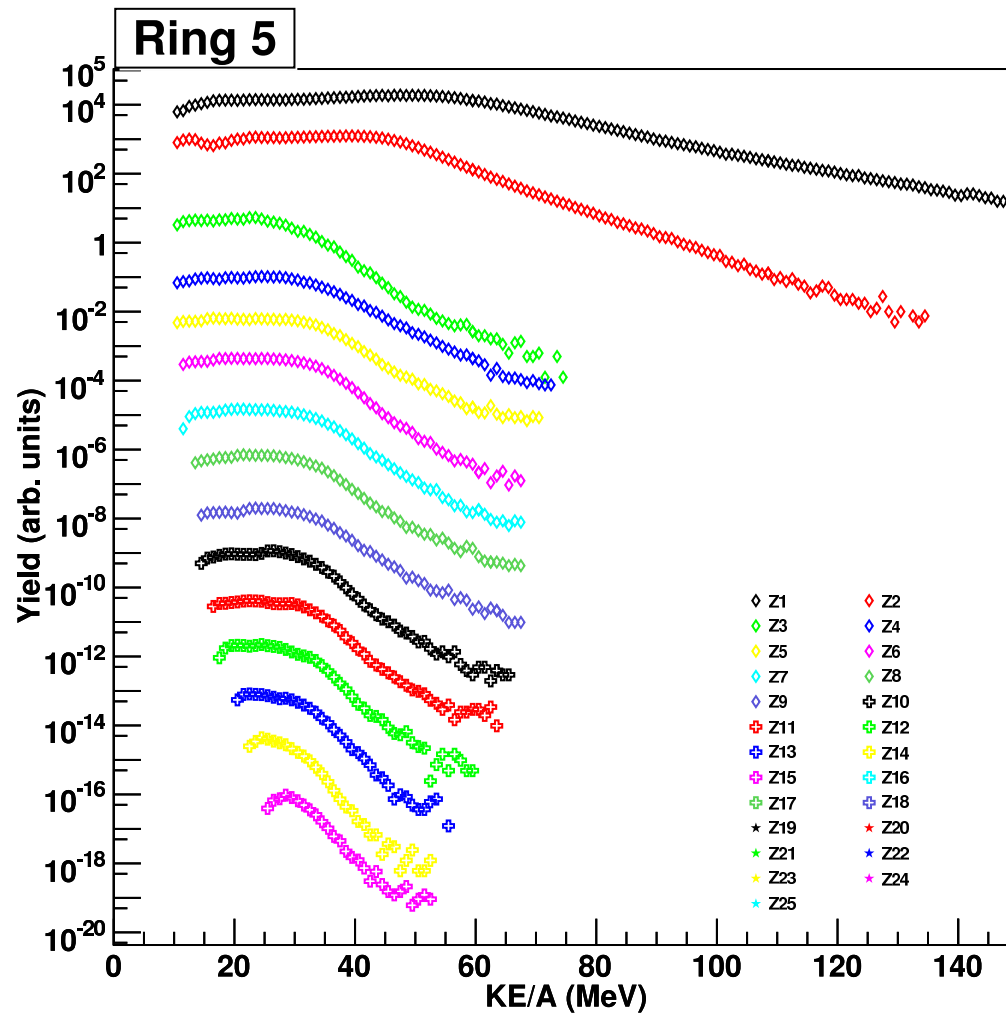FIG. 69. Lab frame energy spectra for ring 4. (color online.)

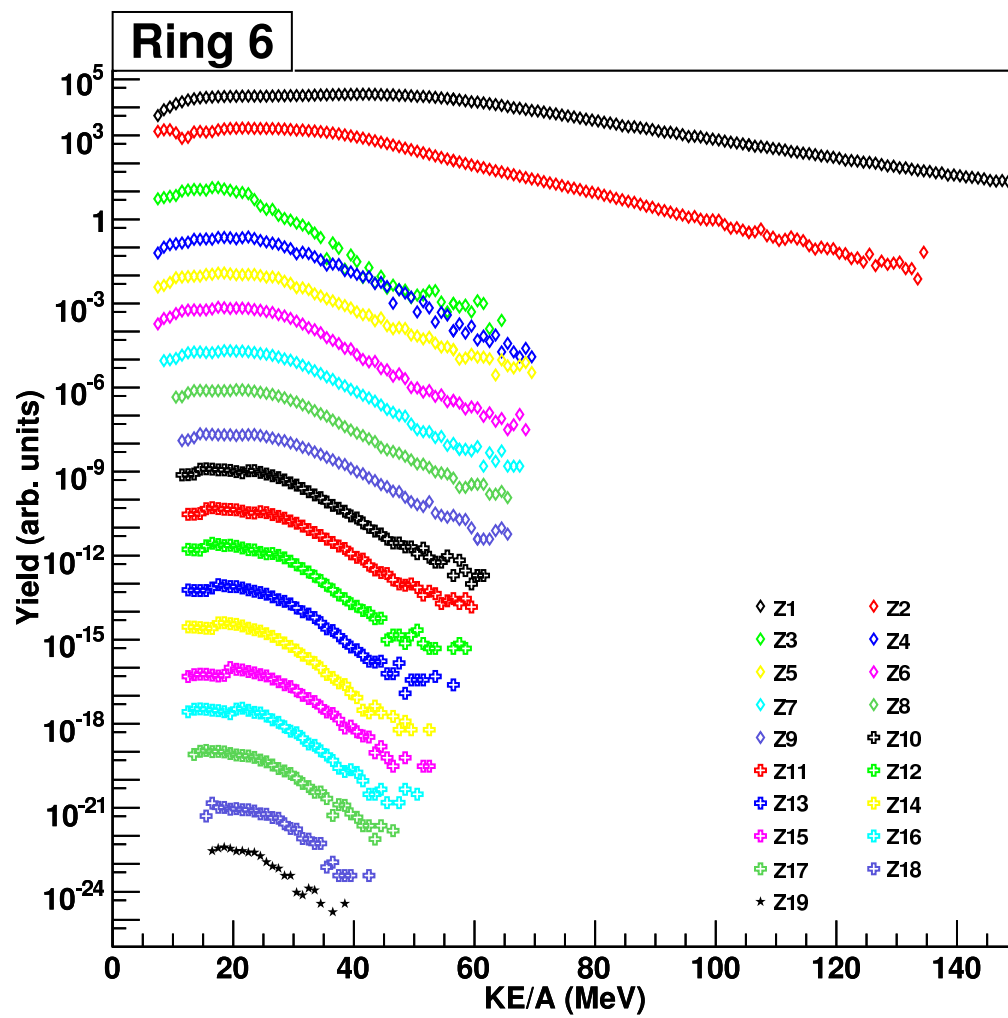FIG. 70. Lab frame energy spectra for ring 5. (color online.)

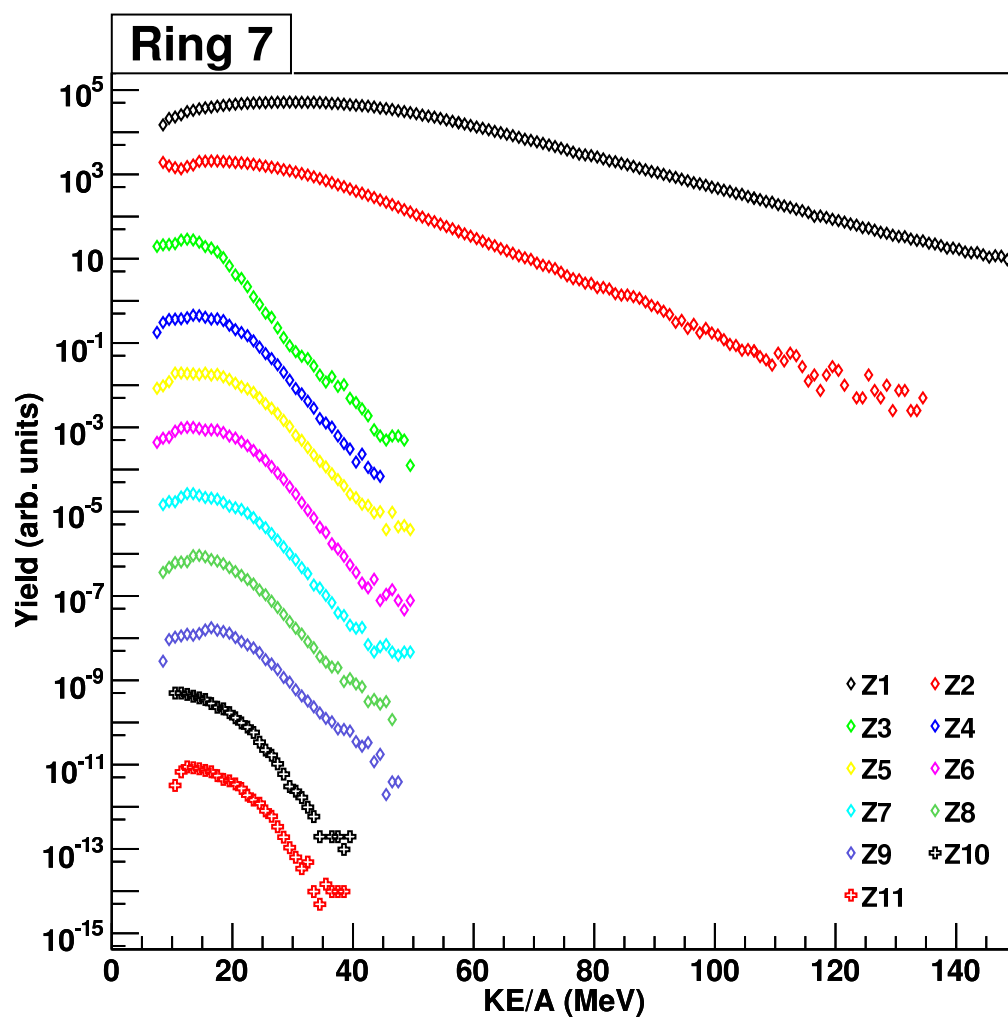FIG. 71. Lab frame energy spectra for ring 6. (color online.)

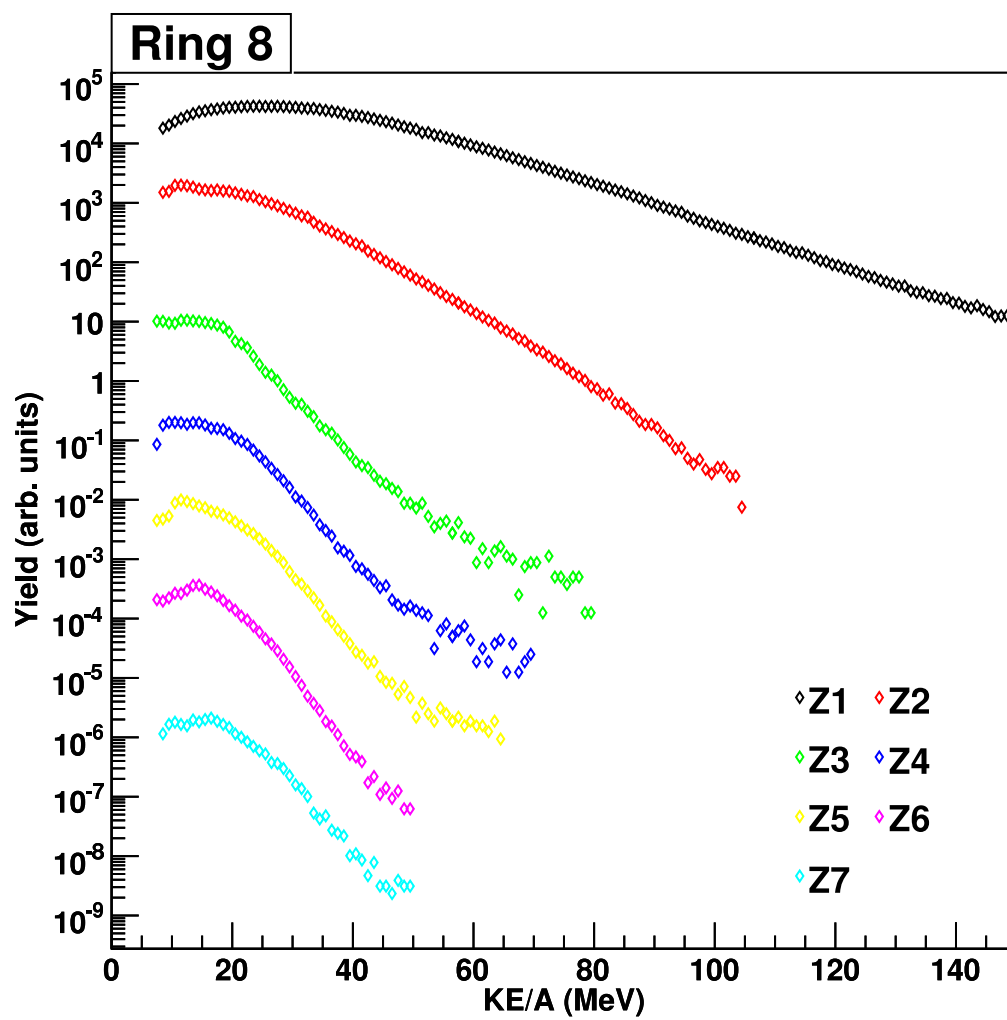FIG. 72. Lab frame energy spectra for ring 7. (color online.)

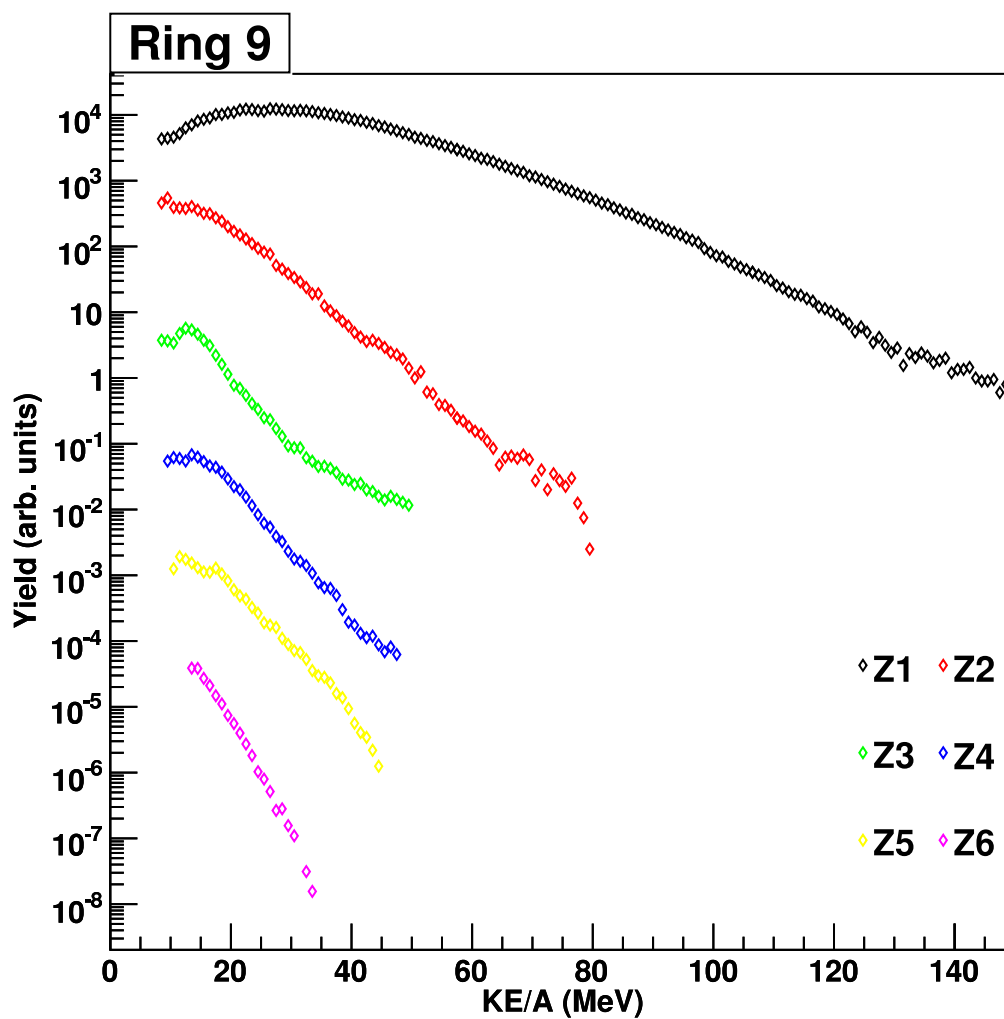FIG. 73. Lab frame energy spectra for ring 8. (color online.)

FIG. 74. Lab frame energy spectra for ring 9. (color online.)

VITA

Sara Katherine Wuenschel

EDUCATION

Ph.D., Texas A&M University, Nuclear Chemistry, August 2009

B.S., LeTourneau University, Chemistry

EXPERIENCE

Graduate Assistant Research, Texas A&M University (2005-2009)

Graduate Assistant Teaching, Texas A&M University (2004-2005)

CONTACT INFORMATION

Sara Wuenschel can be reached through Sherry Yennello at the Cyclotron Institute, Texas A&M University, College Station, Texas, 77843-3366

E-mail: swuenschel@gmail.com

SELECTED AWARDS, SCHOLARSHIPS, AND ASSISTANTSHIPS

Graduate Student Research and Presentation Grant - The Texas A&M University Association of Former Students and the Office of Graduate Studies 2008

Texas A&M Arthur E. Martell Travel Award - Texas A&M University Chemistry Department 2008

Departmental Fellowship- Texas A&M University Chemistry Department 2004

Graduated Magna Cume Laude- LeTourneau University 2004

SELECTED AFFILIATIONS

American Physical Society (Since 2007), American Chemical Society (Since 2005)

SELECTED PUBLICATIONS

NIMROD-ISiS, A versatile tool for studying the Isotopic Degree of Freedom in Heavy-Ion Collisions. S. Wuenschel *et. al.* Nucl. Instrum. Methods Phys. Res. A (2009)